INVESTIGATION OF CHEMICAL AND ELECTROCHEMICAL BEHAVIOUR OF GRAPHENE/MANGANESE OXIDE/TIN OXIDE TERNARY NANOCOMPOSITE

A THESIS SUBMITTED IN PARTIAL FULFILLMENT OF THE REQUIREMENT FOR THE DEGREE OF MASTER OF SCIENCE (M. Sc.) IN CHEMISTRY

SUBMITTED BY

Mohammad Mozammal Hosen

Student ID: F 1014032710

Session: October 2014

Nanochemistry Research Laboratory

Department of Chemistry

Bangladesh University of Engineering and Technology (BUET)

Dhaka - 1000, Bangladesh

March - 2017

CANDIDATE'S DECLARATION

It is hereby declared that this thesis or any part of it has not been submitted elsewhere for the award of any degree or diploma.

.....

(Mohammad Mozammal Hosen)

Signature of the Candidate

Bangladesh University of Engineering and Technology (BUET), Dhaka
Department of Chemistry

Certification of Thesis

A thesis on

INVESTIGATION OF CHEMICAL AND ELECTROCHEMICAL BEHAVIOUR OF GRAPHENE/MANGANESE OXIDE/TIN OXIDE TERNARY NANOCOMPOSITE

by

Mohammad Mozammal Hosen

has been accepted as satisfactory in partial fulfillment of the requirements for the degree of Master of Science (M. Sc.) in Chemistry and certify that the student has demonstrated a satisfactory knowledge of the field covered by this thesis in an oral examination held on March 7, 2017.

Board of Examiners

1. Dr. Md. Shakhawat Hossain Firoz
Associate Professor
Department of Chemistry
BUET, Dhaka

07.03.17
Supervisor & Chairman

2. Dr. Md. Rafique Ullah
Professor and Head
Department of Chemistry
BUET, Dhaka

Member (Ex-officio)

3. Dr. Md. Abdur Rashid
Professor
Department of Chemistry
BUET, Dhaka

Member

4. Dr. Abu Bin Imran
Assistant Professor
Department of Chemistry
BUET, Dhaka

Member

5. Dr. Md. Mominul Islam
Associate Professor
Department of chemistry
University of Dhaka, Dhaka

Member (External)

DEDICATED TO

MY FAMILY MEMBERS

AND

REVERENT TEACHERS

Acknowledgement

First and for most, I would like to praise the name of the almighty Allah, for giving me health, patience and courage from the starting of this program till now to carry out the research work presented in this dissertation.

I would like to express my heartfelt gratitude and sincere appreciation to my honourable advisor and supervisor, Dr. Md. Shakhawat Hossain Firoz, Associate Professor, Department of Chemistry, BUET, for his kind supervision, indispensable guidance, illuminating suggestions and constant inspiration through the whole research period. I am greatly in debt to him for giving me the opportunity to work on the interesting field of graphene along with availing the scope of working with different research groups and hence I feel myself extremely lucky to be a member of his research group, nanoChem.

I am also greatly obliged to Dr. Md. Mominul Islam, Associate Professor, Department of Chemistry, University of Dhaka, for introducing me to the exciting field of electrochemistry and offering me the chance to work with his research group at Materials Chemistry Research Laboratory, University of Dhaka. I am really thankful to him for his kind facilitation of the electrochemical characterization of the synthesized materials, patient guidance in the relevant studies and kindling advices during the analysis of the results.

I owe a heartfelt gratitude to Ratan Kumar Paul, Assistant Professor, Department of Chemistry, Pabna University of Science and Technology, for his directions during the beginning of the project.

I cannot but thank Dr. Kazi Md. Shorowordi, Associate Professor, Department of Materials and Metallurgical Engineering, BUET, for his crucial support during the target materials synthesis.

A big thanks belongs to every members of our research group at Nanochemistry Research Laboratory (nanoChem), BUET, for their assistances during my whole work. I am also thankful to Azam Research Group, Department of Chemistry, BUET, for their assistance during the synthesis of the materials. I am highly grateful to all members including teachers and students at Materials Chemistry Research Laboratory, University of Dhaka, for the amicable environment they provided during my work with them. A special thanks

goes to Hemshankar Saha Roy, Gulshan Ara, Saddam Hossain and Golam Rabbani for their helping hand in case of electrochemical measurements.

I would like to convey my deepest gratitude to the board of examiners for their valuable corrective suggestions regarding this dissertation.

I thank CASR, BUET for funding this project, Department of Chemistry, BUET for all the supports it provided in the project and Ministry Of Science and Technology (MOST) for awarding me National Science and Technology (NST) fellowship regarding this project.

Finally, I would like to express my warmest thanks to my family members for their continuous inspirations, moral supports and immeasurable sacrifices during this project.

7 March, 2017 Mohammad Mozammal Hosen

Abstract

Graphene based nanocomposites show many intriguing physical and chemical properties. Dye removal capacity and higher electrochemical capacitance with longer cyclic performance are two prominent arena of them. Binary nanocomposites of Mn-oxide and Sn-oxide with graphene, offering low cost, environmental benignity and easy synthesis procedure, constitute some of the ideal examples in this regard. Consequently, the graphene based ternary nanocomposites of these metal oxides could be an alternative material with greater potential, to serve the same purposes. Hence, in our present work, a ternary nanocomposite consist of graphene, Mn-oxide and Sn-oxide was synthesized by following a three step method. Graphene oxide (GO), obtained from graphite flake following Hummers method was introduced, first with $Mn(CH_3COO)_2$ and then with $KMnO_4$ in water-isopropyl alcohol system to obtain GO/Mn-oxide nanocomposite. It was further stirred with $SnCl_2$ in aqueous media furnishing a graphene/Mn-oxide/Sn-oxide ternary nanocomposite. The obtained mass was dried and then annealed under N_2 inert atmosphere to achieve better crystallinity of nanoparticles and better reduction of GO. The synthesized materials were characterized using FTIR, FESEM, EDX, XRD and TGA. Dye removal capacity of the materials synthesized, were investigated with visible spectroscopy using MB as a model dye. After 75 minutes of interaction, with 5 mg sample in 5 ppm solution at pH 3, the ternary nanocomposite showed a specific adsorption capacity of 17.7 mg/g, while that of graphene/Mn-oxide and graphene/Sn-oxide binary nanocomposites, under same conditions, was 17.5 mg/g and 17.4 mg/g respectively; suggesting that, the binary and the ternary nanocomposites have almost same amount of surface area. It was also explored that, the ternary nanocomposite is more effective at its lower dose and in low pH solution. Electrochemical capacitive behaviour was investigated with CV, CP and EIS. As a capacitive material, at the current density of 0.5 A/g, it showed a specific capacitance of 145.6 F/g, while under the same conditions, the graphene/Mn-oxide and the graphene/Sn-oxide binary nanocomposites showed 463.8 and 178.3 F/g specific capacitance respectively. The low specific capaciatance of the ternary nanocomposite in comparison to the binaries was attributed to the different ratio of the oxide forms of metals on graphene and their nature. However, the ternary nanocomposite showed a higher discharging/charging time ratio, lower charge transfer resistance and after 500 cycles, it retained almost 84% of its electrochemical charge storage capacity.

Contents

List of Figures

List of Tables

List of Flow Charts

Chapter 1

Introduction

1.1 Introduction

The world, shaped as it is today by the progress of science and technological inputs and massive industrialization and civilization is marked by the emergence of new, increasingly surprising technological amenities along with various natural or environmental crisis and civic life limitations. Resolution of this crisis or limitations of society and civilization has always been the aim of research of the scientific community. They have devoted their efforts to find suitable solution through development of new technologies, new materials and their new applications. Development of new materials may lead us to more useful and effective utilization of the limited resources we have in our hand as well as unlock the potential of the utopian future we dream of today [1].

In the recent years, various natural disasters and climate change caused effects has drawn our attention to environmental pollutions. One of the major form of it is water pollution [2-3]. Availability of safe water has a deep impact on our life, society and state [4-5]. According to UNICEF, every year, on an average 250 million people worldwide succumb to diseases related to water pollution and 3000 children die every day around the globe from various diseases resulting from the lack of pure water. According to a survey done by Food & Water Watch cites that approximately 3.5 billion people in 2025 will face water shortage issues. This is likely to happen because the world pollution is increasing tremendously with more water sources getting contaminated from water pollution [6].

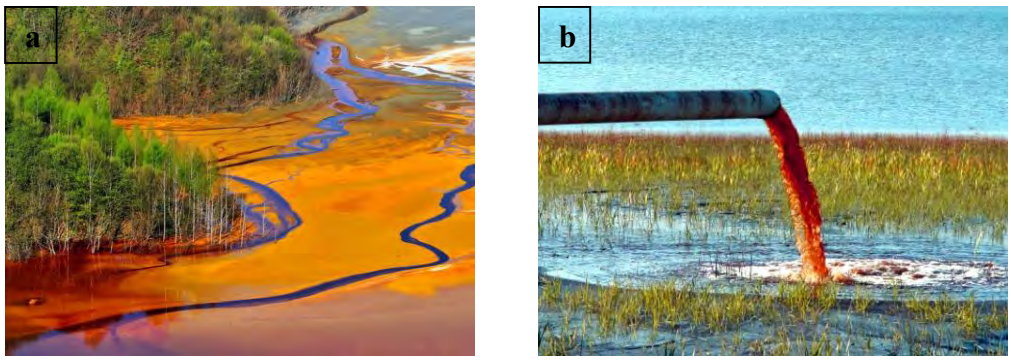

Fig. 1.1- Polluted water running (a) through a river and (b) out of a sewage pipe

To qualify as a developed country, for Bangladesh, water pollution is a great challenge against the target of ensuring safe water for total population [7]. Water pollution may be defined as any chemical or physical change in water, detrimental to living organisms. It has many sources. One of the major source of this pollution in Bangladesh is organic pollutants particularly dye from tannery and garments industry [8].

Fig. 1.2- (a) A dye solution is being used in a tannery in Hazaribagh, Dhaka to colour animal skin and (b) later discharged to a nearby swamp [3]

To prevent this damaging advancement, dye removal can be an effective way [9]. Among various materials, it has been observed that, nanoparticles or nanocomposites with their high surface area and catalytic activity are most effective in this regard [10]. The effectiveness is usually observed by conducting controlled experiment by taking active sample with a model dye e.g. methylene blue (MB) under different criterions and optimum conditions are established [11-15].

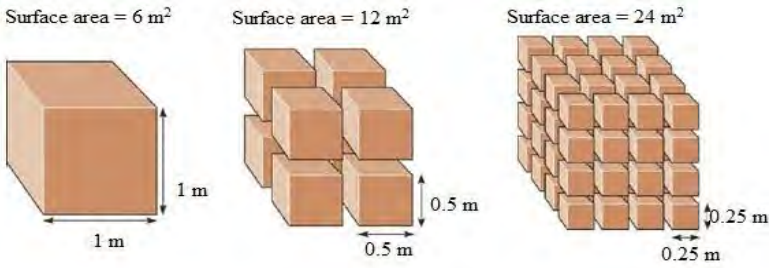

Fig. 1.3- High surface area of nanoparticle or composites compared to bulk materials [16]

Another crying issue of our present time is the shortage of high capacity energy storage materials [17]. Nowadays most of our daily life instruments we rely upon e.g. smartphone, tablet PC, watch, laptop, car are battery i.e. energy storage material dependent. Limitation in charge storage capacity of this materials makes us suffer in various ways. Besides, the dream of energy efficient power system or the environmentally benign electric vehicles

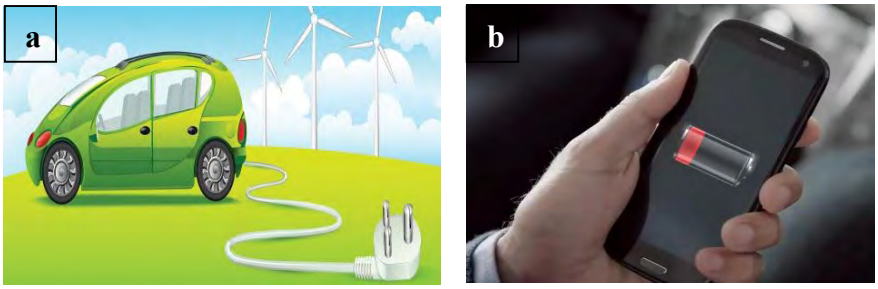

Fig. 1.4- (a) Electric car and (b) smartphone -two charge storage reliable device

of future is also largely dependent on the development of high capacity charge storage materials [18]. Nanocomposites has shown hope in this regard.

Forming electrical double layer at electrode interface while immersed in an electrolyte solution the nanocomposites show capacitance known as electrical double layer capacitance (EDLC). Besides, they can also store charge by means of charge transfer process known as pseudocapacitance [19].

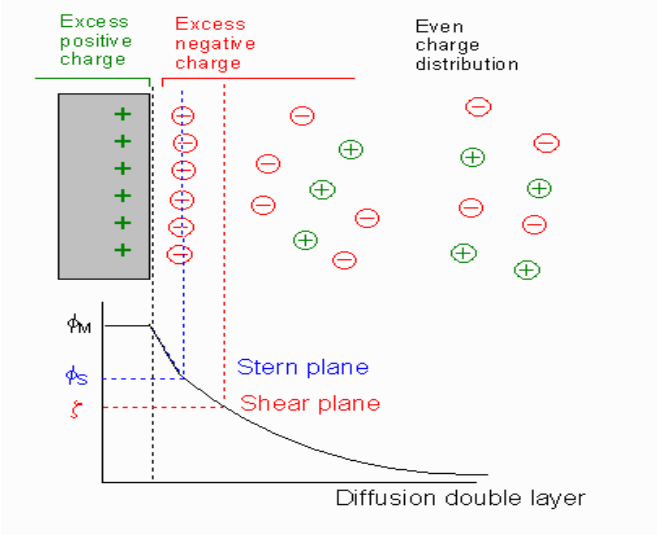

Fig. 1.5- Electrical double layer formed at an electrode surface in electrolyte solution

The both types of problem presented above have their own challenges and deserve attention to be resolved or alleviated. The utmost importance of this problems can be understood from their separate position as goal no. 6 and goal no. 7 among the goals for SDG, 2030 set up by United Nations (UN) in which Bangladesh is a model partner [20-21]. One common way to address these issues is developing new nanocomposite materials and explore there suitability in the areas of applications of interest.

Fig. 1.6- SDG goal no. 6 and 7 set up by UN

Nanocomposites are actually combination of two or more materials with all are present in significant proportions with each having at least one dimension in nanometer scale. In a nanocomposite structure, one serves as matrix while others are loaded on it. Nanocomposites are advantageous from several perspectives. They include the individual

nanoparticle properties, multifunctional capabilities and easy chemical functionalization [16]. The importance and popularity of nanocomposite has led to more than 13000 paper and 4000 patents on nanocomposites in last two decades [22].

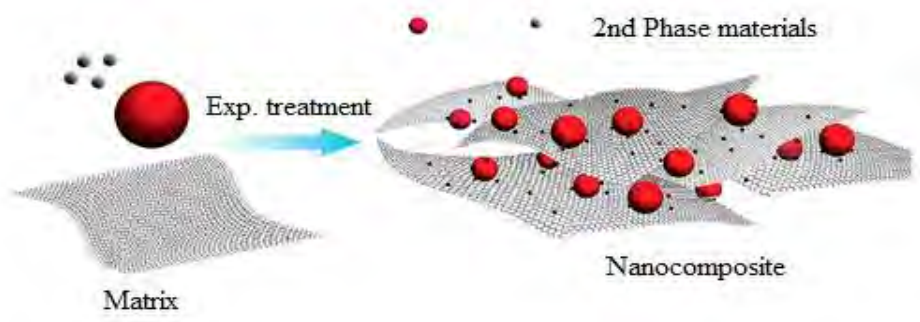

Fig. 1.7- Synthesis of nanocomposite

Graphene based metal oxide nanocomposites are recent addition among the class of nanocomposites. Graphene itself is a new material, developed only in 2004 by A. Geim and K. Novoselov [23-24]. It is, also called as 'super carbon' [25], is one-atom thick two-dimensional sheet of carbon atoms fashioned in a honeycomb lattice and is considered as the future revolutionary material [26]. It has many unique properties including openness from both sides for reaction [27], large theoretical surface area (2630 m^2/g) [28], high electron mobility (200000 cm^2/Vs) [29], high Youngs modulus (~ 1TPa) [30], good optical transparency (~ 90%) [31] etc. However, it suffers from a serious drawback that pure graphene sheet tends to undergo crumpling [32]. This can be overcome by loading nanoparticles, specifically of metal oxides, one or two at a time, resulting to binary and ternary nancomposites respectively [33]. Graphene based manganese oxide or tin oxide binary nanocomposite constitute some of the ideal examples in this regards. Due to their low cost, environmental benignity and easy synthesis [34-35], they have drawn much attention of researchers and has been applied in dye removal and as electrochemical charge storage material. e.g.

Qian *et al.* synthesized graphene/MnO_2 by a polymer-assisted chemical reduction method in 2011 and investigated the capacitive properties of the MnO_2/graphene composite by cyclic voltammetry (CV). The composite exhibited a high specific capacitance of 324 F/g in 1 M Na_2SO_4 electrolyte and also showed excellent long-term cycle stability [36].

Qu *et al.* synthesized graphene/MnO_2 nanocomposite by treating graphene oxide/manganese sulfate with potassium permanganate followed by glucose reduction in

2013 and applied it in oxidative decomposition of MB in presence of H_2O_2. He showed that, 50 mL of MB of 50 ppm can be completely decolourized and nearly 66% mineralized at 50° C in 5 minutes with 10 mg of the nanocomposite [37].

Ye *et al.* reported a facile method to prepare MnO_2/reduced graphene oxide (rGO) composites in 2013 and examined their applications as electrodes in flexible solid-state supercapacitors. The MnO_2/rGO composite electrodes exhibited a good electrochemical performance with an area capacitance of 14 Fcm^{-2} at 2 mVs^{-1} and excellent stability [38].

Huang *et al.* in 2014 reported a MnO_2/graphene nanocomposites synthesized through a simple route in a water-reflux condenser system. 60-MnO_2/graphene composite (48 wt% MnO_2) displayed the specific capacitance as high as 350 F/g at 1000 mA/g, which was almost two times higher than that of MnO_2 (163 F/g). Furthermore, the composite exhibited excellent long cycle life along with ~ 93% specific capacitance retained after 5000 cycle tests [39].

Wen *et al.* proposed a facile method to prepare the MnO_2-graphene composite in 2015 with a sandwich structure. The MnO_2-graphene electrode retained a capacity of 752 mAh/g at a current density of 100 mA/g after 65 cycles [40].

Wang *et al.* synthesized Mn_3O_4 embedded graphene nanocomposite in 2010 by mixing graphene suspension in ethylene glycol with MnO_2 organosol. It exhibited a high specific capacitance of 175 F/g in 1M Na_2SO_4 electrolyte and 256 F/g in 6M KOH electrolyte, respectively [41].

Wang *et al.* synthesized porous Mn_3O_4–graphene nanocomposite, based on a convenient and feasible solution based synthetic route under mild conditions in 2012. He observed, the as-prepared Mn_3O_4–graphene nanocomposites exhibit remarkable pseudocapacitive activity including high specific capacitance (236.7 F/g at 1 A/g), good rate capability (133 F/g at 8 A/g), and excellent cycle ability (the specific capacitance only decreases by 6.32% of the initial capacitance after 1000 cycles) [42].

Li *et al.* offered a facile, effective, energy-saving, and scalable microwave hydrothermal technique to grow well-crystallized Mn_3O_4-reduced graphene oxide (rGO) nanocomposites in 2012. The capacitance value of the nanocomposite, 153 F/g, was much higher than that of the bare Mn_3O_4 (87 F/g) at a scan rate of 5 mV/s in the potential range from −0.1 V to 0.8 V. A 200% increase in capacitance was observed for the

nanocomposite and no observable capacitance fading were found up to 1000 cycles [43].

Fan *et al.* synthesized Mn_3O_4/graphene composite in 2013 with the structure of Mn_3O_4 nanoparticles anchored on graphene sheets was synthesized using facile one pot hydrothermal method. The Mn_3O_4/graphene nanocomposite exhibited a specific capacitance of 171 F/g in 1 M Na_2SO_4 aqueous electrolyte and a good rate property [44].

Yao *et al.* prepared Mn_3O_4−reduced graphene oxide (rGO) hybrids in 2013 and studied their catalytic performance in heterogeneous activation of peroxymonosulfate (PMS) to oxidize a target pollutant, in aqueous solutions. He observed that the combination of Mn_3O_4 nanoparticles with graphene sheets leads to a much higher catalytic activity than that of pure Mn_3O_4 or rGO. Typically, 30 mg/L of Orange II could be completely oxidized in 120 min at 25° C by 0.05 g/L of Mn_3O_4−rGO hybrids, showing a promising application of the catalyst in the oxidative degradation of aqueous organic pollutants [45].

Zhang *et al.* reported a general one-pot hydrothermal synthesis to prepare a nanostructured Mn_3O_4–reduced graphene oxide (rGO) hybrid in 2014. He demonstrated the application of the Mn_3O_4–rGO hybrid in heterogeneous activation of peroxymonosulfate (PMS) to degrade an aqueous organic pollutant and in LIBs. After 90 min 100% decomposition were shown to achieve with 30 mg/L of Orange II, 0.05 g/L of Mn_3O_4–rGO, and 1.5 g/L of PMS. As an anode material of LIBs, the hybrid showed a high specific capacity up to 676 mAh/g after 100 cycles of a cycling performance test [46].

Antihos *et al.* synthesized rGO/MnO nanocomposite via exfoliation of graphene oxide with microwave radiation (mw rGO), in 2012. The 90% MnO–10% mw rGO (w/w) nanocomposite exhibited a capacitance of 0.11 F/cm^2 (51.5 F/g by mass) and excellent capacity retention of 82% after 15,000 cycles at a current density of 0.5 A/g [47].

Xu *et al.* in 2015 reported a novel composite of polyhedral MnO (p-MnO) nanocrystals and reduced graphene oxide (rGO) nanosheets. As an anode material for LIBs, the p-MnO/rGO electrode showed a reversible capacity of 988.6 mAh/g after 120 cycles at a current density of 100 mAh/g and delivered 591.1 mAh/g at a rate of 1600 mA/g [48].

Li *et al.* developed a one-step method to fabricate conductive graphene/SnO_2 (GS) nanocomposites in acidic solution in 2009. Graphite oxides were reduced by $SnCl_2$ to graphene sheets in the presence of HCl and urea with the growth of SnO_2 nanoparticles. It showed a specific capacitance of 43.4 F/g at 100 mV in 1M H_2SO_4 [49].

Wang *et al.* in 2011 presented a simple solution-based synthesis route, to produce a SnO_2/graphene nanocomposite. It was found that the optimum molar ratio of SnO_2/graphene for electrochemical performance was about 3.2:1 (2.4 wt% of graphene). The composite delivered a charge capacity of 840 mAh/g (with capacity retention of 86%) after 30 charge/discharge cycles at a current density of 67 mA/g [50].

Seema *et al.* developed rGO–SnO_2 nanocomposite in 2012 via a redox reaction between graphene oxide (GO) and $SnCl_2$. Graphene oxide (GO) was reduced to graphene (rGO) and Sn^{2+} was oxidized to SnO_2 during the redox reaction, leading to a homogeneous distribution of SnO_2 nanoparticles on rGO sheets. He observed the rGO–SnO_2 composite showed an enhanced photocatalytic degradation activity for the organic dye methylene blue under sunlight compared to bare SnO_2 nanoparticles [51].

Shanmugam *et al.* synthesized graphene-SnO_2 nanocomposite in 2015 by coating SnO_2 nanoparticles on graphene sheets. The strong photocatalytic degradation of Methylene orange (MO) dye was analyzed using the G-SnO_2 nanocomposite under the visible light irradiation and showed that the nanocomposite can achieve 100% removal compared to 65% of SnO_2 [52].

Belmurugan *et al.* synthesized graphene/SnO_2 nanocomposite by a simple wet chemical route in 2016. The electrochemical performances of SnO_2/G nanocomposites towards supercapacitors were studied in 6M KOH electrolyte. A maximum specific capacitance of 818.6 F/g was obtained at 1 mV/s scan rate suggesting that the presence of graphene matrix in SnO_2 nanoparticles have enhanced the electrochemical behaviour of SnO_2. The galvanostatic charge/discharge studies confirmed the good cyclic stability [53].

Yan *et al.* developed, a very simple solution-based method to coat amorphous MnO_2 onto crystalline SnO_2 nanowires grown on stainless steel substrate in 2010 and observed its electrochemical performance. A specific capacitance (based on MnO_2) as high as 637 F/g was obtained at a scan rate of 2 mV/s (800 F/g at a current density of 1 A/g) in 1 M Na_2SO_4 aqueous solution was observed. The energy density and power density measured at 50 A/g were 35.4 Wh/kg and 25 kW/kg, respectively, demonstrated the good rate capability. In addition, the SnO_2/MnO_2 composite electrode showed excellent long-term cyclic stability (less than 1.2% decrease of the specific capacitance was observed after 2000 CV cycles) [54].

In spite of so many efforts to explore the capacity of graphene based manganese oxide or tin oxide nanocomposites in dye removal or electrochemical charge storage, so far we could not find any work devoted to examine the effect of the combined presence of manganese oxide and tin oxide nanoparticles on graphene i.e. graphene/manganese oxide/tin oxide ternary nanocomposite. Besides, ternary nanocomposite of other metal oxides with graphene has shown superior behaviours [55-57]. Hence, this work has been devoted to synthesize a graphene based ternary nanocomposite of manganese oxide and tin oxide and explore their performance in the mentioned areas of application.

1.2 Objectives

The main objectives of the present work was to-

(i) Synthesize a Graphene/Mn-oxide/Sn-oxide ternary nanocomposite.
(ii) Evaluate the morphology of the synthesized nanocomposite.
(iii) Justify the potential of the nanacomposite in dye decolourization and specific capacitance.
(IV) Present a new material for environmental pollution prevention with high specific capacitance.

1.3 Outline of the Work

The ternary nanocomposite was synthesized using graphene oxide (GO) as precursor, following wet-chemical route. GO was synthesized from graphite powder following Hummers method [58]. Next, manganese oxide was grown on GO surface from reaction between manganese acetate and potassium permanganate using Isopropyl alcohol-water soft route. The manganese oxide furnished graphene oxide (GO) was converted to reduced graphene oxide (rGO) by introducing stannous chloride in its aqueous solution which at the same time converted itself into stannic oxide. The product was annealed under N_2 inert atmosphere to increase the degree of crystallinity of the nanocomposite as well as to extend the degree of reduction of GO via thermal reduction. To compare the outcome of the rGO/Mn-oxide/Sn-oxide ternary nanocomposite, two corresponding binary nanocomposites namely rGO/Mn-oxide and rGO/Sn-oxide was also prepared. Fourier transform infrared spectroscopy (FTIR) was used to confirm the presence of relevant functional groups and bonds in the nanocomposites. Field emission scanning electron microscopy (FESEM) revealed their surface morphology where energy dispersive x-ray (EDX) was used for their elemental analysis. X-ray diffraction (XRD)

analysis detected the crystal phases of the nanocomposites and crystallite size and lattice parameters of the nanoparticles. Thermogravimetric analysis (TGA) showed the thermal stability of the nanocomposites. As a typical chemical behaviour, the effectiveness of the nanocomposites in organic pollutant removal was observed using UV-Vis absorption spectroscopy with methylene blue (MB) as a model dye. Initially, a stock solution was prepared, which was later used to prepare MB solution of the desired concentrations. The molar absorbance coefficient was calculated from calibration curve prepared for it. After establishing the equilibrium time of interaction for the ternary nanocomposite with MB solution, effect of contact time, pH and dose was studied with MB solution and the obtained results were compared with those of the binary nanocomposites obtained under same conditions. As an electrochemical behaviour, capacitive behaviour of the ternary nanocomposite was explored and was compared with its binary nanocomposites. A three electrode system including surface modified graphite electrode as working electrode, glassy carbon electrode as counter electrode and calomel electrode as reference electrode was used in an aqueous solution of sodium sulfate. Cyclic voltammetry (CV) was used to find the suitable potential window and chronopotentiometry (CP) was used to obtain specific capacitance. Cyclic stability was also studied for first few cycles using CP where electrical impedance spectroscopy (EIS) was used for understanding the electrochemical processes occurred at electrode surface and drawing equivalent circuit from it.

References

1. Dobrzanski, L. A., "Significance of materials science for the future development of societies", *J. Mater. Process. Technol.*, vol. 175(1-3), pp. 133-148, 2006.
2. Schwarzenbach, R. P., Egli, T., Hofstetter, T. B., Gunten, U. and Wehrli, B., "Global water pollution and human health", *Annu. Rev. Environ. Resour.*, vol. 35(1), pp. 109-136, 2010.
3. Dewan, A. F., Kabir, M. H., Nahar, K. and Rahman, M. Z., "Urbanization and environmental degradation in Dhaka metropolitan area of Bangladesh", *Int. J. Environ. Sust. Dev."*, vol. 11(2), pp. 118-147, 2012.
4. Vörösmarty, C. J., McIntyre, P. B., Gessner, M. O., Dudgeon, D., Prusevich, A., Green, P., Glidden, S., Bunn, S. E., Sullivan, C. A., Liermann, C. R. and Davies, P. M., "Global threats to human water security and river biodiversity", *Nature*, vol. 467, pp. 555-561, 2010.
5. Schwarzenbach, R. P., Escher, B. I., Fenner, K., Hofstetter,T. B., Johnson, C. A., Gunten, U. and Wehrli, B., "The challenge of micropollutants in aquatic systems", *Science,* vol. 313, pp. 1072-1077, 2006.
6. Rosegrant, M. W. and Cline, S. A., "Global food security: challenges and policies", *Science*, vol. 302, pp. 1917-1919, 2003.
7. Khalequzzaman, M., "Sustainable development of water resources in Bangladesh in the context of planetary boundaries and environmental performance index", presented at Int. Conf. on Sust. Dev., Columbia University, NYC, 2015.
8. Kant, R., "Textile dyeing industry an environmental hazard", *Nat. Science*, vol. 4(1), pp. 22-26, 2012.
9. Forgaces, E., Cserhatia, T. and Orsb, G., "Removal of synthetic dyes from wastewaters: a review", *Environ. Int.*, vol. 30, pp. 953-971, 2004.
10. Crini, G., "Non-conventional low-cost adsorbents for dye removal: A review", *Bioresour. Technol.,* vol. 97(9), pp. 1061-1085, 2006.
11. Guptaa, V. K., Pathaniac, D. and Singhc P., "Adsorptional photocatalytic degradation of methylene blue onto pectin–CuS nanocomposite under solar light", *J. Hazard. Mater.*, vol. 243, pp. 179-186, 2012.
12. Li, Y., Dua, Q., Liua, T., Pengb, X., Wanga, J., Suna, J., Wanga, Y., Wua, S., Wanga, Z., Xiaa, Y. and Xiaa, L., "Comparative study of methylene blue dye adsorption onto activated carbon, graphene oxide, and carbon nanotubes", *Chem. Eng. Res. Des.*, vol.

91, pp. 361-368, 2013.

13. Kannan, N. and Sundram, M. M., "Kinetics and mechanism of removal of methylene blue by adsorption on various carbons—a comparative study", *Dyes and Pigments*, vol. 51, pp. 25-40, 2001.
14. Chowdhury, A. N., Azam, A. S., Aktaruzzaman, M. and Rahim, A., "Oxidative and antibacterial activity of Mn_3O_4", *J. Hazard. Mater.*, vol. 172, pp. 1229-1235, 2009.
15. Yaoa, Y., Miaoa, S., Liub, S., Li, P. M., Sunb, H. and Wang, S., "Synthesis, characterization, and adsorption properties of magnetic Fe_3O_4@graphene nanocomposite", *Chem. Eng. J.*, vol. 184, pp. 326-332, 2012.
16. Okpala, C. C., "Nanocomposites – an overview", *Int. J. of Eng. Res. and Dev.,* vol. 8(11), pp. 17-23, 2013.
17. Nanda, J., Martha, S. K. and Yanaraman, R. K., "High-capacity electrode materials for electrochemical energy storage: role of nanoscale effects", *Pramana – J. Phys.*, vol. 84, pp. 1073-1086, 2015.
18. Pasta, M., Wessells, C. D., Huggins, R. A. and Cui, Y., "A high-rate and long cycle life aqueous electrolyte battery for grid-scale energy storage", *Nat. Commun.*, vol. 1149, pp. 1-7, 2012.
19. Simon, P. and Gogotsi, Y., "Materials for electrochemical capacitors", *Nat. Mater.*, vol. 7, pp. 845-854, 2008.
20. Griggs, D., Smith, M. S., Gaffny, O., Rockstorm, J., Ohman, M. C., Shyamsunder, P., Steffen, W., Glaser, G., Kanie, N. and Noble, I., "Policy: sustainable development goals for people and planet", *Nature*, vol. 495, pp. 305-307, 2013.
21. Moran, D. D., Wackernagela, M., Kitzesa, J. A., Goldfingera, S. H. and Boutaudc, A., "Measuring sustainable development — nation by nation", *Ecol. Econ.*, vol. 64, pp. 470-474, 2008.
22. Camargo, P. H. C., Satyanarayana, K. G. and Wypych, F., "Nanocomposites: synthesis, structure, properties and new application opportunities", *Mat. Res.*, vol. 12(1), pp. 1-39, 2009.
23. Novoselov, K. S., Geim, A. K., Morozov, S. V., Jiang, D., Zhang, Y., Dubonos, S. V., Grtigorieva, I. V. and Firsov, A. A., "Electric field effect in atomically thin carbon films", *Science*, vol. 306(5696), pp. 666-669, 2004.
24. Novoselov, K. S., Jiang, D., Schedin, F., Booth, T. J., Khotkevich, V. V., Morozov, S. V. and Geim, A. K., "Two-dimensional atomic crystals", *Nat. Sci.*, vol. 102(30),

pp. 10451-10453, 2005.

25. Savage, N., "Super carbon", *Nature,* vol. 483, pp. 1-2, 2012.
26. Singh, V., Joung, D., Zhai, L., Das, S., Khondoker, S. I. and Seal, S., "Graphene based materials: past, present and future", *Prog. Mater. Sci.* vol. 56, pp. 1178-1271, 2011.
27. Sharmas, R., Baik, J. H., Perera, C. J. and Strano, M. S., "Anomalously large reactivity of single graphene layers and edges toward electron transfer chemistries", *Nano. Lett.,* vol. 10, pp. 398-405, 2010.
28. Rao, C. N. R., Sood, A. K., Subrahmanyam, K. S. and Govindaraj, A., "Graphene: the new two-dimensional nanomaterial", *Angew. Chem. Int. Ed.*, vol. 48, pp. 7752-7777, 2009.
29. Park, S. and Ruoff, R. S., "Chemical methods for the production of graphenes", *Nat. Nanotechnol.,* vol. 4, 217-224, 2009.
30. Lee, C., Wei, X. and Hone, J., "Measurement of the elastic properties and intrinsic strength of monolayer graphene", *Science,* vol. 321, pp. 385-388, 2008.
31. Bae, S., Kim, H., Lee, Y., Xu, X., Park, J., Zheng, Y., Balakrishnan, J., Lei, T., Kim, H. R., Song, Y., Kim, Y, Kim, K., Ozyilmaz, B., Anh, J., Hong, B. H. and Iijima, S., "Roll-to-roll production of 30-inch graphene films for transparent electrodes", *Nat. Nanotechnol.,* vol. 5, pp. 574-578, 2010.
32. Luo, J., Kim, J. and Huang, J., "Material processing of chemically modified graphene: some challenges and solutions", *Acc. Chem. Res.*, vol. 46(10), pp. 2225-2234, 2013.
33. Wanga, B., Wanga, Y., Park, J., Ahnb, H. and Wanga, G., "In situ synthesis of Co_3O_4/graphene nanocomposite material for lithium-ion batteries and supercapacitors with high capacity and supercapacitance", *J. Alloys Comp.*, vol. 509, pp. 7778–7783, 2011.
34. Amini, M., Nyeri, S., Pashaeic, B. and Bagherzadeh, M., "Nano-layered manganese oxides as low-cost, easily synthesized, environmentally friendly and efficient catalysts for epoxidation of olefins", *RSC Adv.*, vol. 2, pp. 3654–3657, 2012.
35. Suscak, P., "Tin oxides: an abundance of uses", *Tin Inter.*, vol. 72(7), pp. 6-8, 2000.
36. Quian, Y., Lu, S. and Gao, F., "Preparation of MnO_2/graphene composite as electrode material for supercapacitors", *J. Mater. Sci.,* vol. 46, pp. 3517-3522, 2011.
37. Qu, J., Shi, L., He, C., Gao, F., Li, B., Hu, H., Shao, G. and Wang, X., Qiu, J., "Highly efficient synthesis of graphene/MnO_2 hybrids and their application for ultrafast oxidative decomposition of methylene blue", *Carbon,* vol. 66, pp. 485-492, 2014.

38. Ye, K., Liu, Z., Xu, C., Li, N., Chen, Y. and Su, Y., "MnO_2/reduced graphene oxide composite as high-performance electrode for flexible supercapacitors", *Inorg. Chem. Commun.*, vol. 30, pp. 1-4, 2013.
39. Huang, H., Sun, G., Hu, J. and Jiao, T., "Low temperature synthesis of MnO_2/graphene nanocomposites for supercapacitors", *J. of Chem.,* vol. 2015(629362), pp. 1-8, 2015.
40. Wen, L., Chen, G., Jiang, F., Zhou, X. and Yang, J., "A facile approach for preparing MnO_2-graphene composite as anode material for lithium-ion batteries", *Int. J. Electrochem. Sci.,* vol.10, pp. 3859 – 3866, 2015.
41. Wanga, B., Park, J., Wang, C., Ahn, H. and Wang, G., "Mn_3O_4 nanoparticles embedded into graphene nanosheets: preparation, characterization, and electrochemical properties for supercapacitors", *Electrochim. Acta,* vol. 55, pp. 6812-6817, 2010.
42. Wang, D., Li, Y., Wang, Q. and Wang, T., "Facile synthesis of porous Mn_3O_4 nanocrystal–graphene nanocomposites for electrochemical supercapacitors", *Eur. J. Inorg. Chem.*, vol. 2012, pp. 628-635, 2012.
43. Li, L., Seng, K. H., Liu, H., Nevirkovets, I. P. and Guo, Z., "Synthesis of Mn_3O_4 - encapsulated graphene sheet nanocomposites via a facile, fast microwave hydrothermal method and their supercapacitive behavior", *Electrochim. Acta*, vol. 87, pp. 801-808, 2013.
44. Fan, Y., Zhang, X., Liu, Y., Cai, Q. and Zhang, J., "One-pot hydrothermal synthesis of Mn_3O_4 /graphene nanocomposite for supercapacitors", *Mater. Lett.*, vol. 95, pp. 153-156, 2013.
45. Yao, Y., Xu, C., Yu, S., Zhang, D. and Wang, S., "Facile synthesis of Mn_3O_4−reduced graphene oxide hybrids for catalytic decomposition of aqueous organics", *Ind. Eng. Chem. Res.*, vol. 52, pp. 3637−3645, 2013.
46. Zhang, L., Zhao, L. and Lian, J., "Nanostructured Mn_3O_4–reduced graphene oxide hybrid and its applications for efficient catalytic decomposition of orange II and high lithium storage capacity", *RSC Adv.,* vol. 4, pp. 41838-41847, 2014.
47. Antihos, D., Pingmuang, K., Romano, M., S., Beirnea, S., Romeo, T., Aitchison, P., Minettd, A., Wallace, G., Phanichphant, S. and Chen, J., "Manganosite–microwave exfoliated graphene oxide composites for asymmetric supercapacitor device applications", *Electrochim. Acta*, vol. 101, pp. 99-108, 2013.

48. Xu, G., Jiang, F., Ren, Z. and Yang, L., "Polyhedral MnO nanocrystals anchored on reduced graphene oxide as an anode material with superior lithium storage capability", *Ceram. Inter*, vol. 41(9), pp. 10680-10688, 2015.
49. Li, F., Song, J., Yang, H., Gan, S., Zhang, Q., Han, D., Ivaska, A. and Niu, L., "One-step synthesis of graphene/SnO_2 nanocomposites and its application in electrochemical supercapacitors", *Nanotechnology*, vol. 20, 455602-455608, 2009.
50. Wang, X., Zhou, X., Zhang, J. and Liu, Z., "A SnO_2/graphene composite as a high stability electrode for lithium ion batteries", *Carbon,* vol. 49, pp. 133-139, 2011.
51. Seema, H., Kemp, K. C., Chandra, V. and Kim, K. S., "Graphene–SnO_2 composites for highly efficient photocatalytic degradation of methylene blue under sunlight", *Nanotechnology*, vol. 23, pp. 1-8, 2012.
52. Shanmugam, M. and Jayavel, R., "Synthesize of graphene-tin oxide nanocomposite and its photocatalytic properties for the degradation of organic pollutants under visible light", *J. Nanosci. Nanotechnol.* , vol. 15, pp. 7195–7201, 2015.
53. Velmurugana, V., Srinivasaraoa, U., Ramachandrana, R., Saranyaa, M., Santhosha, C., Gracea, A. N., "Synthesis of tin oxide/graphene (SnO_2/G) nanocomposite and its electrochemical properties for supercapacitor applications", *Mater. Res. Bull.*, vol. 84, pp. 145-151, 2016.
54. Yan, J., Khoo, E., Sumboja, A., Lee, P.S., "Facile coating of manganese oxide on tin oxide nanowires with high-performance capacitive behavior", *ACS Nano,* vol. 4(7), pp. 4247-4255, 2010.
55. Lian, P., Liang, S., Zhub, X., Yang, W. and Wang, H., "A novel Fe_3O_4–SnO_2–graphene ternary nanocomposite as an anode material for lithium-ion batteries", *Electrochim. Acta*, vol. 58, pp. 81-88, 2011.
56. Lin, Y., Geng, Z., Cai, H., Ma, L., Chen, J., Zeng, J., Pan, N. and Wang, X., "Ternary graphene–TiO_2–Fe_3O_4 nanocomposite as a recollectable photocatalyst with enhanced durability", *Eur. J. Inorg. Chem.,* vol. 2012, pp. 4439–4444, 2012.
57. Almeida, B. M., Bettini, J., Benedetti, J. E. and Nogueira, A. F., "A novel nanocomposite based on TiO_2/Cu_2O/reduced graphene oxide with enhanced solar-light-driven photocatalytic activity", *Appl. Surf. Sci.,* vol. 324, pp. 419-431, 2015.
58. Hummers, W. S., and Offeman, R. E., "Preparation of graphitic oxide", *J. Am. Chem. Soc*., vol. 80, pp. 1339-1339, 1958.

Chapter 2

Background

2.1 Graphene

2.1.1 Introduction

Graphene, a single atomic layer of carbon, is the first material of the class of two-dimensional (2D) crystalline materials and the best studied carbon allotrope [1]. Graphene yields extraordinary thermal, mechanical, and electrical properties, which have long been the interest of many theoretical studies and has attained the central position as a 'miraculous' material in the beginning of the 21st century [2].

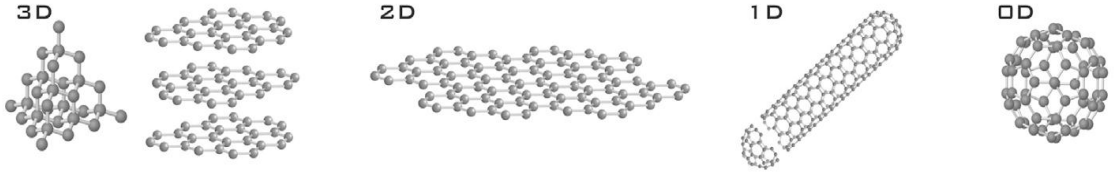

Fig. 2.1- Crystal structures of the different allotropes of carbon - (left to right) diamond and graphite (3D); graphene (2D); nanotubes (1D); and buckyballs (0D) [1]

The theory of graphene was first explored by P. R. Wallace in 1947 as a starting point for understanding the electronic properties of 3D graphite. The term 'graphene' was introduced by Hanns-Peter Boehm and first appeared in 1987 to describe single sheets of graphite as a constituent of graphite intercalation compounds (GICs) [3-4]. However, the credit of true discovery of graphene belongs to A. Geim and K. Novoselov who extracted single sheet graphene from 3D graphite using micromechanical cleavage technique in 2004 and received noble prize in physics in 2010 for this breakthrough discovery [1, 5].

2.1.2 Structure and Properties

Graphene is a one-atom-thick planar sheet of sp^2-bonded carbon atoms in form of a honeycomb lattice, and it is essentially building-block material for graphitic materials such as fullerene, carbon nanotube and graphite [6].

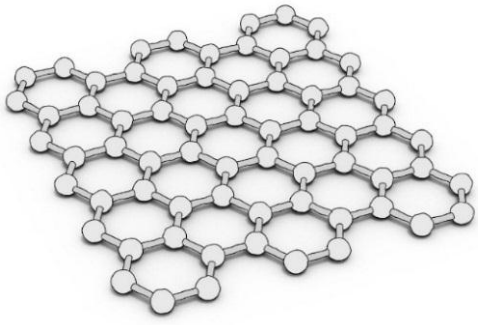

Fig. 2.2- Sheet like atomic structure of graphene

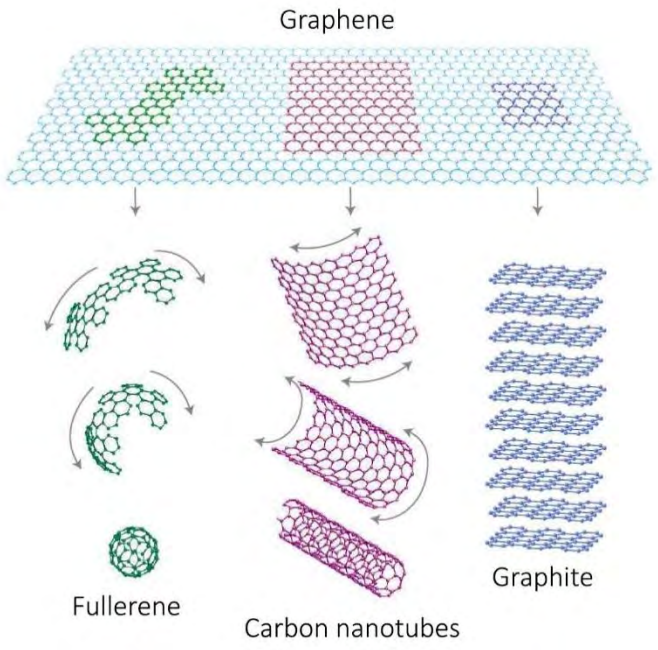

Fig. 2.3- Graphene as a basic building-block material for graphitic materials such as fullerene, carbon nanotube and graphite [6]

The 2s, $2p_x$ and $2p_y$ orbitals in each carbon atom of graphene are mixed with together to form three sp^2-hybrid orbitals. Three sp^2-hybrid orbital electrons form extremely strong in-plane σ-bonds with three nearest neighbor atoms in the basal plane of graphene. The fourth valence electron lies in the $2p_z$ orbital that is oriented perpendicular to the graphene plane and forms delocalized π-bond, which leads to electrical conductivity [7].

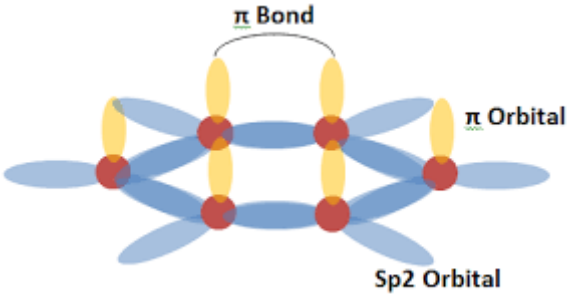

Fig. 2.4- Schematic sp^2-hybridized C-C bond structure of graphene containing in-plane σ-bonds and perpendicular π-bonds

Graphene was first isolated from graphite by Geim and Novoselov at the University of Manchester in 2004. According to their study, graphene demonstrated ambipolar electric-field effect with a high value of charge carrier mobility (~ 10,000 $cm^2V^{-1}s^{-1}$) at ambient temperature [8]. It is reported that, graphene possess superior charge carrier mobility of 2,00,000 $cm^2V^{-1}s^{-1}$ at low-temperature for charge carrier density below 5×10^9 cm^{-2}, which cannot be obtained in semiconductors or non-suspended graphene [9]. It has been

found that the charge carrier mobility decreases with the increase of layer of graphene [10]. The thermal conductivity measurements have shown that the suspended single-layer graphene sheet exhibits extremely high thermal conductivity value of 5000 $Wm^{-1}K^{-1}$ [11]. The measurements have shown that the white light opacity of a suspended single-layer graphene sheet is 2.3 ± 0.1% with a negligible reflectance (< 0.1%) whereas the opacity is independent of wavelength and increases linearly with the increase of the number of layers from 1 to 5 [12]. Besides, graphene exhibits other superior properties such as fracture strength (125 GPa) [13], Young's modulus (~ 1100 GPa) [13], and large specific surface area (2630 m^2g^{-1}) [14].

2.2 Synthesis of Graphene

Four most common routes for synthesis of graphene are mechanical exfoliation, epitaxial growth, chemical vapour deposition and reduction of graphene oxide, which are either top-down or bottom-up strategy. The top-down strategy is the breaking down of graphite into graphene and bottom-up strategy is the building up of graphene using carbon atoms.

2.2.1 Mechanical Exfoliation

In 2004, Geim's group reported the exfoliation of monolayer graphene and transferring it onto a 300 nm silicon dioxide substrate using mechanical exfoliation technique [8]. In this method, an isolated graphene can be produced by peeling it off from highly oriented pyrolytic graphite (HOPG) using a Scotch tape. The advantage with this technique is that the individual graphene sheet prepared by this technique has high quality, while the disadvantage is that this technique is not suitable for large-scale production.

2.2.2 Epitaxial Growth

Epitaxial growth technique is one of the bottom-up strategies to produce graphene sheets. Generally, a silicon carbide (SiC) is heated to the temperature higher than $1000^{o}C$ under ultra-high vacuum. In these conditions, the silicon atoms desorb from the surface of silicon carbide, and the carbon atoms left behind rearrange to create few layers of graphene [15-17]. The major advantages with this method are that it has potential to be used for large-scale production, and the epitaxial graphene on SiC can be used for immediate implementation in electronic devices. However, the epitaxial few-layer graphene grown on SiC substrate is not uniform on thickness and the electronic properties of the epitaxial graphene depend upon its thickness.

2.2.3 Chemical Vapour Deposition

Chemical vapour deposition (CVD) technique is another bottom-up strategy to produce monolayer or few-layer graphene. Generally, carbon atoms can be segregated from hydrocarbon gas (for example, CH_4 or C_2H_2) and adsorbed on the surface of a metal catalytic substrate (such as nickel [18], cobalt [19] and copper [20]), and hence create monolayer or few-layer graphene under high temperature and high vacuum. The thickness and quality of graphene layers can be controlled by varying the cooling rate, and the concentration of carbon atoms diffused into the metal substrate [21].

2.2.4 Graphene from Graphene Oxide (GO)

Graphite flakes can be oxidized in the presence of strong acids and oxidizing agents. The carbon planes of graphite oxide are heavily functionalized with oxygen-containing groups. Due to these oxygen-containing groups, graphite oxide can be easily exfoliated to individual graphene oxide sheets by sonication in water or rapid heating process, which is very suitable for the synthesis of graphene based materials. Due to various advantage, GO is ultimately reduced to graphene which is generally termed as reduced GO (rGO), as the complete removal of the oxygen-containing groups has not yet been achieved [22-23]. There are a number of strategies for the reduction of GO.

2.2.4.1 Thermal Annealing Reduction

GO is thermally unstable and can be reduced by heat treatment, and the process is called thermal annealing reduction. Rapid heating (>2000ºC/min) can exfoliate and reduce

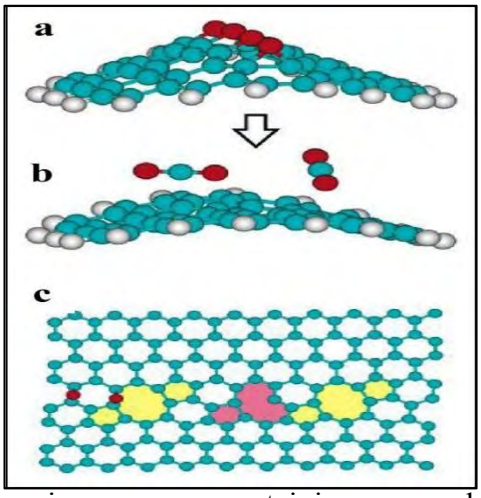

Fig. 2.5- a) GO contain various oxygen containing groups b) CO_2 is released during thermal treatment and it leaves c) vacancies and defects on the carbon grid [25]

graphite oxide, yielding a black powder [24-25]. The exfoliation and reduction of graphite oxide are mainly due to the decomposition of oxygen-containing groups at high

temperature and the sudden generation of CO or CO_2 gases within the space between graphite oxide sheets, which generates a high pressure (130 MPa at 1000 ^oC) to separate the graphene sheets from each other [25]. The main disadvantage is that carbon atoms removed from the carbon plane during the thermal reduction process (by releasing carbon dioxide), splits the carbon plane of graphene into the pieces with small size, and makes vacancies and topological defects, leading to poor electrical conductivity [24, 26-27].

2.2.4.2 Chemical Reduction

The solution-based process to produce monolayer graphene sheets from GO was firstly demonstrated by Ruoff and his group using hydrazine hydrate as reducing agent [28-29]. In this way, first GO is produced from graphite flake. Graphene sheets can be obtained by chemical reduction of these graphene oxide sheets [30]. Several reducing agents have been used for the reduction of graphene oxide such as hydrazine hydrate [28-29], sodium borohydride [31] and hydroiodic acid [32]. Chemical reduction is usually carried out at ambient temperature or by using moderate heating, which makes it a low-cost and easy way to produce large-scale graphene compared with thermal annealing reduction.

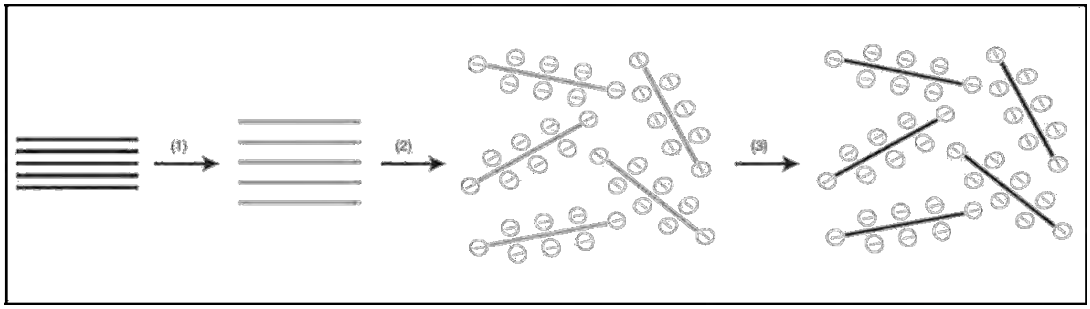

Fig. 2.6- Schematic illustration of the chemical approach to synthesis of aqueous graphene dispersion - 1) oxidization of graphite (black blocks) to graphite oxide (gray blocks) and increasing the interlayer distance of sheets 2) sonication of graphite oxide to exfoliate and obtain colloidal GO 3) Chemical reduction of GO colloids to obtain a conductive graphene colloids [30].

2.2.4.3 Electrochemical Reduction

Electrochemical reduction of GO is a very attractive method to produce a graphene-film due to its fast, easy, green nature and does not require the use of any toxic reducing agents (such as $NaBH_4$ and N_2H_4). The pre-deposited GO film on a substrate (gold, glassy carbon electrode, ITO, etc.) can be reduced by applying a constant DC voltage [33] or a DC bias using cyclic voltammetry technique [34].

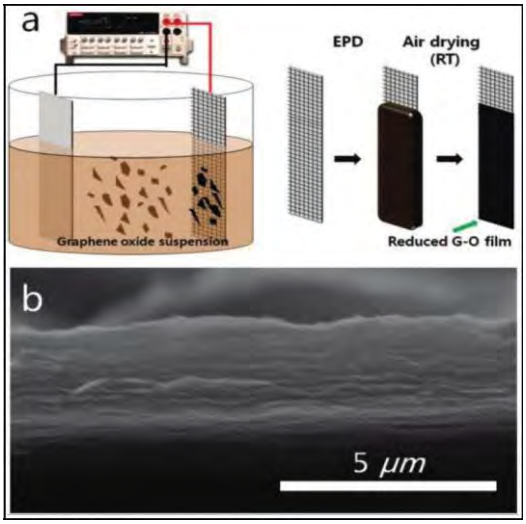

Fig. 2.7- (a) Schematic illustration of the electrophoretic deposition process and b) cross-sectional SEM image of electrophoretic deposited GO film [35]

2.3 Graphene Oxide: Preparation Methods and Structure

Back to the history, Brodie reported the preparation of graphite oxide by oxidizing graphite with potassium chlorate ($KClO_3$) in fuming nitric acid (HNO_3) in 1859 [36]. After 40 years, L. Staudenmaier improved the Brodie's method by modification, in which adding a concentrated sulfuric acid to the reaction that increases the acidity of the reaction mixture. They also added potassium chlorate in multiple aliquots in the reaction mixture over the course of the reaction [37]. In 1957, Hummers and Offeman developed a rapid and relatively safe method where graphite is oxidized by reacting with an anhydrous mixture of potassium permanganate ($KMnO_4$), sodium nitrate ($NaNO_3$) and concentrated sulfuric acid (H_2SO_4) [38].

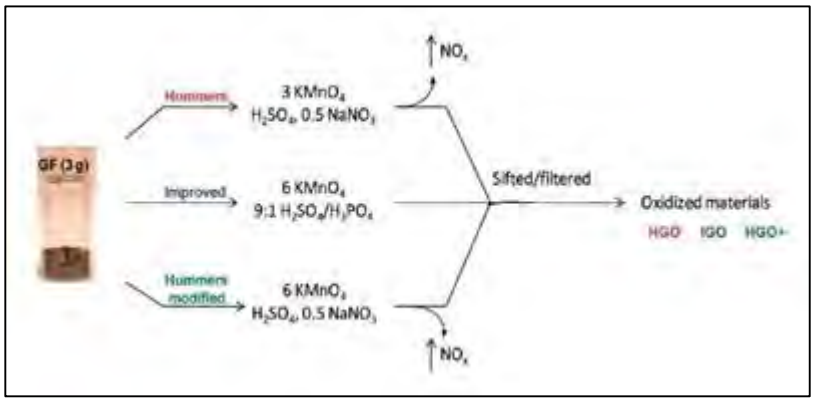

Fig. 2.8- Procedure comparison of different methods to produce GO from graphite [39]

Since graphene was first isolated by Geim and Novoselov at the University of Manchester in 2004, graphite oxide has attracted attention as a precursor for the low-cost and large-

scale production of graphene-based materials and a lot of publications have been reported about its synthesis, structure, reduction and applications. To improve the preparation procedure of GO, Tour and coworkers reported a new recipe for the preparation of GO in 2010 [39]. They excluded sodium nitrate ($NaNO_3$) from the reaction, increased the amount of potassium permanganate ($KMnO_4$) and introduced phosphoric acid (H_3PO_4) into the reaction in a 9:1 mixture of H_2SO_4/H_3PO_4. It is believed that, GO prepared by this method has higher level of oxidation with more intact graphitic basal planes compared to GO prepared by Hummer's method.

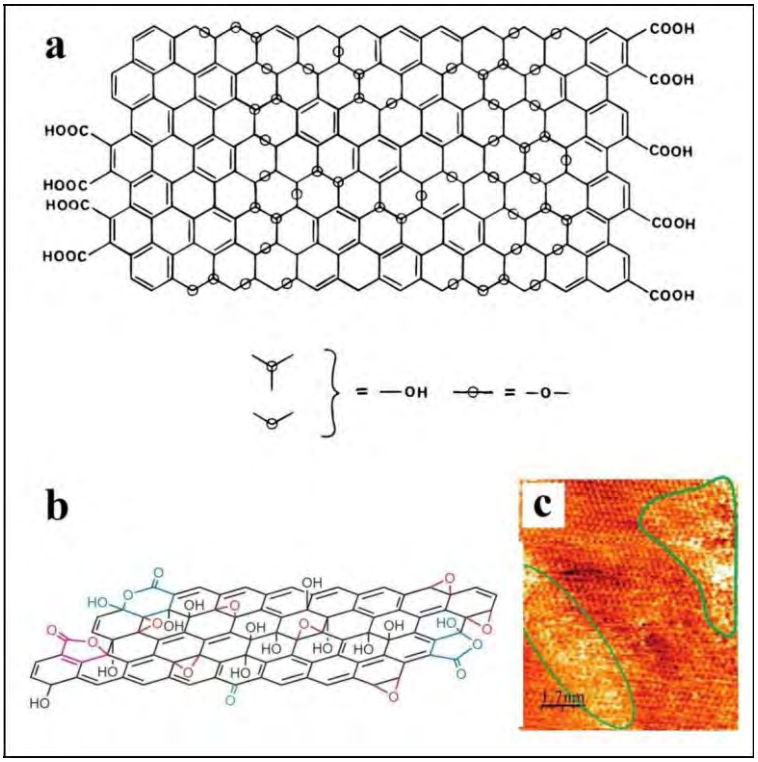

Fig. 2.9- (a) Lerf and Klinowski model for GO (b) STM image of a GO monolayer, which shows the oxidized and unoxidized regions (c) New structural model for GO, which suggests five- and six-membered lactol rings [40-42]

Although, it has been investigated over a century, the precise chemical structure of GO is still the subject for considerable debate and there is no unambiguous model. It is related to the complexity of GO due to its amorphous character. In 1998, Lerf and Klinowski proposed a nonstoichiometric model for GO [40]. In this model, the carbon plane of graphite is decorated with epoxy (1, 2-ether instead of 1, 3-ether, which suggested by Mermoux) and hydroxyl groups, which they are very close to one another. Carbonyl groups can be found on the edge of the plane most likely as carboxylic acids and within the plane as organic carbonyl defects. These functional groups decorate both sides of the

surface of GO. Recently, Gao et al. showed the presence of five- and six-member-ring lactols on the periphery of GO plane by interpreting nuclear magnetic resonance (NMR) spectroscopy data [41]. According to the Lerf and Klinowski model, GO contains two kinds of regions consisted of aromatic regions with unoxidized benzene rings and regions contain oxidized six-member rings, which are distributed randomly on the surface of GO. The degree of oxidation affects the size of both regions. The scanning tunneling microscopy (STM) study on the surface of GO confirmed the presence of both regions with a few nanometer sizes [42].

2.4 Nanocomposites

Nanocomposites are composites in which at least one of the phases shows dimensions in the nanometer range (1 nm = 10^{-9} m) [43]. Nanocomposite materials have emerged as suitable alternatives to overcome limitations of microcomposites and monolithics, while posing preparation challenges related to the control of elemental composition and stoichiometry in the nanocluster phase. They are reported to be the materials of 21st century in the view of possessing design uniqueness and property combinations that are not found in usual composites. The general understanding of these properties is yet to be reached [44], although the first inference on them was reported as early as 1992 [45].

2.5 Graphene-based Nanocomposites

Graphene's high electrical conductivity, large surface-to-volume ratio, and excellent chemical tolerance make it an attractive matrix for composites. In 2006, Ruoff et al. reported the first graphene-based nanocomposite, a graphene-polystyrene composite [46]. According to their results, incorporation of the graphene sheets with polystyrene enhanced the electrical conductivity of the composite. This achievement has introduced a new class of graphene-based composite materials. According to the second component in the composites, graphene-based nanocomposite can be classified into two main categories-

1) Graphene-based polymer nanocomposites
2) Graphene-based inorganic nanocomposites

2.6 Graphene-based Inorganic Nanocomposites

The novel catalytic, magnetic and optoelectronic properties of graphene nanocomposites based on the hybridization with inorganic nanoparticles (NPs) have attracted significant attention [47]. Due to the enhanced electrical and electronic properties and the synergistic

effect between graphene and inorganic nanoparticles, graphene/nanoparticle nanocomposites offer greater potential for various applications.

According to the kind of inorganic components, graphene-based inorganic nanocomposites can be classified into four categories:

1) Graphene-based metal nanocomposites
2) Graphene-based metal compound nanocomposites
3) Graphene-based nonmetal nanocomposites
4) Graphene-based carbon material nanocomposites

Graphene has been extensively integrated with different metal compounds such as metal oxides (such as MnO_2 [48], SnO_2 [49], ZnO [50], TiO_2 [51], Fe_3O_4 [52], NiO [53], etc.), metal sulphides (such as CdS [54], ZnS [55], PbS [56], etc.), metal selenides (such as CdSe [57]) metal hydroxides (such as MnOOH [58], $Co(OH)_2$ [59], $Ni(OH)_2$ [60]) etc). It has been demonstrated that the charge-transferring, and magnetic and electronic interactions between graphene sheets and the attached metal compound nanostructures can improve their performance in various applications.

2.7 Synthesis of Graphene-Inorganic Nanocomposites

The graphene-based inorganic nanocomposites are usually prepared by using different strategies:

1) ***Ex situ* hybridization**, hybridization of pre-synthesized nanomaterials with graphene oxide or reduced graphene oxide.
2) ***In situ* formation**, formation or crystallization of nanomaterials in the presence of graphene oxide, reduced graphene oxide or functionalized graphene nanosheets, and growing on the surface of them.

2.7.1 *Ex situ* Hybridization

In this strategy, first, nanomaterials (such as nanoparticles, nanowires, nanorods or, etc.) are synthesized before mixing with graphene-based nanosheets. The surface of graphene and/or nanomaterials are usually modified, which can bind with together through either covalent bonding [61-62] or non-covalent interactions [63] (such as π-π stacking, or electrostatic interactions [64]).

2.7.2 *In situ* Formation

Ex situ hybridization strategy involves multiple steps, which results in the complexity of

the preparation process. Compared to the e*x situ* hybridization strategy, *in situ* formation or crystallization strategy is a simple and usually one-step process. Another advantage of this strategy is that the using surfactants or polymer for modification of graphene and/or nanomaterials could be eliminated, which may influence the performance of the nanocomposites. In addition, in this strategy, a variety of techniques can be utilized, including chemical reduction methods, sol-gel techniques, solvothermal / hydrothermal routes, electrochemical deposition techniques, sonochemical method.

2.7.2.1 Chemical Reduction Method

The in situ chemical reduction method is the most common way to the synthesis of graphene-based inorganic nanocomposites. The attraction of metal ions onto the surface of graphene oxide is the initial step for the nucleation of the nanostructures on the surface of graphene, which can be prepared by mixing a precursor of metal with a solution of GO. These attracted metal ions can be easily reduced by common reducing agents such as $NaBH_4$, amines and ascorbic acid, in which GO could also be reduced simultaneously [65]. If, GO does not reduce during the reduction of metal ions on the surface of GO, there are two ways to address this problem-

1) Using additional reducing agents for reducing GO
2) Using rGO instead of GO.

2.7.2.2 Hydrothermal / Solvothermal Routes

Hydrothermal and solvothermal are powerful synthesis approaches for the formation of a variety of inorganic nanostructures. Recently, these methods have been frequently used for the synthesis of graphene-based inorganic nanocomposites [66-67]. These routes were usually operated at elevated temperature of solutions (aqueous solution for hydrothermal and non-aqueous solution for solvothermal) with high vapour pressure in a sealed vessel called the autoclave. As mentioned, the reaction carried out in a sealed autoclave with a confined volume, so the elevated temperature increases the vapor pressure above the critical pressure, which facilitates the crystal growth of initial nucleation sites. The main advantage of hydrothermal synthesis is feasible in producing desired nanostructures such as nanoparticles, nanowires and nanorods with high crystallinity without the need of post-synthetic annealing. Concurrently, it enables the reduction of GO to rGO [68].

2.7.2.3 Electrochemical Deposition

Electrochemical approach for deposition of variety of inorganic crystals on different

substrates is a very attractive method to produce thin-films due to its fast, easy and green nature. Recently, different electrochemical deposition techniques have been utilized for the fabrication of graphene-based noble metal nanocomposites such as Au [69-70], however, the process involves multi-step.

2.7.2.4 Sonochemical Method

Sonochemical method has been proven to be a versatile and promising technique in the synthesis of a variety of nanostructures. The chemical effects of ultrasound irradiation arise from acoustic cavitation phenomenon. When a liquid is irradiated with ultrasound, bubbles are created, which accumulate the ultrasonic energy while growing. The unstable gas-liquid interface subsequently collapsed, releasing the stored energy within a very short time. These cavitational implosions generate localized hotspots with a high temperature of 5000 K, a pressure of 1000 bar, and a heating and cooling rate of 10^{10} K/s [71]. Different parameters such as ultrasonic irradiation time, frequency, concentration and various organic additives can affect the shape and size of nanostructures [72-73].

2.8 Application of Graphene-Inorganic Nanocomposites

Functionalization of the intriguing two-dimensional nanosheets is expected not only to enhance the performance of graphene and nanocrystals, but also to display novel advantages resulting from the interaction between the materials. It is found that graphene-based inorganic nanocomposites show enhanced performance in the field of dye removal, electrochemical capacitor, solar cell, battery, sensors, catalysis, pollutant removal and other interesting applications.

2.8.1 Dye Removal

2.8.1.1 Dye

A dye is a colored substance that has an affinity to the substrate to which it is being applied. The dye is generally applied in an aqueous solution, and requires a mordant to improve the fastness of the dye on the fiber [74-75]. The process of dying has been known to human since a long time ago. According to various archaeological evidence found so far, it can be concluded that that, particularly in India and Phoenicia, dyeing has been widely carried out for over 5,000 years. The dyes were obtained from animal, vegetable or mineral origin, with none to very little processing. By far the greatest source of dyes has been from the plant kingdom, but only a few have ever been used on a commercial scale.

2.8.1.2 Types of Dyes

Primarily dyes are classified depending upon their sources. From that perspectives there are two types of them e.g. natural and synthetic dyes [76-77].

The majority of natural dyes are from plant sources – roots, berries, bark, leaves, and wood, fungi, and lichens. Textile dyeing dates back to the Neolithic period. Throughout history, people have dyed their textiles using common, locally available materials. Plant-based dyes such as wood, indigo, saffron, and madder were raised commercially and were important trade goods in the economies of Asia and Europe. Across Asia and Africa, patterned fabrics were produced using resist dyeing techniques to control the absorption of color in piece-dyed cloth. The discovery of man-made synthetic dyes late in the 19th century ended the large-scale market for natural dyes.

The first human-made organic dye, mauveine, was discovered serendipitously by William Henry Perkin in 1856, the result of a failed attempt at the total synthesis of quinine. Many thousands of synthetic dyes have since been prepared. Synthetic dyes quickly replaced the traditional natural dyes. They cost less, they offered a vast range of new colors, and they imparted better properties to the dyed materials.

Most commonly dyes are classified according to how they are used in the dyeing process [76]. Some of them are acid dyes, basic dyes, substantive dye, mordant dye, vat dye, reactive dye, azoic dye, food dye etc. Among them acid dyes and basic dyes are mostly discussed.

Acid dyes are water-soluble anionic dyes that are applied to fibers such as silk, wool, nylon and modified acrylic fibers using neutral to acid dye baths. Attachment to the fiber is attributed, at least partly, to salt formation between anionic groups in the dyes and cationic groups in the fiber. Acid dyes are not substantive to cellulosic fibers. Most synthetic food colors fall in this category. On the other hand, basic dyes are water-soluble cationic dyes that are mainly applied to acrylic fibers, but find some use for wool and silk. Usually acetic acid is added to the dye bath to help the uptake of the dye onto the fiber. Basic dyes are also used in the coloration of paper.

2.8.1.3 Methylene Blue (MB)

Methylene blue is a heterocyclic aromatic chemical compound with the molecular

formula $C_{16}H_{18}N_3SCl$ and its IUPAC name is 3, 7-bis (Dimethyl amino)-phenothiazin-5-ium chloride. Chemically, it's a basic cationic dye [78].

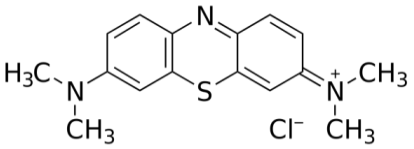

Fig. 2.10- Chemical structure of methylene blue

It has many uses in a range of different fields, such as biology and chemistry. At room temperature it appears as a solid, odourless, dark green powder that yields a blue solution when dissolved in water.

Methylene blue is widely used as a redox indicator in analytical chemistry. Solutions of this substance are blue when in an oxidizing environment, but will turn colorless if exposed to a reducing agent.

In biology methylene blue is used as a dye for a number of different staining procedures, such as Wright's stain and Jenner's stain. Since it is a temporary staining technique, methylene blue can also be used to examine RNA or DNA under the microscope or in a gel: as an example, a solution of methylene blue can be used to stain RNA on hybridization membranes in northern blotting to verify the amount of nucleic acid present. It can also be used as an indicator to determine if eukaryotic cells such as yeast are alive or not.

Table 2.1- Effect of MB on human health

Cardiovascular	**Central Nervous System**	**Dermatologic**	**Gastro-intestinal**	**Genito-urinary**	**Hemato-logic**
• Hypertension • Precordial pain	• Dizziness • Mental confusion • Headache • Fever	• Staining of skin • Injection site necrosis (SC)	• Fecal discoloration • Nausea • Vomiting • Abdominal pain	• Discoloration of urine (doses over 80µg) • Bladder irritation	• Anemia

In the human body, methylene blue is highly stable; if ingested, it resists the stomach's acidic environment as well as the hydrolytic enzymes present. Methylene blue has some other adverse effect in human body as it has been stated in the chart [79].

2.8.1.4 Dye Removal by Graphene-Inorganic Nanocomposites

Graphene based nanocomposites usually remove dye following two basic routes- adsorption and photocatalytic degradation. Adsorption is a process that occurs when a gas or liquid solute accumulates on the surface of a solid or a liquid, forming a molecular or atomic film. It is a surface phenomenon and a consequence of surface energy. The atoms on the surface of the adsorbent are not wholly surrounded by other atoms and thus, can attract adsorbates. The exact nature of the bonding depends on the details of the species involved, but the adsorption process is generally classified as follows:

(1) **Physisorption**: It is a type of adsorption in which the adsorbate adheres to the surface through Van der Walls (weak intermolecular) interactions.
(2) **Chemisorption**: It is a type of adsorption whereby a molecule adheres to a surface through the formation of a chemical bond.

Adsorption takes place primarily on the walls of the pores or at specific sites inside the particle. As the pores are generally small, the internal surface area is greater than the external area. Separation occurs because differences in molecular weight, shape or polarity cause some molecules to be held more strongly on the surface than others. In many cases, the adsorbate is held strongly enough to allow complete removal of that component from the fluid [80].

In recent years, semiconductor-mediated photocatalysis has attracted tremendous attention for its potential applications such as photocatalytic degradation of organic pollutants and photocatalytic hydrogen generation. In general, when a nanocomposite is illuminated with photons, which have energies greater than the band gap of the semiconductor, electrons in the valance band of the material are excited into the conduction band, resulting the generation of electron-hole pairs. These electron-hole pairs either recombine or migrate to the surface of photocatalyst to initiate a series of photocatalytic reactions and produce hydroxyl radicals, $^{\bullet}OH$ and superoxide radical, $^{\bullet}O_2^-$ in water, resulting the generation of hydrogen gas and degradation of organic pollutants. The drawback of the most of the photocatalysts is the rapid electron-hole recombination within photocatalysts, which decreases the efficiency of its photocatalytic activity. It is

believed that graphene with excellent electrical conductivity and large specific surface area can be used as an electron acceptor and transfer channel for reducing the rate of electron-hole recombination, which increases the efficiency of photocatalytic activity. In addition, graphene can increase the adsorption of pollutants due to the non-covalent interaction between organic pollutants and the aromatic regions of graphene, and extend the light absorption range of photocatalysts [81].

2.9 Electrochemical Capacitor

Electrochemical energy storage technologies are under serious consideration to satisfy the increasing demand for energy and growing concerns about energy conservation and global warming. Research programs are being launched through various government, university, and commercial ventures to develop the chemistries and technologies that will improve the generation and distribution of energy. Electrochemical capacitor are an important part of this endeavour.

2.9.1 Origin of Electrochemical Capacitance

2.9.1.1 Electrochemical Double-Layer Capacitance

A double layer appears on any surface of an electrode whenever it is placed in a solution. Let's consider a metal/solution interface. When the metal is under potentiostatic control (under q_M) there will be either an excess (q_M is negative) or a deficit of free electrons (q_M is positive) at the surface of the metal. A number of processes can occur at the electrode/electrolyte interface including contact adsorption and double layer formation. Solvated anions such as chloride, hydroxide, or cyanide can directly adsorb on metal electrodes due to chemical interaction between the host and these ions. During this process these ions lose part of their solvation sheath in the aqueous media which facilitates a metal-ion bond on the surface of the electrode. This process is referred to as "contact" adsorption. The region which contains these contact adsorbed ions is known as the Inner Helmholtz Layer (IHL). In addition to this, the excess charges on the metal can attract other particles in the solution such as dipole to preferentially orient in the vicinity of the metal solution interface and form a layer. This formed layer of solvated ions is the so called Outer Helmholtz Layer (OHL). The charge densities on the electrode and in the OHL are assumed to be equal and opposite in sign. Figure depicts these two layers and the variation of potential from the electrode surface. Therefore, the interface can be approximated by a double-layer, one layer being the OHL and the second one on the

electrode surface (the IHL) [82].

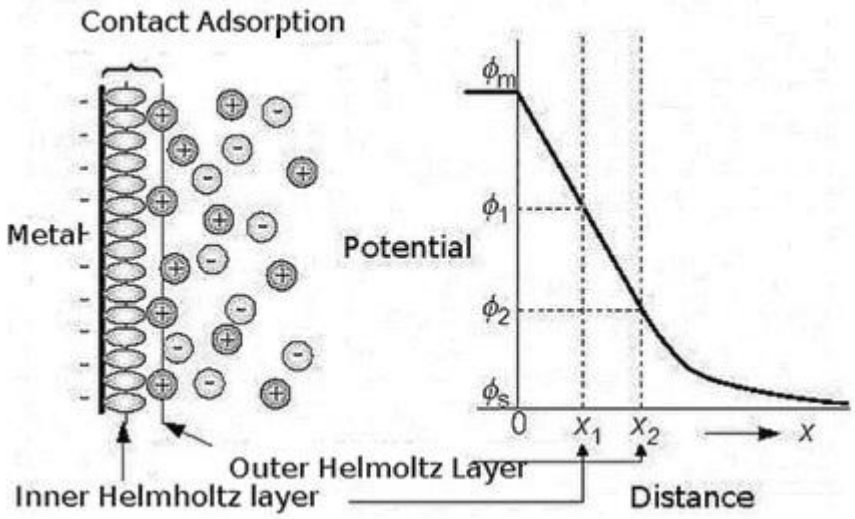

Fig. 2.11- Visual representation of a metal/solution interface in a solution and the potential profile of the electrified interface measured from the metal electrode surface

There are different models to explain the structure and potential variation of electrochemical double layer e.g. Helmholtz model [82], Gouy-Chapman Model [83], Stern Model [84].

2.9.1.2 Pseudo-Capacitance

Pseudo-capacitance involves a completely different charge storage mechanism which is faradaic in nature and requires charge transfer across the electrode/electrolyte interface. The faradaic process involves two types of reaction. One is the redox reaction which occurs in the metal oxide or conducting polymer electrodes, the other is the adsorption of ions on the electrode surface from the electrolyte. This capacitance behaviour was first noted by Buzzanca and Tarasatti in the cyclic voltammetry behavior of RuO_2 electrodes and followed by the studies of Conway *et al*., under potential deposition of hydrogen ad-atom [85-86].

Faradaic pseudocapacitance only occurs together with static double-layer capacitance. Pseudocapacitance and double-layer capacitance both contribute inseparable to the total capacitance value.

There are certain differences among the two type of capacitance. Some of the basic differences between double layer capacitance and pseudo-capacitance has been presented in the following table-

Table 2.2-Comparison of double-layer and pseudo-capacitance properties [86]

Double-Layer Capacitance	Pseudo-Capacitance
x Involves non-faradaic process	x Involves faradaic process
x Capacitance has the value of 20 to 50 μF/cm^2	x Capacitance has the value of 2000 μF/cm^2
x Capacitance is fairly constant with potential	x Capacitance is not constant with potential
x Highly reversible nature of charging and discharging	x Quasi–reversible nature of charging and discharging

2.9.2 Classification of Electrochemical Capacitors

Electrochemical capacitors can be classified as to the processes involved in the capacitor-

1) Electrochemical Double-layer Capacitor (EDLC)
2) Pseudo-capacitor
3) Hybrid Capacitor

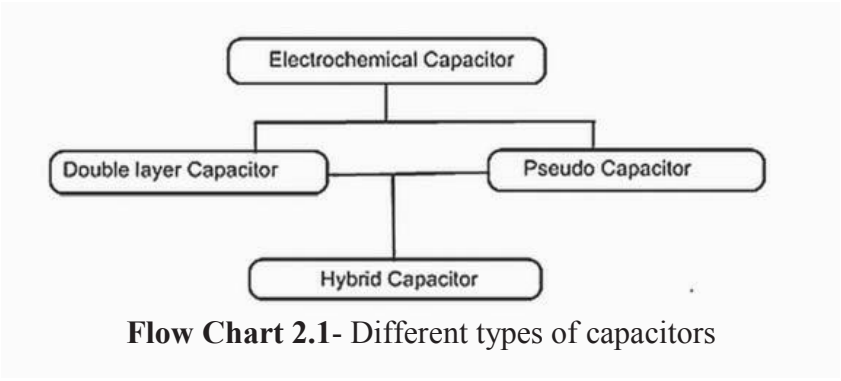

Flow Chart 2.1- Different types of capacitors

EDLC's employs high surface area carbons, carbon aerogels, carbon fibers and carbon nanotubes. The pseudo-capacitor utilizes the metal oxides such as RuO_2, NiO and MnO_2. Hybrid capacitors make use of high surface area carbon electrodes in combination either with battery type redox electrodes such as nickel hydroxide and lithium electrodes or pseudo-capacitor type electrodes.

2.10 Oxides of Manganese

Manganese (Mn)**,** chemical element, one of the silvery white, hard, brittle metals of Group 7 (VIIb) of the periodic table. It was recognized as an element in 1774 by the Swedish chemist Carl Wilhelm Scheele and was isolated the same year by his

associate, Johan Gottlieb Gahn. Manganese (Mn) is the 10th most abundant element in the earth's crust and second only to iron as the most common heavy metal; on average crustal rocks contain about 0.1% Mn. It occurs in natural systems mainly in three different oxidation states: +2, +3, and +4, giving rise to a range of multivalent phases. The most available oxides of manganese are MnO, Mn_3O_4, Mn_2O_3, MnO_2 and Mn_5O_8. The structural properties of these oxides are listed in table-

Table 2.3- Structural properties of different oxides of manganese

Oxide	**MnO**	**Mn_3O_4**	**Mn_2O_3**	**Mn_5O_8**	**MnO_2**
Mineral Name	Manganosite	Hausmannite	Bixbyte	n/a	Pyrolusite
Oxidation Number	+2	+2, +3	+3	+2, +4	+4
Crystal Structure	Cubic	Tetragonal	Cubic	Monoclinic	Tetragonal
Lattice Parameter	a = 4.44 Å	a = 5.76 Å c = 9.46 Å	a = 9.40 Å	a = 10.39 Å b = 5.73 Å c = 4.86 Å	a = 4.39 Å c = 2.87 Å

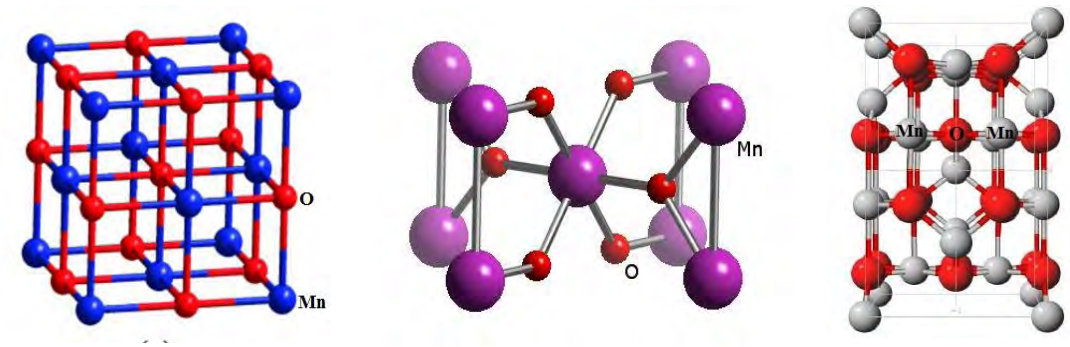

Fig. 2.12- Crystal structure of MnO (left), MnO_2 (middle) and Mn_3O_4 (right)

2.11 Oxides of Tin

Tin (Sn), a chemical element belonging to the carbon family, Group 14 (IVa) of the periodic table. It is a soft, silvery white metal with a bluish tinge, known to the ancients in bronze, an alloy with copper. It is usually obtained in two different oxidation state +2 and +4 as SnO and SnO_2. The structural properties of these oxides are listed in table-

Table 2.4- Structural properties of different oxides of tin

Oxide	**SnO**	**SnO_2**
Mineral Name	Romarchite	Cassiterite
Oxidation Number	+2	+4
Crystal Structure	Tetragonal	Rutile tetragonal
Lattice Parameter	a = 3.80 Å	a = 4.737 Å, c = 3.186 Å

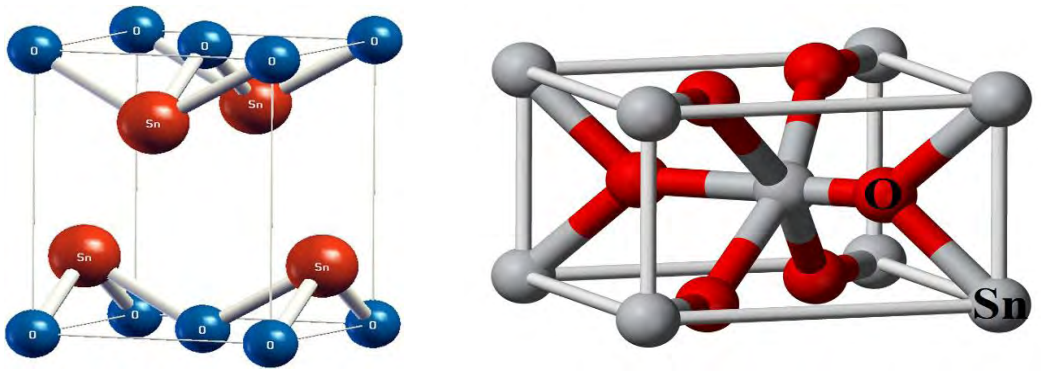

Fig. 2.13- Crystal structure of SnO (left) and SnO_2 (right)

References

1. Katsnelson, M. I., "Graphene: carbon in two dimensions", *Mater. Today*, vol. 20, pp. 20-27, 2007.
2. Geim, A. K., "Graphene: status and prospects", *Science*, vol. 324, pp. 1530-1534, 2004.
3. Bohem, H. Setton, R. and Stumpp, E., "Nomenclature and terminology of graphite intercalation compounds", *Pure & Appl. Chem.,* vol. 66(9), pp. 1893-1901, 1994.
4. Efremova, L. V., Vasilchenko, A. S., Rakov, E. G. and Deryabin, D. G., "Toxicity of graphene shells, graphene oxide, and graphene oxide paper evaluated with *Escherichia coli* biotests", *BioMed Res. Inter.*, vol. 2015(869361), pp. 1-10, 2015.
5. Dresselhaus, M. S. and Araujo, P. T., "Perspectives on the 2010 nobel prize in physics for graphene", *ACS Nano*, vol. 4(11), pp. 6297-6302, 2010.
6. Geim, A. K. and Novoselov, K. S., "The rise of graphene", *Nat. Mater.*, vol. 6, pp. 183-191, 2007.
7. Allen, M. J., Tung, V. C. and Kaner, R. B., "Honeycomb carbon: a review of graphene", *Chem. Rev.,* vol. 110, pp. 132–145, 2010.
8. Novoselov, K. S., Geim, A. K., Morozov, S. V., Jiang, D., Zhang, Y., Dubonos, S. V., Grigorieva, I. V. and Firsov, A. A., "Electric field effect in atomically thin carbon films", *Science,* vol. 306, pp. 666-669, 2004.
9. Du, X., Skachko, I., Barker, A. and Andrei, E. Y., "Approaching ballistic transport in suspended graphene", *Nat. Nanotechnol.,* vol. 3, pp. 491-495, 2008.
10. Nagashio, K., Nishimura, T., Kita, K. and Toriumi, A., "Mobility variations in mono- and multi-layer graphene films", *Appl. Phys. Express*, vol. 2, pp. 1-3, 2009.
11. Balandin, A. A, Ghosh, S., Bao, W., Calizo, I., Teweldebrhan, D., Miao, F. and Lau, C. N., "Superior thermal conductivity of single-layer graphene", *Nano Lett.,* vol. 8, pp. 902-907, 2008.
12. Nair, R. R., Blake, P., Grigorenko, A. N., Novoseolov, K. S., Booth, T. J., Stauber, T., Peres, N. M. R., and Geim, A. K., "Fine structure constant defines visual transparency of graphene", *Science,* vol. 320, pp. 1308- 1309, 2008.
13. Lee, C., Wei, X., Kyser, J. W., and Hone, J., "Measurement of the elastic properties and intrinsic strength of monolayer graphene", *Science,* vol. 321, pp. 385-388, 2008.
14. Rao, C. N. R., Sood, A. K., Subrahmanyam, K., S., and Govindaraj, A., "Graphene: the new two-dimensional nanomaterial", *Angew. Chem. Int. Ed.,* vol. 48, pp. 7752-

7777, 2009.

15. Van, B. A. J., Crombeen, J. E. and Van, A., "LEED and auger electron observations of the SiC (001) surface", *Surf. Sci.*, vol. 48, pp. 463-472, 1975.
16. Juang, Z., Wu, C., Lo, C., Chen, W., Huang, C., Hwang, J., Chen, F., Leou, K., Tsai, C., "Synthesis of graphene on silicon carbide substrates at low temperature", *Carbon,* vol. 47, pp. 2026-2031, 2009.
17. Emtsev, K. V., Bostwick, A., Horn, K., Jobst, J., Kellogg, G. L., Ley, L., Mcchesney, J. L., Ohta, T., Reshanov, S. A., Rohrl., J., Rotenberg, E., Schmid, A. K., Waldmann, D., Weber, H. B. and Seyller, T., "Towards wafer-size graphene layers by atmospheric pressure graphitization of silicon carbide", *Nat. Mater.,* vol. 8, pp. 203-207, 2009.
18. Kim, K. S., Zhao, Y., Jang, H., Lee, S. Y., Kim, J. M., Kim, K. S., Ahn, J., Kim, P., Choi, J. and Hong, B. H., "Large-scale pattern growth of graphene films for stretchable transparent electrodes", *Nature,* vol. 457, pp.706-710, 2009.
19. Blake, P., Brimicombe, P. D., Nair, R. R., Booth, T. J., Jiang, D., Schedin, F., Ponomarenko, L. A., Morozov, S. V., Gleeson., H. F., Hill, E. W., Geim, A. K. and Novoselov, K. S., "Graphene-based liquid crystal device", *Nano Lett.,* vol. 8, pp.1704-1708, 2008.
20. Bae, S., Kim, H., Lee, Y., Xu, X., Park, J., Zheng, Y., Balakrishnan, J., Lei, T., Kim, H. R., Song, Y. I., Kim, Y. J., Kim, K. S., Ozyilmaz, B., Ahn, J., Hong, B. H. and Jima, S., "Roll-to-roll production of 30-inch graphene films for transparent electrodes", *Nat. Nano.,* vol. 5, pp. 574-578, 2010.
21. Shelton, J. C., Patil, H. R. and Blakely, J. M., "Equilibrium segregation of carbon to a nickel (111) surface: a surface phase transition", *Surf. Sci.,* vol. 43, pp. 433-520, 1974.
22. Kaiser, A. B., "Electronic transport properties of conducting polymers and carbon nanotubes", *Rep. Prog. Phys.,* vol. 64(1), pp. 1-49, 2001.
23. Kopelevich, Y. and Esquinazi, P., "Graphene physics in graphite", *Adv. Mater.,* vol. 19, pp. 4559-4563, 2007.
24. Schniepp, H. C., Li, J., Mcallister, M. J., Sai, H., Herrera, A., Adamson, D. H., Prudhomme, R. K., Car, R., Saville, D. A. and Aksay, I. A., "Functionalized single graphene sheets derived from splitting graphite oxide", *J. Phys. Chem. B,* vol. 110, pp. 8535-8539, 2006.
25. Mcallister, M. J., Li, J., Adamson, D. H., Car, R., Schniepp, H. C., Abdala, A. A.,

Liu, J., Herrera, M., Milius, D. L., Car, R., Prudhomme, R. K. and Aksay, I. A., "Single sheet functionalized graphene by oxidation and thermal expansion of graphite", *Chem. Mater.,* vol. 19, pp. 4396-4404, 2007.

26. Kudin, K. N., Ozbas, B., Schnieep, H. C., Prudhomme, R. K., Aksay, I. A. and Car, R., "Raman spectra of graphite oxide and functionalized graphene sheets", *Nano Lett.,* vol. 8, pp. 36-41, 2007.
27. Cuong, T. V., Pham, V. H., Chung, J. S., Shin, E. W., Hahn, S. H., Huh, J. S., Rue, G. H., Kim, E. J., Hur, S, H. and Kohl, P. A., ". Solution-processed ZnO-chemically converted graphene gas sensor", *Mater. Lett.,* vol. 64, pp. 2479-2482, 2010.
28. Stankovich, S., Piner, R. D., Chen, X., Wu, N., Nguyen, S. T. and Ruoff, R. S., "Stable aqueous dispersions of graphitic nanoplatelets via the reduction of exfoliated graphite oxide in the presence of poly (sodium 4-styrenesulfonate)", *J. Mater. Chem.,* vol. 16, pp. 155-158, 2006.
29. Stankovich, S., Dikin, D. A., Piner, R. D., Kohlhass, K., Jia, Y., Wu, Y., Nguyen, S. T. and Ruoff, R. S., "Synthesis of graphene-based nanosheets via chemical reduction of exfoliated graphite oxide", *Carbon,* vol. 45, pp. 1558-1565, 2007.
30. Li, D., Muller, M. B., Gilje, S., Kaner, R. B. and Wallace, G. G., "Processable aqueous dispersions of graphene nanosheets", *Nat. Nano,* vol. 3, pp. 101-105, 2008.
31. Bourlinos, A. B., Gournis, D., Petridis, D., Szabo, A. and Dekany, I., "Graphite Oxide: Chemical reduction to graphite and surface modification with primary aliphatic amines and amino acids", *Langmuir,* vol. 19, pp. 6050-6055, 2003.
32. Pei, S., Zhao, J., Ren, W. and Cheng, H., "Direct reduction of graphene oxide films into highly conductive and flexible graphene films by hydrohalic acids", *Carbon,* vol. 48, pp. 4466-4474, 2010.
33. Guo, H., Wang, X., Qian, Q., Wang, F. and XIA, X., "A green approach to the synthesis of graphene nanosheets", *ACS Nano,* vol. 3, pp. 2653-2659, 2009.
34. Ramesha, G. K. and Sampath, S., "Electrochemical reduction of oriented graphene oxide films: an in situ raman spectroelectrochemical study", *J. Phys. Chem. C,* vol. 113, pp. 7985-7989, 2009.
35. An, S. J., Zhu, Y., Lee, S. H., Stoller, M. D., Emilsson, T., Park, S., Velamakanni, A., An, J. and Ruoff, R. S., "Thin film fabrication and simultaneous anodic reduction of deposited graphene oxide platelets by electrophoretic deposition", *J. Phys. Chem. Lett.,* vol. 1, pp. 1259-1263, 2010.
36. Brodie, B. C., "On the atomic weight of graphite", *Phil. Trans. Royal Soc. London,*

vol. 149, pp. 249-259, 1859.

37. Staudenmaier, L., "Verfahren zur darstellung der graphitsäure", *Berichte der deutschen chemischen Gesellschaft,* vol. 31, pp. 1481-1487, 1898.
38. Hummers, W. S. and Offeman, R. E., "Preparation of graphitic oxide", *J. Am. Chem. Soc.,* vol. 80, pp. 1339-1339, 1958.
39. Marcano, D. C., Kosynkin, D. V., Berlin, J. M., Sinitskii, A., Sun., Z., Slesarev, A., Alemany, L. B., Lu, W. and Tour, J. M., "Improved synthesis of graphene oxide", *ACS Nano,* vol. 4, pp. 4806-4814, 2010.
40. Lerf, A., He, H., Forster, M. and Klinowski, J., "Structure of graphite oxide revisited", *J. phys. Chem. B,* vol. 102, pp. 4477-4482, 1998.
41. Gao, W., Alemany, L. B., Ci, L. and Ajayan, P. M., "New insights into the structure and reduction of graphite oxide", *Nat. Chem.*, vol. 1, pp. 403-408, 2009.
42. Gomez, C., Weitz, R. T., Bittner, A. M., Scolari, M., Mews, A., Burghard, M. and Kern, K., "Electronic transport properties of individual chemically reduced graphene oxide sheets", *Nano Lett.,* vol. 7, pp. 3499-3503, 2007.
43. Roy, R., Roy, R. A. and Roy, D. M., "Alternative perspectives on "quasi-crystallinity: non-uniformity and nanocomposites", *Mater. Lett.*, vol. 4, pp. 323-328, 1986.
44. Schmidt, D., Shah, D. and Giannelis, E. P., "New advances in polymer/layered silicate nanocomposites", *Curr. Opin. Solid State*, vol. 6(3), pp. 205-212, 2002.
45. Gleiter, H., "Materials with ultrafine microstructures: retrospectives and perspectives", *Nano, Mater,*, vol. 1(1), pp. 1-19, 1992.
46. Stankovich, S., Dikin, D. A., Dommett, G. H. B., Kohlhaas, K. M., Zimney, E. J., Stach, E. A., Piner, R. D., Nguyen, S. T. and Ruoff, R. S., "Graphene-based composite materials", *Nature*, vol. 442, pp. 282-286, 2006.
47. Bai, S. and Shen, X., "Graphene-inorganic nanocomposites", *RSC Adv*., vol.2, pp. 64-98, 2012.
48. Cheng, Q., Tang, J., Ma, J., Zhang, H., Shinya, N. and Qin, L., "Graphene and nanostructured MnO_2 composite electrodes for supercapacitors", *Carbon,* vol. 49, pp. 2917-2925, 2011.
49. Huang, X., Zhou, X., Zhou, L., Qian, K., Wang, Y., Liu, Z. and Yu, C., "A facile one-step solvothermal synthesis of SnO_2/graphene nanocomposite and its application as an anode material for lithium-ion batteries", *ChemPhysChem*, vol. 12, pp. 278-281, 2011.
50. Luo, Q., Yu, X., Lei, B., Chen, H., Kuang, D. B. and Su, C., "Reduced graphene

oxide-hierarchical ZnO hollow sphere composites with enhanced photocurrent and photocatalytic activity", *J. Phys. Chem. C,* vol. 116, pp. 8111-8117, 2012.

51. Guo, J., Zhu, S., Chen, Z., Li., Y., Yu, Z., Liu, Q., Li, J., Feng, C. and Zhang, D., "Sonochemical synthesis of TiO_2 nanoparticles on graphene for use as photocatalyst", *Ultrason. Sonochem.,* vol. 18, pp. 1082-1090, 2011.
52. Wang, J., Zhong, C., Wexler, D., Idris, N. H., Wang, Z., Chen, L. and Liu, H., "Graphene-encapsulated Fe_3O_4 nanoparticles with 3d laminated structure as superior anode in lithium ion batteries", *Chem. Eur. J.,* vol. 17, pp. 661-667, 2011.
53. Xia, X., Tu, J., Mai, Y., Chen, R., Wang, X., Gu, C. and Zhao, X., "Graphene sheet/porous NiO hybrid film for supercapacitor applications", *Chem. Eur. J.,* vol. 17, pp. 10898-10905, 2011.
54. Cao, A., Liu, Z., Chu, S., Wu, M., Ye, Z., Cai, Z., Chang, Y., Wang, S., Gong, Q. and Liu, Y., "A facile one-step method to produce graphene–CdS quantum dot nanocomposites as promising optoelectronic materials", *Adv. Mater.,* vol. 22, pp. 103-106, 2010.
55. Wang, P., Jiang, T., Zhu, C., Zhai, Y., Wang, D. and Dong, S., "One-step, solvothermal synthesis of graphene-CdS and graphene-ZnS quantum dot nanocomposites and their interesting photovoltaic properties", *Nano Res.,* vol. 3, pp. 794-799, 2010.
56. Zhang, D., Gan, L., Wang, Q., Qi, L. and Guo, X., "Understanding charge transfer at PbS-decorated graphene surfaces toward a tunable photosensor", *Adv. Mater.,* vol. 24, pp. 2715-2720, 2012.
57. Wang, K., Liu, Q., Wu, X., Guan. Q. and Li, H., "Graphene enhanced electrochemiluminescence of CdS nanocrystal for H_2O_2 sensing", *Talanta,* vol. 82, pp. 372-376, 2010.
58. Chen, S., Zhu, J., Huang, H., Zeng, G., Nie, F. and Wang, X., "Facile solvothermal synthesis of graphene–MnOOH nanocomposites", *J. Solid State Chem.,* vol. 183, pp. 2552-2557, 2010.
59. He, Y., Bai, D., Yang, X., Chen, J., Liao, X. and Ma, Z., "A $Co(OH)_2$−graphene nanosheets composite as a high performance anode material for rechargeable lithium batteries", *Electrochem. Commun.,* vol. 12, pp. 570-573, 2010.
60. Wang, H., Robinson, J. T., Diankov, G. and Dai, H., "Nanocrystal growth on graphene with various degrees of oxidation", *J. Am. Chem. Soc.,* vol. 132, pp. 3270-3271, 2010.

61. He, F., Fan, J., Ma, D., Zhang, L., Leung, C. and Chan, H., "The attachment of Fe_3O_4 nanoparticles to graphene oxide by covalent bonding", *Carbon,* vol. 48, pp. 3139-3144, 2010.
62. Zhang, Y., Chen, B., Zhang, L., Huang, J., Chen, F., Yang, Z., Yao, J. and Zhang, Z., "Controlled assembly of Fe_3O_4 magnetic nanoparticles on graphene oxide", *Nanoscale,* vol. 3, pp. 1446-1450, 2011.
63. Huang, J., Zhang, L., Chen, B., Ji, N., Chen, F., Zhang, Y. and Zhang, Z., "Nanocomposites of size-controlled gold nanoparticle and graphene oxide: formation and applications in SERS and catalysis", *Nanoscale,* vol. 2, pp. 2733-2738, 2010.
64. Zhu, G., Liu, Y., Xu, Z., Jiang, T., Zhang, C., Li., X. and Qi, G., "Flexible magnetic nanoparticles–reduced graphene oxide composite membranes formed by self-assembly in solution", *ChemPhysChem,* vol. 11, pp. 2432-2437, 2010.
65. Li, J. and Liu, C., "Ag/graphene heterostructures: synthesis, characterization and optical properties", *Eur. J. Inorg. Chem.,* vol. 2010, pp. 1244-1248, 2010.
66. Zou, W., Zhu, J., Sun, Y. and Wang, X., "Depositing ZnO nanoparticles onto graphene in a polyol system", *Mater. Chem. Phys.,* vol. 125, pp. 617-620, 2011.
67. Huang, X., Zhou, X., Wang, Y., Liu, Z. and Yu, C., "A facile one-step solvothermal synthesis of SnO_2/graphene nanocomposite and its application as an anode material for lithium-ion batteries", *ChemPhysChem,* vol. 12, pp. 278-281, 2011.
68. Zhou. Y., Bao, Q., Tang, L. A. L., Zhong, Y. and Looh, K. P., "Hydrothermal dehydration for the 'green' reduction of exfoliated graphene oxide to graphene and demonstration of tunable optical limiting properties", *Chem. Mater.,* vol. 21, pp. 2950-2956, 2009.
69. Du, M., Yang, T. and Jiao, K., "Immobilization-free direct electrochemical detection for DNA specific sequences based on electrochemically converted gold nanoparticles/graphene composite film", *J. Mater. Chem.,* vol. 20, pp. 9253-9260, 2010.
70. Hu, Y., Jin, J., Wu, P., Zhang, H. Cai, C., "Graphene–gold nanostructure composites fabricated by electrodeposition and their electrocatalytic activity toward the oxygen reduction and glucose oxidation", *Electrochim. Acta,* vol. 56, pp. 491-500, 2010.
71. Bang, J. H. and Suslick, K. S., "Applications of ultrasound to the synthesis of nanostructured materials", *Adv. Mater.,* vol. 22, pp. 1039-1059, 2010.
72. Khorshed, Z. A., Majid, W. H. A., Wang., H, Z., Yousefi, R., Moradi, G. A. and Ren., Z. F., "Sonochemical synthesis of hierarchical ZnO nanostructures", *Ultrason.*

Sonochem., vol. 20, pp. 395-400, 2013.

73. Caruso, R. A., Ashok, K. M. and Grieser, F., "Sonochemical formation of gold sols", *Langmuir*, vol. 18, pp. 7831-7836, 2002.
74. Yagub, M. T., Sen, T. K., Afroze, S. and Ang, H. M., "Dye and its removal from aqueous solution by adsorption: a review", *Adv. Colloid Interface Sci.,* vol. 209, pp. 172–184, 2014.
75. Lomax, S. Q., Learner, T., "A review of the classes, structures, and methods of analysis of synthetic organic pigments", *JAIC*, vol. 45, pp. 107-125, 2006.
76. Shahid, M., Islam, M. and Mohammad, F., "Recent advancements in natural dye applications: a review", *J. Clean. Prod.*, vol. 53, pp. 310-331, 2013.
77. Forgacs, E., Cserhati, T. and Oros, G., "Removal of synthetic dyes from wastewaters: a review", *Environ. Inter.*, vol. 30, pp. 953-971, 2004.
78. Schirmera, R. H., Adlera, H., Pickhard, M. and Mandelkowb, E., "Lest we forget you — methylene blue", *Nurobiol. Aging*, vol. 32(12), pp. 7–16, 2011.
79. Mokhlesi, B., Leikin, J. B., Murray, P. and Corbridge, T. C., "Adult toxicology in critical care part II: specific poisonings", *Chest*, vol. 123 (3), pp. 897-922, 2003.
80. Chang, H. and Wu, H., "Graphene-based nanocomposites: preparation, functionalization and energy and environmental applications", *Energy Environ. Sci*., vol. 6, pp. 3483–3507, 2013.
81. Zhang, H., Lv, X., Li, Y., Wang, Y. and Li. J., "P25-graphene composite as a high performance photocatalyst", *ACS Nano,* vol. 4, pp. 380-386, 2009.
82. Helmholtz, "Theory of electrical double layer", *Wied. Ann.,* vol. *7*, pp. 337-340, 1879.
83. Gouy, G., "Constitution of the electric charge at the surface of an electrolyte", *J. phys*, vol. *9* (4), pp. 457-467, 1910.
84. Stern, O., "The theory of the electric double layer", *Z. Electrochem*., vol. 30, pp. 508-513, 1924.
85. Pell, W. G., Conway, B. E., "Double-layer and pseudo-capacitance types of electrochemical capacitors and their applications to the development of hybrid devices", *J. Solid State Electrochem.,* vol. 7(9), pp. 637-644, 2003.
86. Conway, B., Birss, V., Wojtowicz, J., "The role and utilization of pseudo-capacitance for energy storage by supercapacitors", *J. Power Sources*, vol. 66 (1-2), pp. 1-14, 1997.

Chapter 3

Characterization Techniques

3.1 Fourier Transform Infrared spectroscopy (FTIR)

FTIR is one of the most common and widely used spectroscopic techniques employed mainly by chemists due to its usefulness in determining structures of compounds and identifying them. It is based upon characteristic absorption of infrared radiation (IR) of molecules. The fundamental measurement obtained in FTIR is an infrared spectrum, which is a plot of measured intensity versus wavenumber of IR for a solid, liquid or gas sample.

IR involves the energy region of electromagnetic radiation (EMR) corresponding to wavenumber of 14000 ~ 4 cm^{-1}. It can be divided into near-infrared region (14000 ~ 4000 cm^{-1}), mid-infrared region (4000 ~ 400 cm^{-1}) and far-infrared region (400 ~ 4 cm^{-1}). The commonly used region for FTIR is 4000 ~ 400 cm^{-1} because the absorption radiation of most functional groups and bonds in organic and inorganic materials is within this region. Only the molecules which have a dipole moment that changes as a function of time are able to interact with IR and thus called IR active. Molecules with different structure even with same bond at different chemical environment vibrate at different frequencies and thus make it enable to distinguish them from FTIR. FTIR of a sample may be affected by various structural parameters. Structural factor include nature of the bonds (single/double/triple), mass of the atoms constituting bond, nature of hybridization, mode of vibration, resonance, type of isotope, solvent etc [1].

The most common method of sample preparation for IR involves mixing the finely ground solid sample with powdered KBr and pressing the mixture under high pressure. Under pressure KBr melts and seals the compound into a matrix. The result is a KBr pellet which can be inserted into a holder into the spectrometer. This method is known as mull technique.

FTIR is advantageous from several perspective. e.g. High scan speed, high resolution, high sensitivity, wide range of application, large amount of structural information, non destructiveness.

3.2 Field Emission Scanning Electron Microscopy (FESEM)

FESEM, a modern form of the scanning electron microscope (SEM), is a powerful technique in the examination of materials, revealing external morphology (texture), crystalline structure and orientation of materials making up the sample [2]. The term ‘SEM’ is substituted by ‘FESEM’ with the use of Field Emission GUN (FEG) instead of

Thermionic Emission Gun (TEG) as electron emitter gun. SEM uses a focused beam of high-energy electrons to generate a variety of signals at the surface of solid specimens.

Among the signals, secondary electrons and backscattered electrons are commonly used for imaging samples: secondary electrons are most valuable for showing morphology and topography on samples and backscattered electrons are most valuable for illustrating contrasts in composition in multiphase samples (i.e. for rapid phase discrimination).

In most applications, data are collected over a selected area of the surface of the sample, and a 2-dimensional black-white image is generated that displays spatial variations in these properties. Areas ranging from approximately 1 cm to 5 microns in width can be imaged in a scanning mode using conventional SEM techniques (magnification ranging from 20X to approximately 500000X, spatial resolution of 50 to 100 nm).

Advantages of SEM include its wide-array of applications, the detailed two-dimensional and topographical imaging and the versatile information garnered from different detectors. SEMs are also easy to operate with the proper training and advances in computer technology and associated software has made operation user-friendly.

3.3 Energy Dispersive X-ray Spectroscopy (EDX)

Energy Dispersive X-ray Spectroscopy (EDX), which is also called EDS, is a microanalysis technique used to identify the elemental composition and in chemical characterization of materials. EDX systems are commonly used in conjunction with Electron Microscopy instruments (Scanning Electron Microscopy (SEM) or Transmission Electron Microscopy (TEM)), where the imaging capability of the microscope identifies the specimen of interest [3].

When the sample is bombarded by the SEM's electron beam, electrons are ejected from the atoms comprising the sample's surface. The resulting electron vacancies are filled by electrons from a higher state, and an x-ray is emitted to balance the energy difference between the two electrons' states. The x-ray energy being characteristic of the element from which it was emitted, identity of elements and their relative abundance can be marked by detecting this x-ray radiation.

EDX offers the advantages of quick, ‘first look’ compositional analysis. When used in "spot" mode, a user can acquire a full elemental spectrum in only a few seconds. Supporting software makes it possible to readily identify peaks, which makes EDX a

great survey tool to quickly identify unknown phases prior to quantitative analysis. EDX can also be used in semi-quantitative mode to determine chemical composition by peak-height ratio relative to a standard.

3.4 X-Ray Diffraction Spectroscopy (XRD)

XRD is one of the most powerful, reliable, non-destructive technique for the qualitative and quantitative analysis of the crystalline materials, in form of powder or solid.

XRD is based on constructive interference of monochromatic X-rays and a crystalline sample. These X-rays are generated by a cathode ray tube, filtered to produce monochromatic radiation, collimated to concentrate, and directed toward the sample. The interaction of the incident rays with the sample produces constructive interference (and a diffracted ray) when conditions satisfy Bragg's Law. This law relates the wavelength of electromagnetic radiation to the diffraction angle and the lattice spacing in a crystalline sample [4].

These diffracted X-rays are then detected, processed and counted. By scanning the sample through a range of 2θ angles, all possible diffraction directions of the lattice are attained due to the random orientation of the powdered material. Conversion of the diffraction peaks to d-spacing allows identification of the mineral because each mineral has a set of unique d-spacing. Typically, this is achieved by comparison of d-spacing with standard reference patterns. The value of d-spacing is obtained from Bragg's law-

$$2d \sin\theta = n\lambda$$

Where, d is inter layer spacing, θ is the x-ray angle of incidence (and of diffraction) measured with respect to the crystalline planes, n is an integral value and λ is the wavelength of incident beam.

Crystallite size of crystals are calculated from Scherrer formulae-

$$D = \frac{k\lambda}{\beta \cos\theta}$$

Where, D is the crystallite size, k is a dimensionless shape factor (typical value 0.9), l is the x-ray wavelength, β is the line broadening at halfway of the maximum intensity (FWHM) and θ is the Bragg angle (in degrees).

Sample preparation is one of the most important steps in a successful XRD analysis. Typically, samples are grinded to achieve a good S/N ratio, avoid spottiness and minimize preferred orientation. The ideal samples are crystalline powders.

XRD offers many advantages over other available techniques in sample analysis. These includes powerful and rapid technique for identification of an unknown mineral, in most cases provide an unambiguous mineral determination, require small amount of sample preparation, data interpretation is relatively straight forward etc.

3.5 Thermogravimetric Analysis (TGA)

Thermogravimetric Analysis (TGA) is a thermal analysis technique used to learn about various possible physical and chemical phenomenon associated with a sample and their kinetics. In this operation, the mass of a substance is monitored as a function of temperature or time as the sample specimen is subjected to a controlled temperature program in a controlled atmosphere. TGA is used primarily to determine the composition of materials and to predict their thermal stability. It can characterize materials that exhibit weight loss or gain due to sorption/desorption of volatiles, decomposition, oxidation and reduction [5].

3.6 Ultraviolet-Visible (UV-Vis) Absorption Spectroscopy

UV-Vis absorption spectroscopy is a common tool in absorption / adsorption study particularly in dye removal. It is an absorption spectroscopy in the UV region of electromagnetic radiation (EMR). Owing to different electronic structure, molecules may absorb radiation at different wavelengths, with different intensity varying upon concentration and thus can be used to identify and calculate their concentration in a solution.

The absorption of UV or visible radiation corresponds to the excitation of outer electrons. There are three types of electronic transition among which transitions involving σ, π, and *n* electrons are more simple and easy to explain. Molecules containing π or non-bonding electrons can absorb UV-Vis light to result into various electronic excitations e.g. $\sigma - \sigma^*$, $\pi - \pi^*$, n-σ^*, n-π^* etc. With difference in band gap energy, different excitation requires different amount of energy leading to UV-Visible light absorption at different wavelength. Thus different compounds with difference in their electronic structure, rise to absorption of UV-Vis light at characteristic wavelength [6].

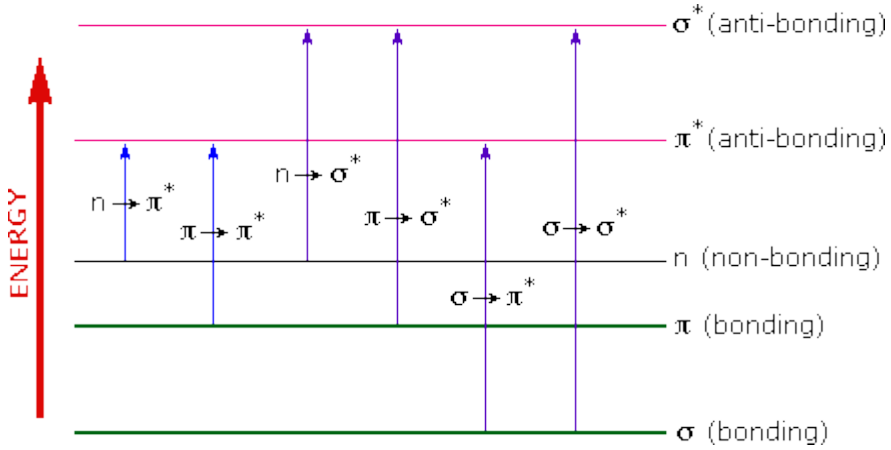

Fig. 3.1- Possible simple electronic excitations in a molecule

UV-Vis absorption spectroscopy obeys the Beer-Lambert law, which states that, when a beam of monochromatic light is passed through a solution of an absorbing substance, the rate of decrease of intensity of radiation with thickness of the absorbing solution is proportional to the incident radiation as well as the concentration of the solution.

The expression of Beer-Lambert law is-

$$A = \log \frac{I_0}{I} = \epsilon c l$$

Where, A is absorbance, I_0 = intensity of light incident upon sample cell, I = intensity of light leaving sample cell, ε is molar absorbance, c is concentration and l is length of sample cell (cm). As a result, difference in intensity of the spectrum can be correlated to the concentration of active sample.

In UV-Vis spectroscopy, a sample is usually dissolved in a solvent that is transparent to the UV-Vis region of interest. It is because otherwise, it will be difficult to distinguish between absorption peak from sample and solvent.

UV-Vis spectroscopy offers a mean of rapid analysis and can provide very high precission and accuracy. It is useful for a wide variety of chemicals, and it is non-destructive. It can be used both quantitatively and qualitatively on pure substances.

3.7 Cyclic Voltammetry (CV)

CV is an electro-analytical technique based on the current response of a material as a function of potential [7]. It is performed by cycling the potential of the working electrode while measuring the resulting current. It is the modern form of polarography, developed by Jaroslav Heyrovsky in 1922.

In the CV experiment, the potential of an immersed, stationary electrode is scanned from a predetermined starting potential to a final value (called the switching potential) and then the reverse scan is performed. This gives a 'cyclic' sweep of potentials which can be repeated as per interest and the current vs. potential curve derived from the data is called a cyclic voltammogram. The first sweep is called the 'forward scan' and the return wave is called the 'reverse scan'. The potential extremes are termed the 'scan window'.

When potential allowed to increase, initially current response is defined as capacitive, originating from electrical double layer (EDL) formed at electrode surface involving diffusion controlled process. When the potential approaches a specific value favoring the reduction of the active material, current response increases rapidly resulting an anodic peak and the corresponding current and potential are called anodic peak current and anodic potential. Then current falls off as the maximum rate of mass transfer has been reached and goes down only to reach equilibrium at some steady value. A similar but opposite peak current may be observed when potential meets a value favoring oxidation of the reduced species during its return tour to the initial value [18].

$$\mathbf{R} + \mathbf{e}^{-} \leftrightarrow \mathbf{O}$$

Current responses from redox reaction are termed as faradic current while the remaining responses are usually attributed to EDL and called non Faradic current. Thus, the capacitive window of a material can be easily identified from the absence or presence of redox peak in its CV [19].

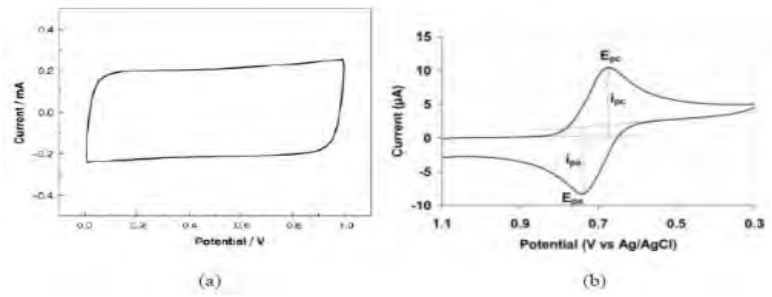

Fig. 3.2- Cyclic voltammogram of a material in different potential window (a) without and (b) with redox peak

One important feature of CV is that, the total current increases with increasing scan rate. The rate of change of potential with time is referred to as the scan rate. This can be rationalized by considering the size of the diffusion layer and the time taken to record the scan.

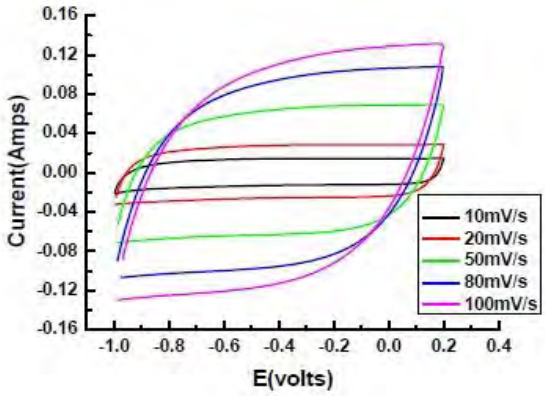

Fig. 3.3- Variation in current response of a material with different scan rates

The magnitude of current response and the shape of the voltammograms are highly dependent on analyte nature, concentration, scan rates, and experimental conditions. By varying these factors, cyclic voltammetry can yield information regarding dependency of the process, the stability of transition metal oxidation state in the complex form, reversibility of electron transfer reactions, reactivity of active material etc.

3.8 Chronopotentiometry (CP)

Chonopotentiometry (CP) is the most commonly used constant current experiment. It is an electro-analytical technique in which an unstirred solution of an electroactive species, in presence of excess of a supporting electrolyte, is electrolyzed at a programmed current density between an indicator electrode and a counter electrode and the potential-variation of the former vs. a suitable reference is recorded as a function of time [8]. The resulting graphs are current excitation signal and potential response as a function of time.

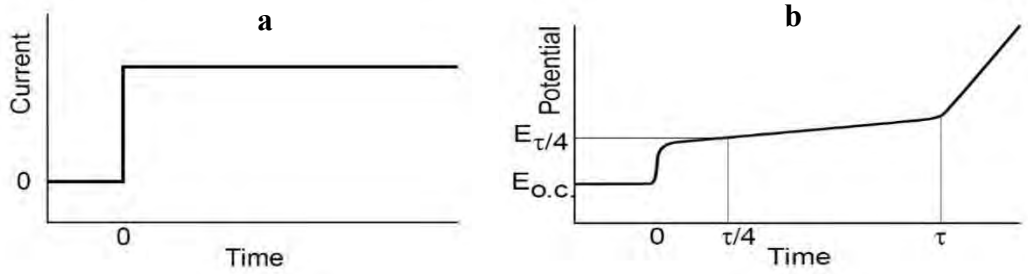

Fig. 3.4- Current excitation (a) and potential response (b) in CP

It is possible to identify the nature of electrode material from the CP. e.g. the potential response of an ideal capacitive material in CP shows discharge/ charge time to be ~ 1 and can be easily marked.

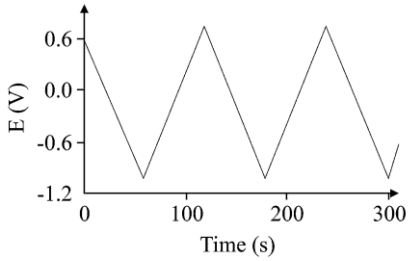

Fig. 3.5- Potential response of an ideal electrochemical capacitor in CP

The specific capacitance of an electrochemical capacitor can be easily calculated from its potential response in CP on the basis of the relationship-

$$C_{sp} = \frac{i\Delta t}{m\Delta V}$$

Where, C_{sp} is the specific capacitance, I is discharge current (cathodic current), m is the mass of active electrode material, Δt is the total time of discharge and ΔV is the potential drop during discharge.

3.9 Electrical Impedance Spectroscopy (EIS)

Electrical Impedance Spectroscopy (EIS) is a perturbative characterization of the dynamics of an electrochemical process [9]. It is a method of measuring the electrical impedance of a substance as a function of the frequency of an applied electrical current.

Electrical impedance (Z) is the total effect of resistance or the measure of the opposition to the passage of the current when an AC voltage source is applied. In simple circuit system, where DC voltage source is applied, resistance (R) is the only property of a material that oppose the flow of current. However, in real circuit systems, i.e. RLC circuit, resistance (R) is accompanied by reactance (X) from capacitor (C) and inductor (L), collectively known as impedance. Following Ohm's law V=IR, we can write in that case, V=IZ, where impedance Z use the same unit ohm, as used by resistance.

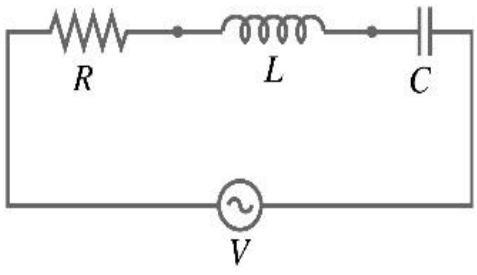

Fig. 3.6- A RLC series circuit

Impedance data are commonly represented in two forms. One as Nyquist plot, showing the variation of Z_{img} with Z_{real} and the other as Bode plot showing the frequency dependency of phase angle.

Electrochemical processes involves various types of resistance originating from solution, charge transfer, electrical double layer (capacitor), diffusion etc. and their equivalent circuit, commonly known as Randles circuit, can be drawn from EIS study.

A Randles circuit is an equivalent electrical circuit that consists of an active electrolyte resistance R_S in series with the parallel combination of the double-layer capacitance C_{dl} and an impedance of a faradaic reaction.

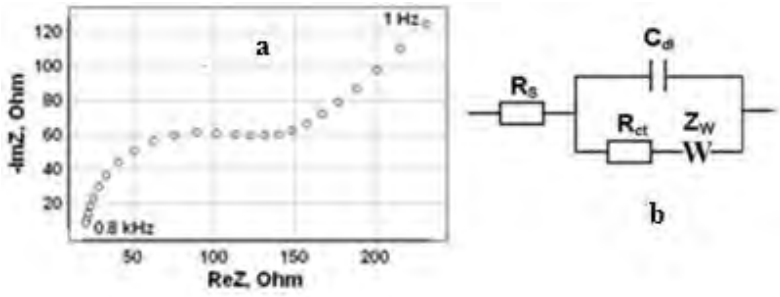

Fig. 3.7- (a) A typical Nyquist plot and (b) its equivalent circuit

EIS offers the chance of both diagnostic and application of electrochemical processes. With EIS, it is possible to identify the nature of an electroactive material. It has been applied in engineering, biosensor applications etc.

References

1. Pavia, D. L., Lampman, G. M. and Kriz, G. S. (2001) *Introduction to spectroscopy*. Thomson Learning Inc., Singapore.
2. Egerton, R. F. (2005) Physical principles of electron *microscopy.* Springer Science + Business Media, Inc., New York.
3. Reed, A. J., and Bell, D. C. (2003) *Energy-dispersive x-ray analysis in the electron microscope*. Bios Scientific Publishers Ltd., London.
4. Suryanarayana, C. and Norton, M. J. (1998) *X-ray diffraction - a practical approach*. Springer Science + Business Media, Inc., New York.
5. Prime, R. B., Bair, H. E., Vyazovkin, S., Gallegher, P. K. and Riga, A. (2009) *Thermal analysis of polymers: fundamentals and applications*. John Wiley & Sons, Inc., New York.
6. Grinter, H. C. and Threlfall, T. L. (1992) *UV-Vis spectroscopy and its applications.* Springer-Verlag Berlin Heidelberg, Berlin.
7. Wang, J. (2000) *Analytical electrochemistry*. John Wiley & Sons, Inc., New York.
8. Bard, A. J. and Faulkner, L. R., (1944) *Electrochemical methods: fundamentals and applications*. John Wiley & Sons, Inc., New York.
9. Barsoukov, E. and Macdonald, J, R. (2005) *Impedance spectroscopy*. John Wiley & Sons, Inc., New Jersey.

Chapter 4

Experimental

4.1 Materials and Instruments

4.1.1 Chemicals and Reagents

The chemicals and reagents used in this work were all of analytical grade and were used without further purification. The whole work along with the final parts of the washings was performed using de-ionized water (~ 0.66 μS / 1.51 MΩ). The chemicals and reagents used in this work are listed below:

(i) Graphite powder (Sigma-Aldrich, Switzerland)
(ii) Sodium nitrate (Merck, Germany)
(iii) Potassium permanganate (Merck, India)
(iv) Sulfuric acid (Merck, Germany)
(v) Hydrogen peroxide (Scharlau, Spain)
(vi) Hydrochloric acid (RCI Labscan, Thailand)
(vii) Manganese acetate (Merck, Germany)
(viii) 2-Propanol (Daejung, South Korea)
(ix) Stannous chloride (Scharlau, Spain)
(x) Methylene blue (Merck, Germany)
(xi) Polyvinyl alcohol (Merck, Germany)
(xii) Dimethyl sulphoxide (Lab-Scan, Ireland)
(xiii) Ethanol (Merck, Germany)

4.1.2 Instruments

Synthesis and analysis of the samples were performed using the following instruments:

(i) Digital balance (CX 220, Citizon, USA and GH-252, AND, Japan)
(ii) Hotplate with digital stirrer (CD 162, Stuart, UK)
(iii) Centrifuge machine (Universal 16A, Hettich, Germany)
(iv) Hot air oven (DSO-500D, Digisystem, Taiwan)
(v) Agate mortar (125mm)
(vi) Muffle furnace (LT 5/12, Nabertherm, Germany)
(vii) Inert atmosphere furnace (CWF-1300, Carbolite Gero, Germany)
(viii) pH meter (3510 pH meter, Jenway, UK)
(ix) Orbital shaker (SSL1, Stuart, UK)
(x) Ultrasonic bath (Powersonic 505, Hwashin, S. Korea)
(xi) Fourier Transform Infrared Spectrophotometer (FTIR-8400, Shimadzu, Japan)

(xii) Field emission scanning electron microscopy (JSM-7600F, JEOL, Japan)

(xiii) X-ray diffractometer (Ultima IV, Rigaku, Japan)

(xiv) Thermogravimetric analyzer (TGA-50H, Shimadzu, Japan)

(xv) UV-Visible spectrophotometer (UV-1800, Shimadzu, Japan)

(xvi) Electrochemical working station (760E, CH instruments, USA)

4.2 Synthesis of Materials

4.2.1 Synthesis of Graphene Oxide (GO) and reduced Graphene Oxide (rGO)

GO was prepared from graphite powder (< 20 μm) following the Hummers method. In detail, a mixture of graphite powder (1.0 g), $NaNO_3$ (0.5 g) and $KMnO_4$ (3.0 g) were slowly added to a concentrated H_2SO_4 solution (23 ml) within an ice bath. After removing the ice bath, the above mixture was intensely stirred at ~ 35 °C for 30 min. After the reaction was completed, deionized water (46 ml) was added to above mixture while keeping the temperature at ~ 98°C for 15 min, followed by reducing the temperature to ~ 60 °C with the addition of warm deionized water (140 ml) and H_2O_2 (30%, 10 ml) while stirring continuously for a further 2 h. The obtained mixture was filtrated to collect the solid product and washed with 4 wt% HCl solution several times and then with water until the solution was found to be free of chloride ion. The prepared solution of GO was preserved for further use. A portion of GO was dried in an oven at 60°C resulting to thin brown sheet for analysis purpose. rGO was prepared via thermal reduction by annealing dried GO at 400°C under N_2 inert atmosphere for 1.5h.

4.2.2 Synthesis of rGO/Mn-oxide/Sn-oxide Ternary Nanocomposite

The synthesis of rGO/Mn-oxide/Sn-oxide ternary nanocomposite was performed in several steps. The first step involved the synthesis of GO as described earlier.

The second step involved the growth of Mn-oxide nanoparticles on the functionalized surface of GO using water-isopropyl alcohol system. In brief, 10 mL of GO solution (~10 g/L) was introduced with 100 mL of 2-propanol (Isopropyl alcohol) along with 507.4 mg of $Mn(CH_3COO)_2.2H_2O$. The mixture was subjected to High power sonication for 30 minutes. Next, it was heated to 83°C with a fitted condenser while performing a vigorous stirring. Then, 218.1 mg of $KMnO_4$ dissolved in 10 mL water was added to the mixture while stirring continued. After 30 minutes of refluxing, the mixture was allowed to settle down and cooled to room temperature. The obtained product was washed gently with water replacing the water-Isopropyl alcohol system with D.I. water only.

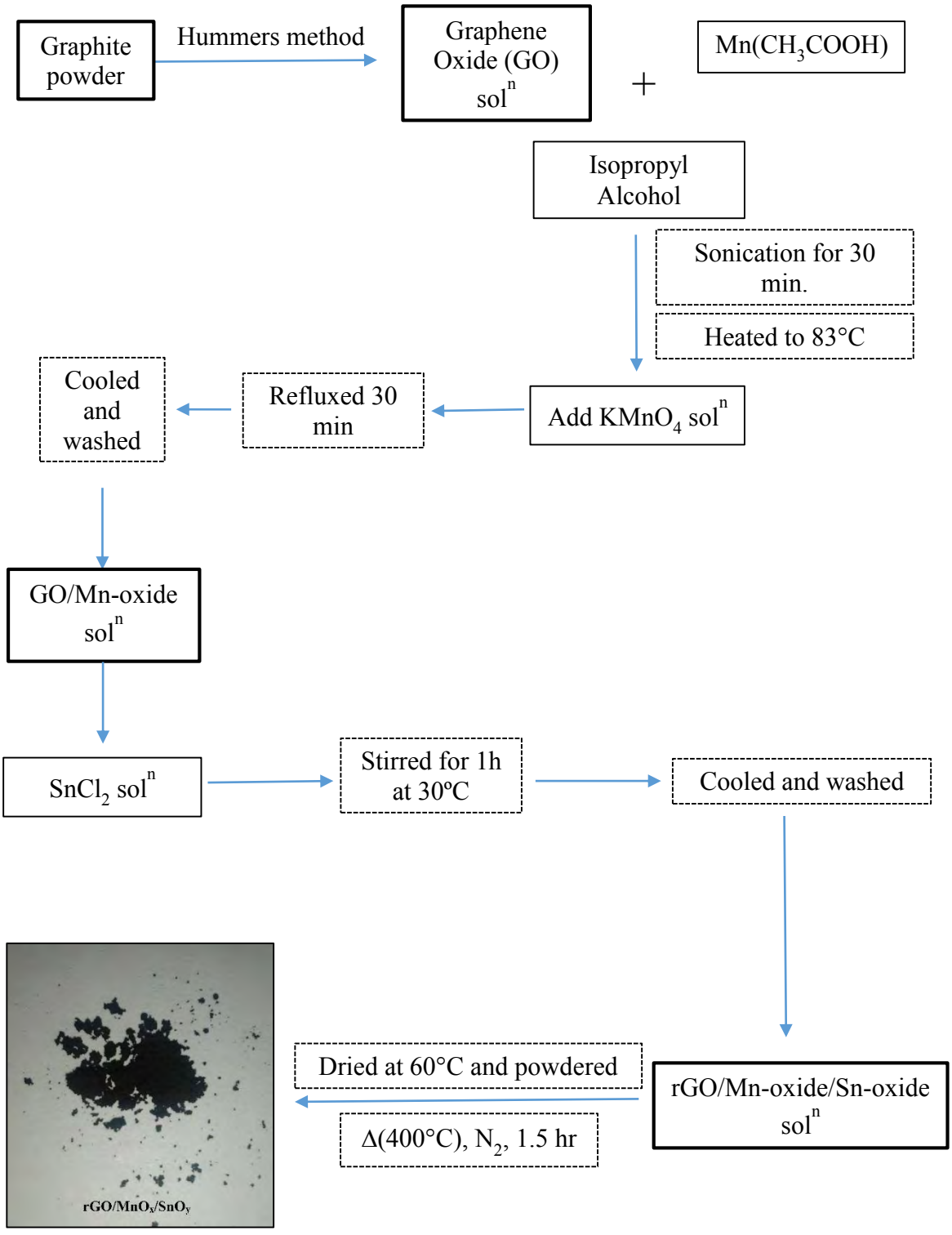

Flow Chart 4.1- Scheme of the synthesis of rGO/Mn-oxide/Sn-oxide ternary nanocomposite

The third step involved reducing the GO surface while harbouring SnO_2 nanoparticles. It began with the introduction of 250 mg of $SnCl_2.2H_2O$ into an adjusted volume of 500mL of the mixture, which was then subjected to stirring for 1h at ~ 30°C. Consequentially, the nanocomposite was washed with water, dried at 60°C and powdered with agate mortar.

The final product was obtained after annealing at 400°C under N_2 inert atmosphere for 1.5h to achieve a better crystallinity along with a better reduction of GO surface.

4.2.3 Synthesis of rGO/Mn-oxide and rGO/Sn-oxide Binary Nanocomposites

To understand the suitability of the ternary nanocomposite in the applications of interest, two corresponding binary nanocomposites namely rGO/Mn-oxide and rGO/Sn-oxide was also prepared. They were prepared exactly in the same way as it was employed for the ternary nanocomposite except omitting the third and the second step for the synthesis of rGO/Mn-oxide and rGO/Sn-oxide binary naocomposite respectively. Both of these nanocomposites were also annealed at 400°C under N_2 inert atmosphere for 1.5h.

4.3 Characterization

4.3.1 Fourier Transform Infrared Spectroscopy (FTIR) analysis

The FTIR spectra of the nanocomposites were recorded with an FTIR-8400, Shimadzu spectrophotometer in the mid-IR region (4000-400 cm^{-1}). In each case, about 125 mg of dry, pure KBr was mixed with ~ 1 mg dry sample, grinded homogenously with mortar-pestle and pressed mechanically under a pressure of 8-10 tons to make a pellet. Finally, the pallet was placed in the path of IR beam for measurement.

4.3.2 Field Emission Scanning Electron Microscope (FESEM) Analysis

The surface morphology of the samples were analyzed with Schottky Field Emission Scanning Electron Microscope (JSM-7600F, JEOL) via secondary electron imaging. After finely powdering, ~ 1-2 mg of the nanocomposite were dispersed on a conducting carbon glued strip. It was dried with air from hand pump. The sample loaded strip was then mounted to a chamber that evacuated to ~ 10^{-3} to 10^{-4} torr and then a very thin gold layer (~few nanometers thick) were sputtered on the sample to ensure the conductivity of the sample surface. Finally it was placed in the main SEM chamber. The acceleration voltage of the electron gun was 5 or 10 kV with probe current zero and the working distance was ~8 mm. Various magnification range was used, varying from 5,000-500,000 times.

4.3.3 Energy Dispersive X-Ray Spectroscopy (EDX) Analysis

The energy dispersive x-ray spectra of the samples were analyzed with Schottky Field Emission Scanning Electron Microscope (JSM-7600F, JEOL) equipped with an EDX detector within the range of 0-12 kV. The acceleration voltage was same as it was used for SEM analysis.

4.3.4 X-Ray Diffraction (XRD) Analysis

The x-ray diffraction pattern of the nanocomposites were recorded with an Ultima IV, Rigaku x-ray diffractometer operating at 40 kV and 40 mA using Cu $K\alpha_1$ radiation (λ = 1.540598 A°), fitted with scientillation detector . The powdered samples were taken within two plain glass slide (25 mm × 75 mm) forming a film, were placed inside the diffractometer. The measurement was performed in the continuous mode with a scan speed of 3.0 deg./min. within the scan range of 10-70 degree while the scan width was 0.02 deg.

4.3.5 Thermogravimetric Analysis (TGA)

The thermogravimetric analysis of the samples were performed with a thermogravimetric analyzer (TGA-50H, Shimadzu) within the range of room temperature to 800°C. In each case, a certain amount of the nanocomposites (< 5 mg) were taken in an alumina cell under nitrogen atmosphere and then subjected to heating with a flow rate of 10°C/min.

4.4 Investigation of the Behaviour in Dye Decolourization

4.4.1 Experimental Setup

To investigate the behaviour of the nanocomposites in dye decolourization, methylene blue (MB) was used as a model dye which imparts a blue appearance to the aqueous solution. First, a stock solution of MB was prepared, which were further used for the preparation of MB solutions of desired concentrations. In each case, a certain amount of the samples was added to a certain amount of MB solution in a reagent bottle and was subjected to shaking at 250 rpm. After the desired time, the solution from reagent bottle was transferred to a falcon tube and was centrifuged at 4000 rpm for ~ 10 minutes. The supernatant was collected in a plastic bottle fitted with cap and was kept under cover to avoid any photo degradation. The effect of the samples on dye solution was studied with UV-Visible spectroscopic analysis technique within 24h - 48h of their combination. With different samples, all the experiments were performed in similar fashion. The experiments were conducted at room temperature (~ 30°C).

4.4.2 UV-Visible Spectral Analysis

The UV-Visible spectral analysis was performed with a double beam UV-Visible spectrophotometer (UV-1800, Shimadzu) using two cells of 1cm path length, transparent to the whole UV-Visible region (200-800 nm). The analysis were performed within 400-800 nm range in auto scan mode with D. I. water as reference.

4.4.2.1 Preparation of Stock Solution

A stock MB solution of 100 mL volume with a concentration of 500 ppm was prepared by dissolving 50 mg of MB (M. W. = 355.89 g) in D.I. water in a 100 mL volumetric flask. This solution was further used for the preparation of MB solutions of desired concentrations using the formulae $V_1S_1 = V_2S_2$.

4.4.2.2 Determination of Molar Absorption Coefficient

Molar absorption coefficient of the MB solutions was determined from a plot of absorbance against concentration (calibration curve) using Beer-Lambert law. To have data for this plot, five different MB solutions of concentrations viz. 1, 3, 5, 7, 10 ppm was prepared and their absorbance value was determined without any further treatment.

4.4.2.3 Determination of Equilibrium Time of Interaction

To find the equilibrium time of interaction, 5 mg of the samples were added with 25 mL 5 ppm MB solution and were allowed to interact for different time intervals viz. 0, 15, 30, 45, 60, 75, 90, 120 minutes. The equilibrium time was found from the concentration of the treated MB solutions with the ternary nanocomposites for different time intervals.

4.4.2.4 Study of the Effect of Contact Time

The effect of contact time was disclosed by observing the concentration of supernatant from mixture of 5 mg sample with 25 mL 5 ppm MB solution for the time intervals viz. 0, 5, 10, 15, 20, 30, 45, 60, 75 minutes.

4.4.2.5 Study of the Effect of pH

The effect of pH was unraveled by conducting experiment at acidic pH 1, 3, and 5, a basic pH 10 and at the neutral pH 7. In each case, 5 mg of the samples were added with 25 mL 5 ppm MB solution and were allowed to interact for the equilibrium time. The pH of the MB solution was adjusted by the addition of dilute HCl or NaOH solution.

4.4.2.6 Study of the Effect of Dose

To understand the dose effect, experiment was conducted with four different amount of

samples viz. 2 mg, 5 mg, 10 mg and 20 mg which were added with 25 mL 5 ppm MB solution and were allowed to interact for the equilibrium time.

4.5 Investigation of Electrochemical Capacitive Behaviour

4.5.1 Experimental Setup

To investigate the electrochemical capacitive behaviour of the nanocomposites, a three electrode system, single compartment cell was employed, which utilized a modified graphite electrode with only an exposed surface area of radius ~ 0.3 cm as working electrode. A rectangular glassy carbon electrode (GCE) and an Ag | AgCl | KCl (sat.) electrode was used as counter electrode and reference electrode respectively. The modification of the graphite electrode was performed by solvent casting and drop drying method. First, 1 mg of active material along with ~ 25% PVA as binder was added to a mixture of 200 µL ethanol (EtOH) and 500 µL dimethyl sulphoxide (DMSO). The mixtures were subjected to sonication in a digital ultrasonic bath for at least 30 minutes. Then, 10 µL of that mixture was casted on graphite electrode surface with a micropipette in a way that, it left no exposed surface area uncovered. Finally, the electrode was dried at 60°C in an oven for several hours which resulted in the formation of a thin film of the sample on graphite surface. The experiments were conducted in an electrolyte solution of 0.5 M Na_2SO_4. Each time, before use, the electrodes were cleaned carefully. The graphite electrode surface was cleaned by polishing mechanically on a smooth piece of paper while the GCE was cleaned by polishing with alumina powder. With different samples, all the experiments were performed in similar fashion. All the electrochemical analysis for a single sample was performed at a time one after another with same setup.

4.5.2 Electrochemical Analysis

The electrochemical characterization of the nanocomposites were carried out in a computer controlled electrochemical working station (760E, CH instruments, USA). Three electrochemical techniques namely cyclic voltammetry (CV), chronopotentiometry (CP) and electrochemical impedance spectroscopy (EIS) was employed in this endeavor. The focus of these experiment were to find out the capacitive behavior of the ternary nanocomposite.

4.5.2.1 Cyclic Voltammetry (CV)

The CV of the samples were performed to find the potential window within which they shows capacitive behavior and its dependency on scan rate. Initially, in each case, CV

was taken within -0.5 V o 1.0 V which was later adjusted to the symmetric shape of cyclic voltammogram that corresponds to capacitive behaviour. Then, CV was performed at different scan rate, starting from 5 mV/s to up to 100 mV/s.

4.5.2.2 Chronopotentiometry (CP)

Chronopotentiometric technique also known as Galvanostatic Charging Discharging (GCD), was used to evaluate the specific capacitance of the samples with different charging-discharging current or current density varying from 0.5 A/g to 5 A/g within suitable potential window chosen from CV. Again, the same potential window was used to find the cyclic stability of the three nanocomposites by observing specific capacitance for first 50 cycles in general and 500 cycles for the the ternary nanocomposite at the current density 5 A/g.

4.5.2.3 Electrochemical Impedance Spectroscopy (EIS)

Electrochemical impedance measurement was carried out to investigate the arranged electrochemical system and measure the equivalent circuit resistance. It was performed at different AC potentials within the potential window used for chronopotentiometric measurement. Impedance data was recorded within the frequency range of 1 Hz to 10^5 Hz with an amplitude of 5 mV and a quiet time of 2 s.

Chapter 5

Results and Discussion

5.1 Synthesis of Materials: Steps of Reactions

5.1.1 Synthesis of Graphene Oxide (GO) and Reduced Graphene Oxide (rGO)

The ternary nanocomposite was synthesized using graphene oxide (GO) as a precursor. GO was synthesized following Hummers method [1], a well-known and commonly adopted technique in this regard [2-3]. According to report, the dark red oil of dimanganese heptoxide formed from the combination of sulfuric acid and potassium permanganate, play the key role in oxygenation of graphite. Sodium nitrate serves as catalyst. Further oxidation occurs by permanganate ion after addition of water and before the addition of hydrogen peroxide, which is used to reduce residual permanganate and manganese dioxide from earlier steps. The washing with HCl and water results GO solution free of impurities [4-5].

$$KMnO_4(aq) + 3\,H_2SO_4(aq) \rightarrow K^+(aq) + MnO_3^+(aq) + H_3O^+(aq) + 3\,HSO_4^-(aq)$$

$$KMnO_4(s) \rightarrow K^+(aq) + MnO_4^-(aq)$$

$$MnO_3^+(aq) + MnO_4^-(aq) \rightarrow Mn_2O_7(l)$$

$$\text{Graphite} + Mn_2O_7(l) \rightarrow GO$$

rGO was obtained by heating GO at 400°C under inert (N_2) atmosphere for 1.5 hr. The mechanism behind this lies in the sudden expansion of CO or CO_2 gases into spaces between graphene sheets during the rapid heating. The rapid temperature increase makes the oxygen containing functional groups attached on carbon plane decompose into gases that create huge pressure between the stacked layers. A pressure of ~ 50 MPa is generated at 400°C whereas a pressure of only 2.5 MPa is enough to separate two stacked GO platelets. However, high temperature is essential to ensure the removal of interlayer water with a greater extent of oxygen containing functional groups while a very high temperature also affects the resulting structure by leaving too much structural damage and causing extreme weight loss. The use of inert atmosphere was important to facilitate the etching of oxygen at higher temperature [6-7].

$$GO \xrightarrow{400°C,\ N_2,\ 1.5\,hr} rGO$$

5.1.2 Synthesis of rGO/Mn-oxide/Sn-oxide Ternary Nanocomposite

Having no prior report of synthesis of graphene based ternary nanocomposite of Mn-

oxide with Sn-oxide, trial and error method was employed in this venture with knowledge from reports on the corresponding binary nanocomposites. The effort resulted into success in the first attempt.

The mixture of GO with $Mn(CH_3COO)_2.2H_2O$ at a ratio of almost 1 **:** 5, in isopropyl alcohol was first subjected to sonication to make sure the presence of properly exfoliated GO sheet as well as to help $Mn(CH_3COO)_2.2H_2O$ disintegrate into the solution[8]. At this stage, the Mn^{2+} ions formed from the salt of manganese, preferably bound with the oxygen atoms of negatively charged, oxygen containing functional groups on GO sheets via electrostatic force. With the addition of $KMnO_4$ solution at an elevated temperature, a redox reaction occurred between its MnO_4^- ion and the already present Mn^{2+} ion, leading to the formation of manganese oxide. The Mn atoms may have formed co-ordinate covalent bond with oxygen atoms of the functional groups from GO surface, acting as anchor sites for the crystals to grow [9].

$$Mn(CH_3COO)_2.2H_2O\ (s) \rightarrow\ Mn^{2+}(aq) + 2\ CH_3COO^-(aq) + 2\ H_2O\ (l)$$

$$KMnO_4(s)\ \rightarrow\ K^+(aq) + MnO_4^-(aq)$$

$$3\ Mn^{2+}(aq) +\ 2\ MnO_4^-(aq) + 2\ H_2O \rightarrow\ 5\ MnO_2(s) + 4\ H^+(aq)$$

Next, $SnCl_2.2H_2O$, at an amount, half to the amount of $Mn(CH_3COO)_2.2H_2O$ was introduced with the product in D.I. water, which is slightly acidic in nature and helps stannous chloride to dissolve into it. The Sn^{2+} ions from $SnCl_2$, bind them with the available oxygenated groups on GO surface through electrostatic attraction [10]. Later, it converted itself spontaneously into SnO_2 while reducing GO to reduced graphene oxide (rGO) [11]. The reduction is reported to occur best at 30°C [12].

$$SnCl_2(aq) + GO + H_2O(l) \rightarrow SnO_2(s) + rGO + 2HCl(l)$$

The extent of reduction of rGO in the composite along with the order of crystallinity of the nanoparticles was further increased by heating at 400°C under inert (N_2) atmosphere for 1.5 hr [11]. The remaining small amount of oxygen containing groups help to maintain a dispersion of the existing metal oxide nanoparticles through co-ordinate covalent bonding and hydrogen bonding [9, 11]. However, with increasing crystallinity, the heating also affected the structure of the nanoparticles, particularly of MnO_2. It was converted into Mn_3O_4 and MnO [13-14].

$$3MnO_2(s) \rightarrow Mn_3O_4(s) + O_2(g)$$

$$2C(s) + O_2(g) \rightarrow CO(g)$$

$$MnO_2(s) + CO(g) \rightarrow MnO(s) + CO_2(g)$$

5.1.3 Synthesis of rGO/Mn-oxide and rGO/Sn-oxide Binary Nanocomposite

The binary nanocomposites were prepared exactly in the same way as it was employed for the ternary nanocomposite except omitting the third and the second step for the synthesis of rGO/Mn-oxide and rGO/Sn-oxide binary nanocomposite respectively. In absence of any reducing agent in case of rGO/Mn-oxide binary nanocomposite, thermal annealing made sure the conversion of GO to rGO [6]. Besides, absence of oxygen helps to convert MnO_2 to Mn_3O_4 preferentially over MnO.

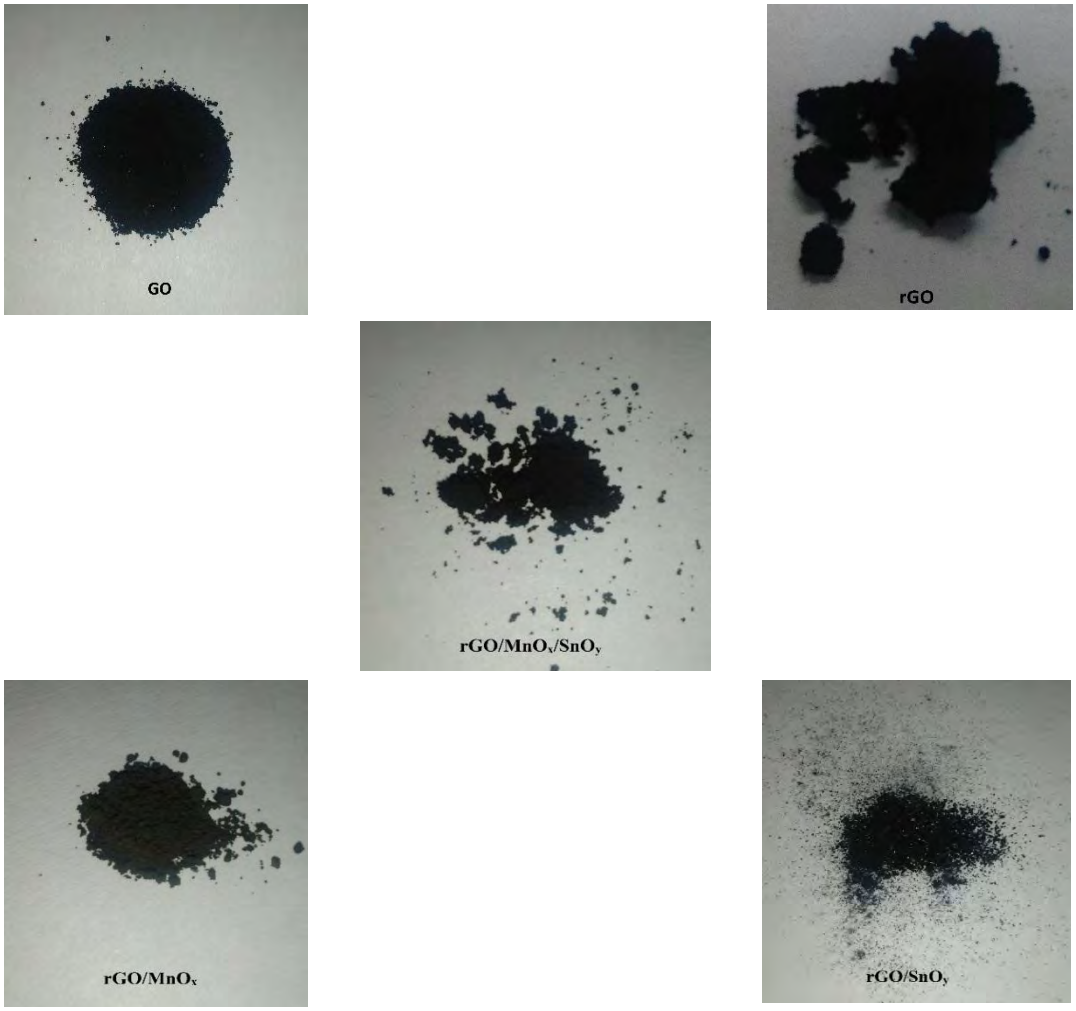

Fig. 5.1- Optical image of the prepared samples

5.2 Structural Characterization

5.2.1 Fourier Transform Infrared Spectroscopy (FTIR) Analysis

5.2.1.1 Graphene Oxide (GO)

The FTIR spectra of GO suggests the presence of various oxygen containing functional groups on its surface assuring its formation. The strong broad peak centered at 3420 cm^{-1} of stretching vibration of O–H bond refers to alcohol and carboxylic acid groups as well as adsorbed water molecules [15]. The weak sharp peak centered at 1720 cm^{-1} of C=O stretching vibration denotes the presence of carboxylic group and carbonyl moieties. The weak broad peak centered at 1250 cm^{-1} of stretching vibration of C-O bond refers to the presence of epoxy group. The presence of these groups is further strengthened by the occurrence of weak broad peak centered at 1365 cm^{-1} corresponding to deformed C-OH stretching vibration and medium sharp peak centered at 1060 cm^{-1} corresponding to C-O stretching vibration of alkoxy groups [16-17].

The medium sharp peak centered at 1620 cm^{-1} is mainly from stretching vibration of C=C bond indicating the presence of sp^2 hybridized carbon along with contribution from bending vibration of O-H bond resulting higher intensity [18-19]. The weak sharp peak centered at 2360 cm^{-1} corresponds to stretching vibration of C=O bond within CO_2 molecule, erupts during drying of GO in addition to atmospheric CO_2 [20].

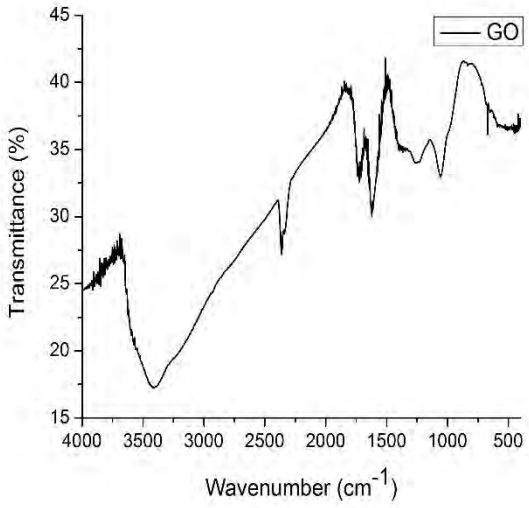

Table 5.1- FTIR bands of GO

Frequency (cm^{-1})	Functional groups
3420	**O-H** (alc./water)
2360	**C=O** (CO_2)
1720	**C=O** (carbonyl)
1620	**C=C** (sp^2 hybrid.)
1365	**C-OH** (deformed)
1250	**C-O-C** (epoxy)
1060	**C-O** (alkoxy)

Fig. 5.2- FTIR spectra of GO

5.2.1.2 Reduced Graphene Oxide (rGO)

The reduction of GO via thermal annealing was primarily confirmed by FTIR analysis. The absence of C=O carbonyl peak (1720 cm^{-1}), C-OH deformed bond peak (1365 cm^{-1}) and C-O alkoxy peak (1060 cm^{-1}) indicate the removal of the corresponding groups while the peak at 3450 cm^{-1} corresponding to O-H stretching vibration and the peak at 1230 cm^{-1} corresponding to C-O-C with reduced intensity indicates the presence of alcoholic and epoxy groups respectively at a lower extent compared to GO [17]. Also, the peak at 1120 cm^{-1} of stretching vibration of C-O-H claims incomplete reduction [21]. The peak at 1580 cm^{-1} comes from C=C skeletal vibration, free of the influence of O-H bending vibration [15]. Thus, it is safe to assume that rGO has been formed.

The peak at 2360 cm^{-1} corresponds to stretching vibration of C=O bond within CO_2 molecule, erupted during thermal annealing of GO in addition to atmospheric CO_2 [20]. No significant bond could be found related to the peaks around 600cm^{-1} assuming them as impurity.

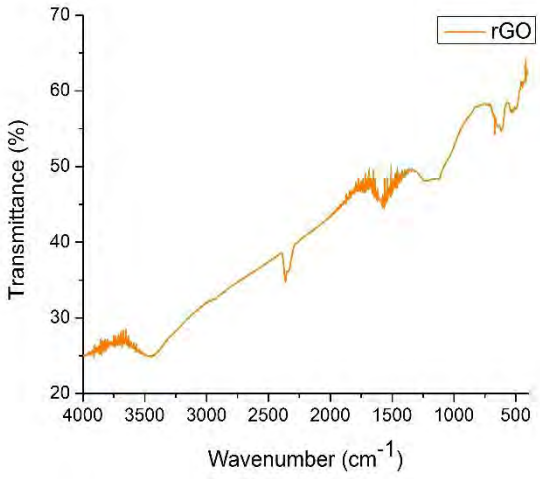

Table 5.2- FTIR bands of rGO

Frequency (cm^{-1})	Functional groups
3450	**O-H** (alc./Water)
2360	**O=C=O** (CO_2)
1580	**C=C** (sp^2)
1230	**C-O-C** (epoxy)
1120	**C-O-H** (alc.)

Fig. 5.3- FTIR spectra of rGO

5.2.1.3 rGO/Mn-oxide Binary Nanocomposite

The FTIR of rGO/Mn-oxide shows peaks at 610 cm^{-1} corresponding to Mn-O stretching vibration and at 493 & 423 cm^{-1} corresponding to Mn-O bending vibration indicating the presence of Mn-oxide [21]. The peak at 1581 cm^{-1} refers to C=C skeletal vibration of graphene while the peaks at 3450, 1378, 1250 corresponding to O-H, C-OH and C-O-C respectively predicts the presence of certain functional groups along with water indicating rGO [18]. The peak at 2360 for C=O stretching vibration of CO_2 is present as usual.

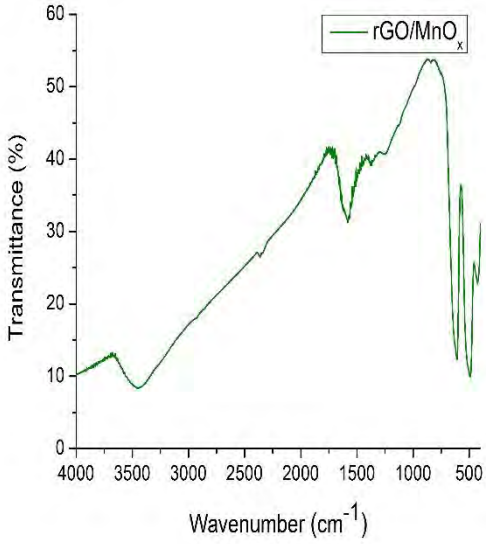

Table 5.3- FTIR bands of rGO/Mn-oxide binary nanocomposite

Frequency (cm^{-1})	**Functional groups**
3450	**O-H** (alc./Water)
2360	**O=C=O** (CO_2)
1581	**C=C** (sp^2)
1378	**C-OH** (deform.)
1250	**C-O-C** (epoxy)
610	**Mn-O** stretching
493 & 423	**Mn-O** bending

Fig. 5.4- FTIR spectra of rGO/Mn-Oxide binary nanocomposite

5.2.1.4 rGO/Sn-oxide Binary Nanocomposite

The FTIR of rGO/Sn-oxide binary nanocomposite shows peak at 630 cm^{-1} of O-Sn-O antisymmetric stretching vibration with subsequent shoulder indicating the formation of SnO_2 nanoparticle on rGO sheet where weak broad peak of O-H (3420 cm^{-1}) and C-O-C (1210 cm^{-1}) along with sharp peak of skeletal C=C vibration (1560 cm^{-1}) make sure higher extent of reduction of GO. The peak at 2360 for C=O stretching vibration of CO_2 is present as usual [18, 22].

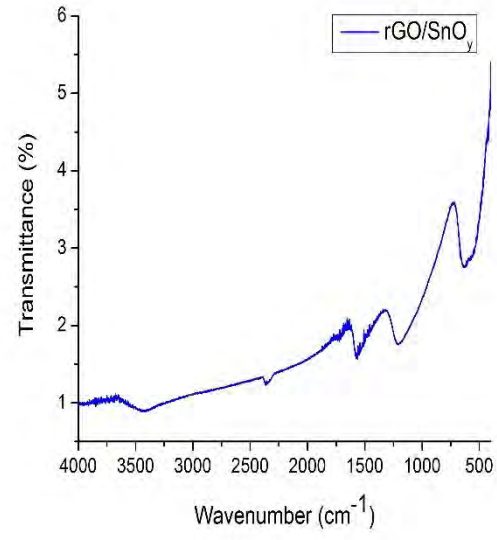

Table 5.4- FTIR bands of rGO/Sn-oxide binary nanocomposite

Frequency (cm^{-1})	**Functional groups**
3420	**O-H** (alc./Water)
2360	**O=C=O** (CO_2)
1560	**C=C** (sp^2)
1210	**C-O-C** (epoxy)
630	**O-Sn-O** stretching

Fig. 5.5- FTIR spectra of rGO/Sn-oxide binary nanocomposite

5.2.1.5 rGO/Mn-oxide/Sn-oxide Ternary Nanocomposite

The formation of the ternary nanocomposite can be identified from the presence of almost all of the peaks from rGO, rGO/Mn-oxide and rGO/Sn-oxide in FTIR spectrum. The major peaks at 3420 cm^{-1}(O-H, stretching), 1620 cm^{-1}(C=C, skeletal vibration), 603 cm^{-1}(O-Sn-O, stretching) and 533 cm^{-1}(Mn-O, bending) confirms the synthesis.

Relatively higher intensity of O-H bond in the ternary nanocomposite compared to its binaries might be due to the interlayer trapped water [23].

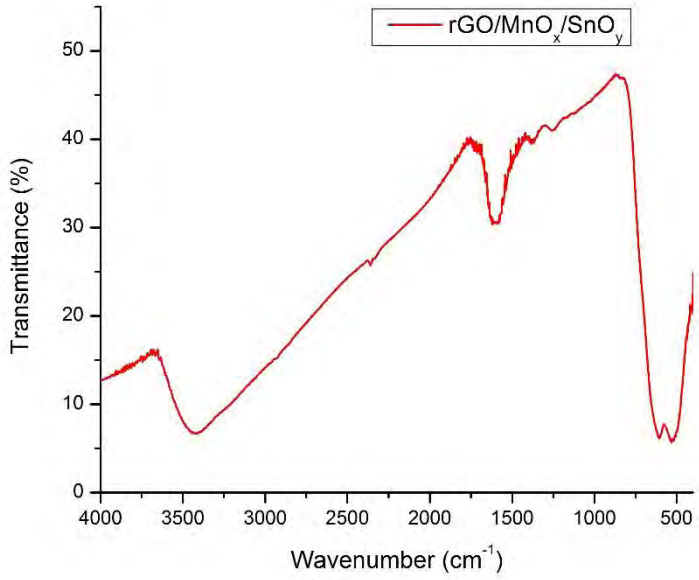

Fig. 5.6- FTIR spectra of rGO/Mn-oxide/Sn-oxide ternary nanocomposite

Table 5.5- FTIR bands of rGO/Mn-oxide/Sn-oxide ternary nanocomposite

Frequency (cm^{-1})	Functional groups
3420	**O-H** (alc./Water)
2360	**O=C=O** (CO_2)
1620	**C=C** (sp^2)
1380	**C-OH** (deform.)
1260	**C-O-C** (epoxy)
603	**O-Sn-O** stretching
533 & 416	**Mn-O** bending

FTIR data of all of the samples and their corresponding peaks can be briefly described as below-

Table 5.6- FTIR bands of GO, rGO and nanocomposites

Frequency (cm^{-1})	Functional groups	Frequency (cm^{-1})	Functional groups
~ 3420	**O-H** (alc./water)	~ 610	**Mn-O** stretching
2360	**C=O** (CO_2)	~ 493 & ~ 423	**Mn-O** bending
~ 1720	**C=O** (carbonyl)		
~ 1620	**C=C** (sp^2 hybrid.)	~ 630	**O-Sn-O** stretching
~ 1365	**C-OH** (deformation)		
~ 1250	**C-O-C** (epoxy)		
~ 1060	**C-O** (alkoxy)		

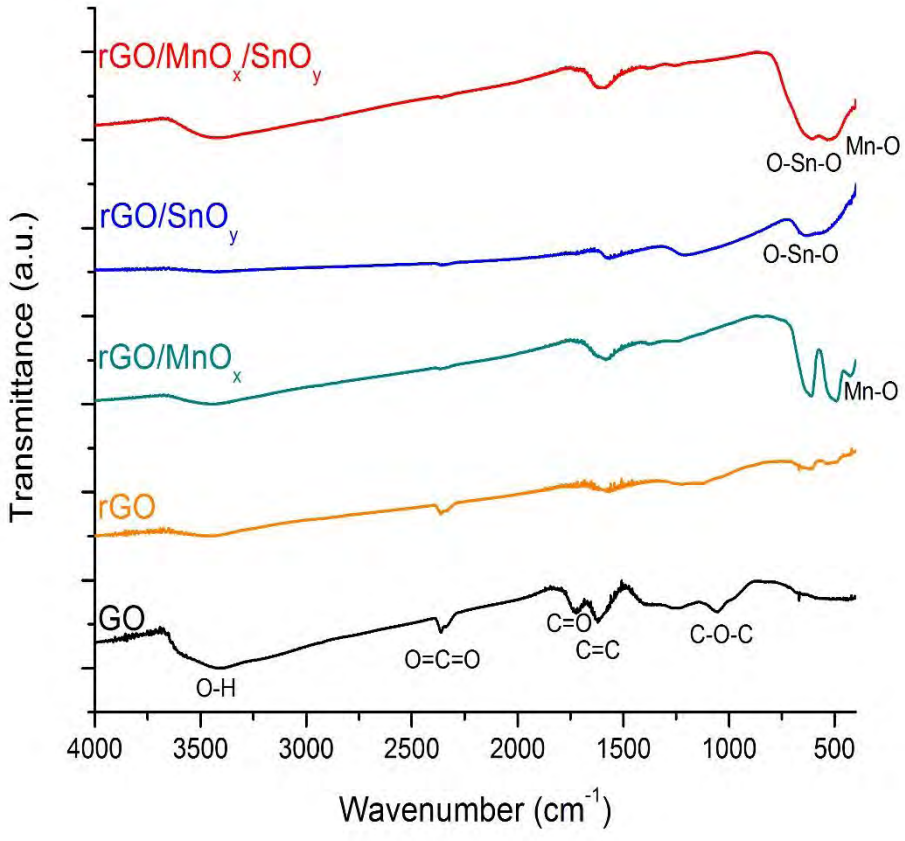

Fig. 5.7- FTIR spectra of GO, rGO and the nanocomposites

5.2.2 Scanning Electron Microscope (SEM) Analysis

5.2.2.1 Graphene Oxide (GO)

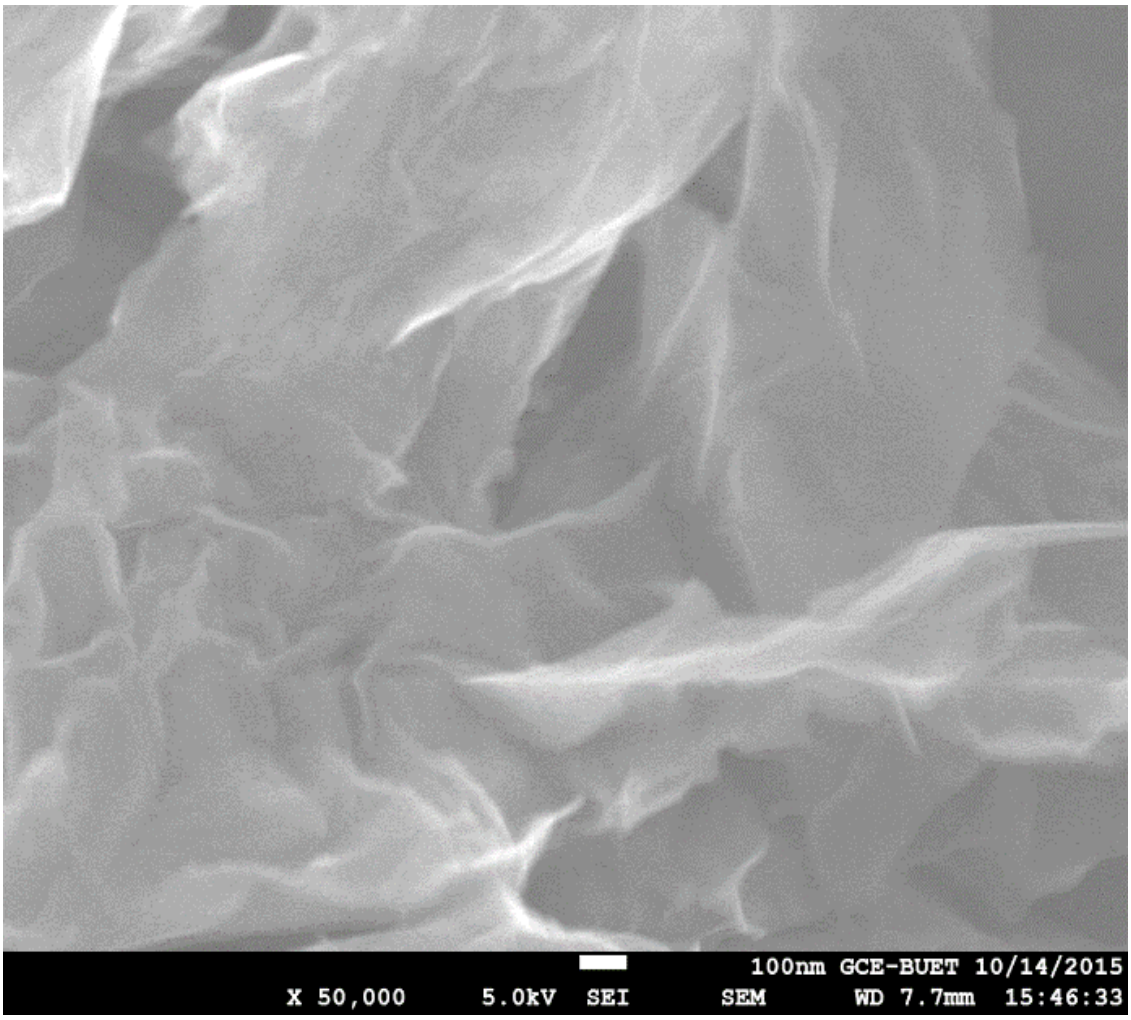

Fig. 5.8- SEM image of GO

The SEM image shows strong disorder and crumpled state of ultrathin GO sheets. There are also huge spacing between the layers indicating a successful introduction of oxygenated groups among the layers of graphite. Although the thickness of the GO layer cannot be verified from SEM image [24], it seems to be apparently ~ 10 nm.

5.2.2.2 Reduced Graphene Oxide (rGO)

The SEM image of rGO shows a clear change in the morphology than the earlier shown GO. As the reduction process reduces oxygen containing groups, the sheets undergo shrinking with smaller in between spacing, as seen in the above image with an apparent thickness of ~ 5 nm. The rGO sheet has assumed a flake like structure with rippled surface

which are due to the thermodynamic requirement for the existence of out-of-plane bending with interatomic interaction generating a mathematical paradox [25].

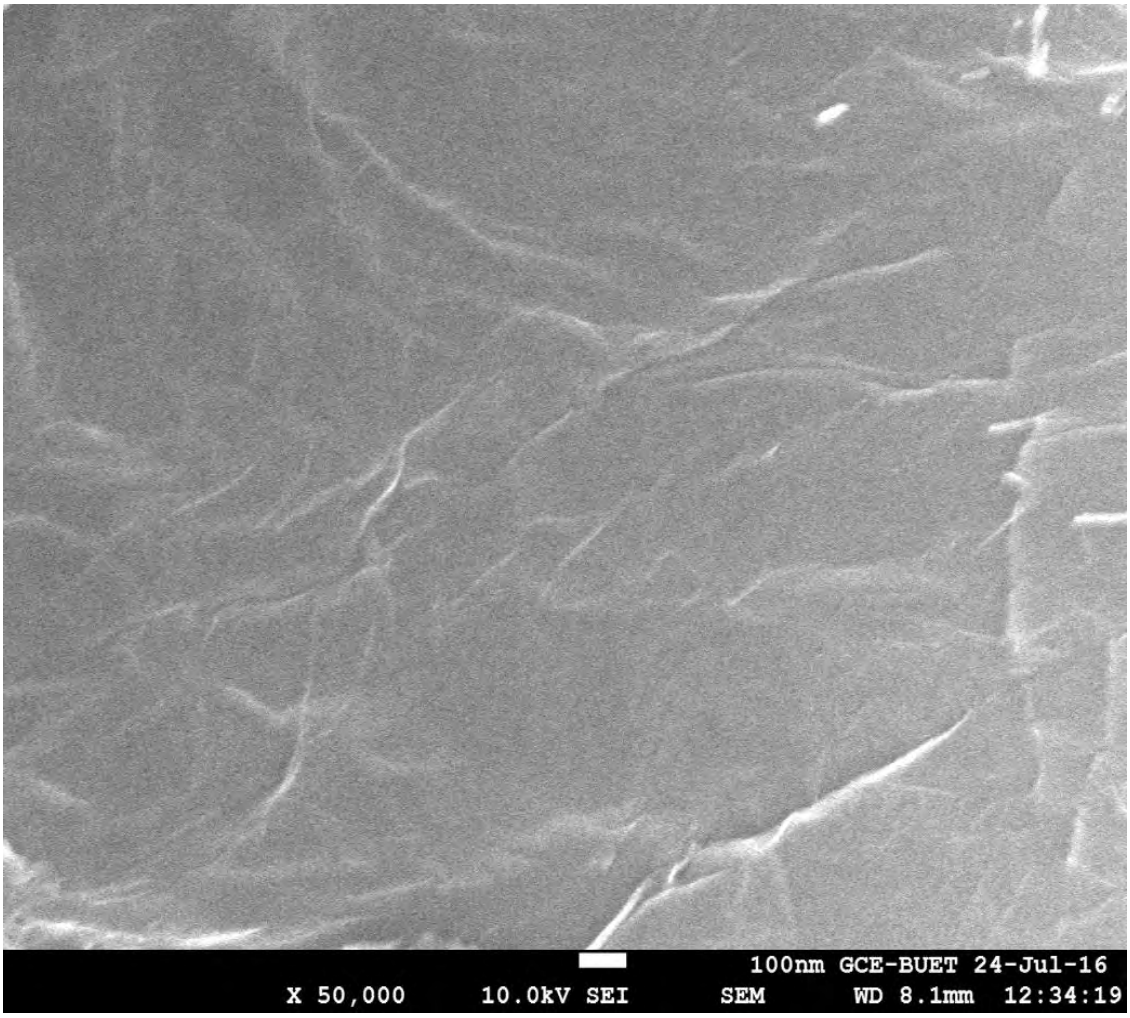

Fig. 5.9- SEM image of GO

5.2.2.3 rGO/Mn-oxide Binary Nanocomposite

The SEM image of the rGO/Mn-oxide primarily shows a high yield of manganese oxide nanoparticles covering the surface of rGO, with almost homogenous dispersion with a porous surface which may play an important role in its applications. There are two different types of geometry of manganese oxide-rod like structure and cubic structure indicating possible presence of multiple phase of manganese oxide. The rod like structures show a diameter of ~ 25 nm with varying length upto1 μm. On the other hand, the cubic structure shows side length of ~ 50 nm.

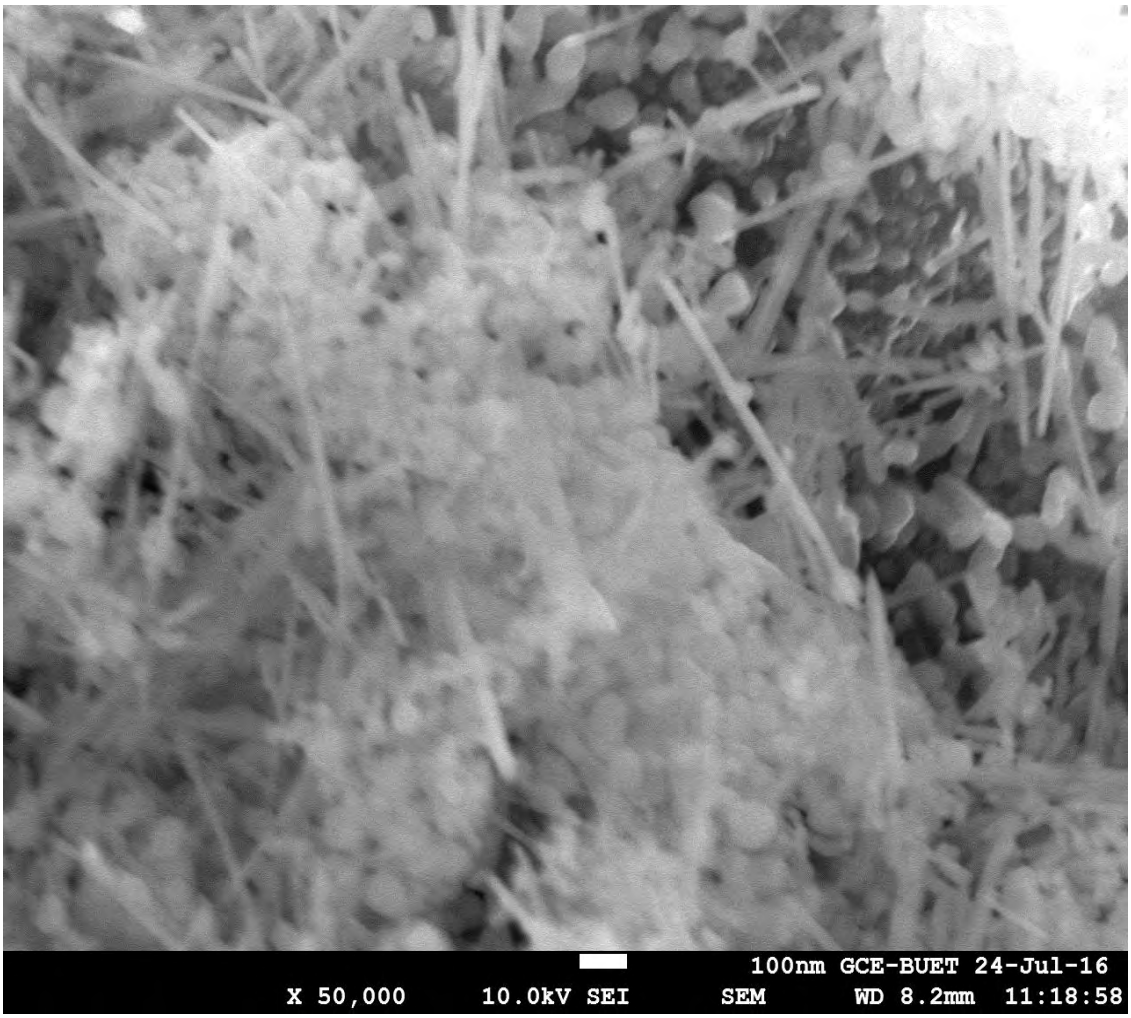

Fig. 5.10- SEM image of rGO/Mn-oxide

5.2.2.4 rGO/Sn-oxide Binary Nanocomposite

The SEM image of rGO/SnO_2 shows a uniform dispersion of SnO_2 nanoparticles on sheet like rGO surface indicating its successful reduction from GO. The tin oxide nanoparticles are seen to be forming a structure with average side length of ~ 5 nm. The image also shows that the presence of tin oxide prevents the crumpling of rGO sheets.

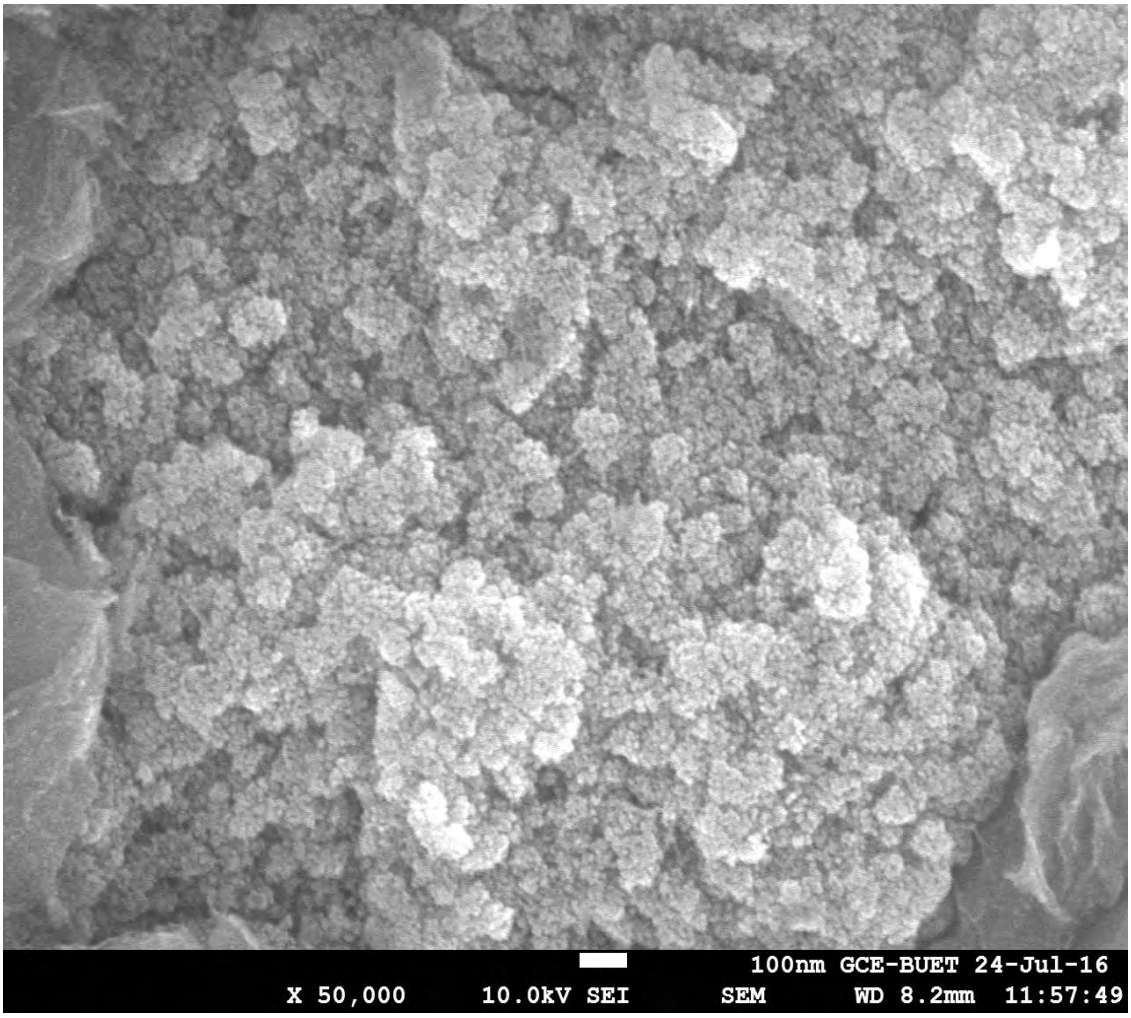

Fig. 5.11- SEM image of rGO/Sn-oxide

5.2.2.5 rGO/Mn-oxide/Sn-oxide Ternary Nanocomposite

The SEM image of rGO/Mn-oxide/Sn-oxide annealed at 400°C under N_2 atmosphere for 1.5 hr clearly shows the presence of different types of nanoparticles on rGO surface. There is a chain like structure of manganese oxide with diameter less than 10 nm and length higher than 1 μm. Besides there are two types of structure, one with 5-10 nm side length of tin oxide and another with 15-20 nm side length of manganese oxide. Thus the composite contain oxides of both of manganese and tin. It is notable that the chain like nanoparticle is present at a lesser extent than the cubic shaped nanoparticles.

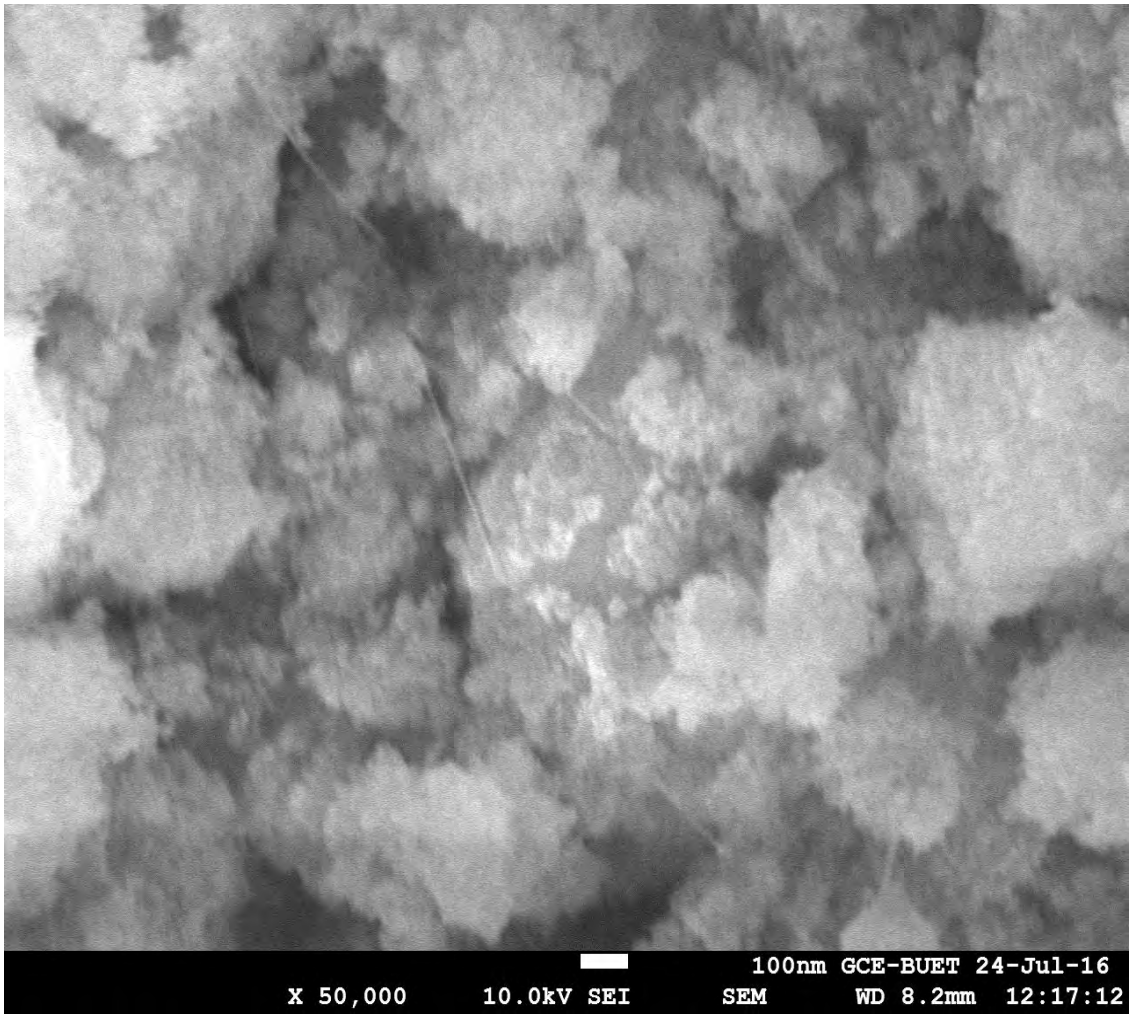

Fig. 5.12- SEM image of rGO/Mn-oxide/Sn-oxide

5.2.3 Energy Dispersive X-Ray Spectroscopy (EDX) Analysis

5.2.3.1 Graphene Oxide (GO)

Depending upon the preparation method, GO with chemical compositions ranging from $C_8O_2H_3$ to $C_8O_4H_5$, corresponding to a C/O ratio of 4:1–2:1, is typically produced. The EDX of the synthesized GO shows the C/O atomic ratio 5.4:1, which is almost same to the typical value [6]. Thus the obtained data is in agreement with the formation of GO.

Table 5.7- Elemental composition of GO

Sample Location	C (atomic %)	O (atomic %)
1	84.78	15.22
2	84.46	15.54
3	84.15	15.85
Average	**84.46**	**15.54**

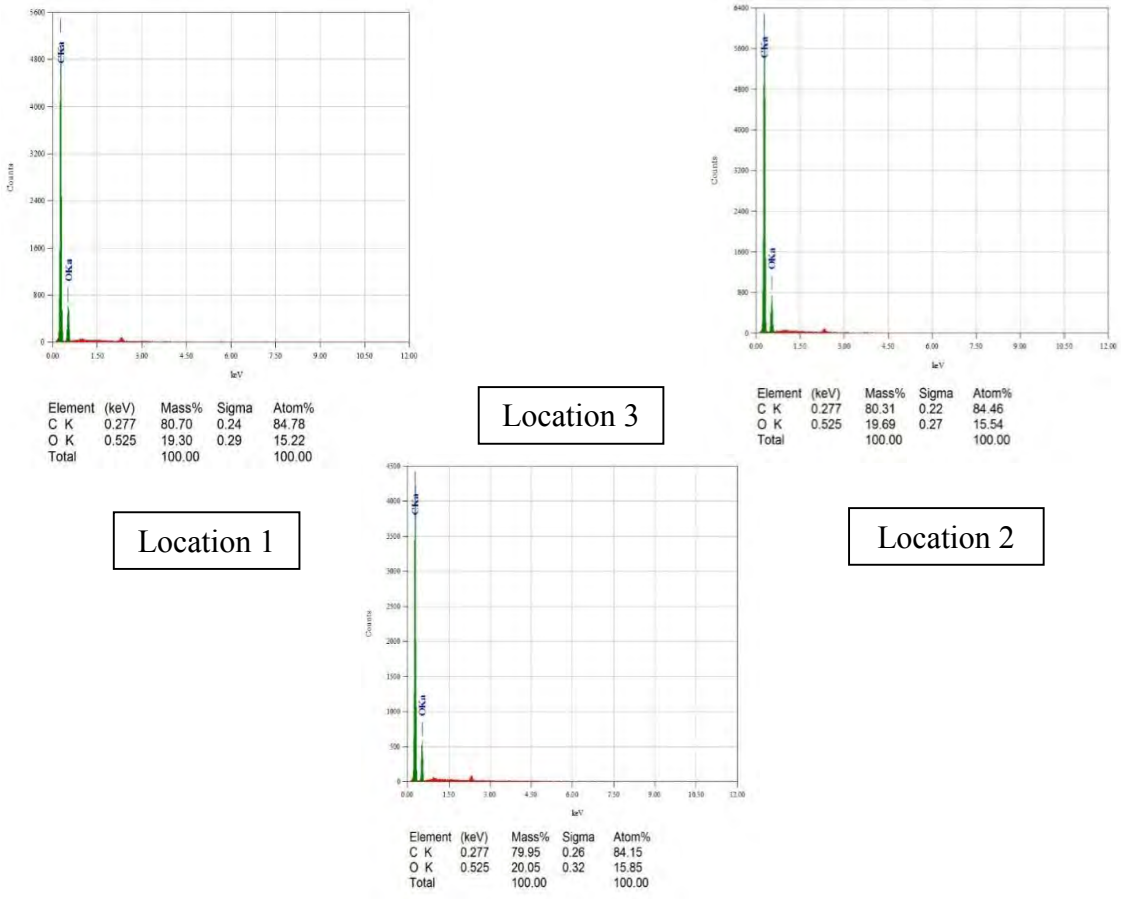

Fig. 5.13- EDX spectra of GO

5.2.3.2 Reduced Graphene Oxide (rGO)

Reduction of graphene oxide leads to a C/O atomic ratio of 12:1 in most cases. In present case, the EDX of rGO shows a C/O atomic ratio of 20.9 from 5.4 in GO, which is much higher than the typical value showing that the synthesized product is almost close to graphene. However, there are still a significant amount of oxygen atom present, indicating it is more perfect to call it rGO.

Table 5.8- Elemental composition of rGO

Sample Location	C (atomic %)	O (atomic %)
1	95.29	4.71
2	95.56	4.44
3	95.46	4.51
Average	**95.44**	**4.56**

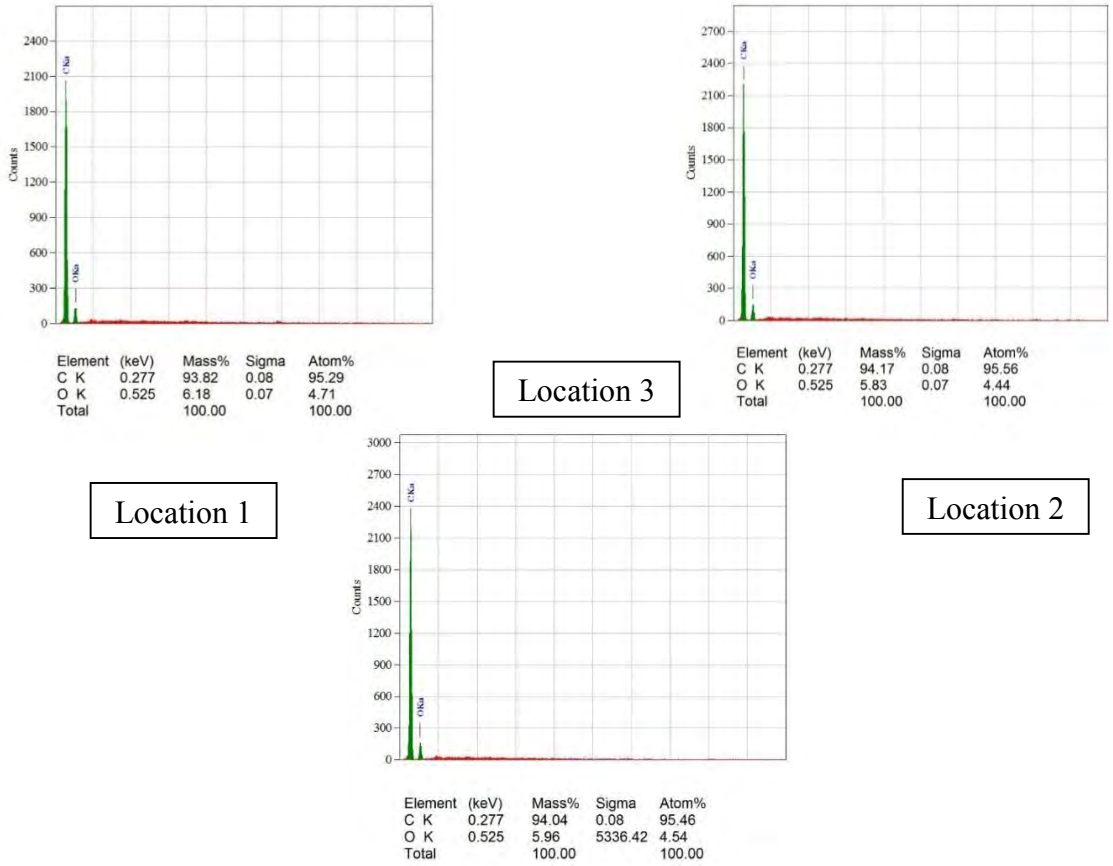

Fig. 5.14- EDX spectra of rGO

5.2.3.3 rGO/Mn-oxide Binary Nanocomposite

The EDX of rGO/Mn binary nanocomposite is a clear evidence of the formation of manganese oxide nanoparticle on reduced graphene oxide sheet. The relative abundance of oxygen atom compared to manganese atom can attributed to the presence of moisture along with some oxygen containing functional group of rGO.

Table 5.9- Elemental composition of rGO/Mn-oxide

Sample Location	**C (**atomic **%)**	**O (**atomic **%)**	**Mn (**atomic **%)**
1	67.56	25.18	7.26
2	66.05	27.09	6.85
3	50.12	37.33	12.55
Average	**61.24**	**29.87**	**8.88**

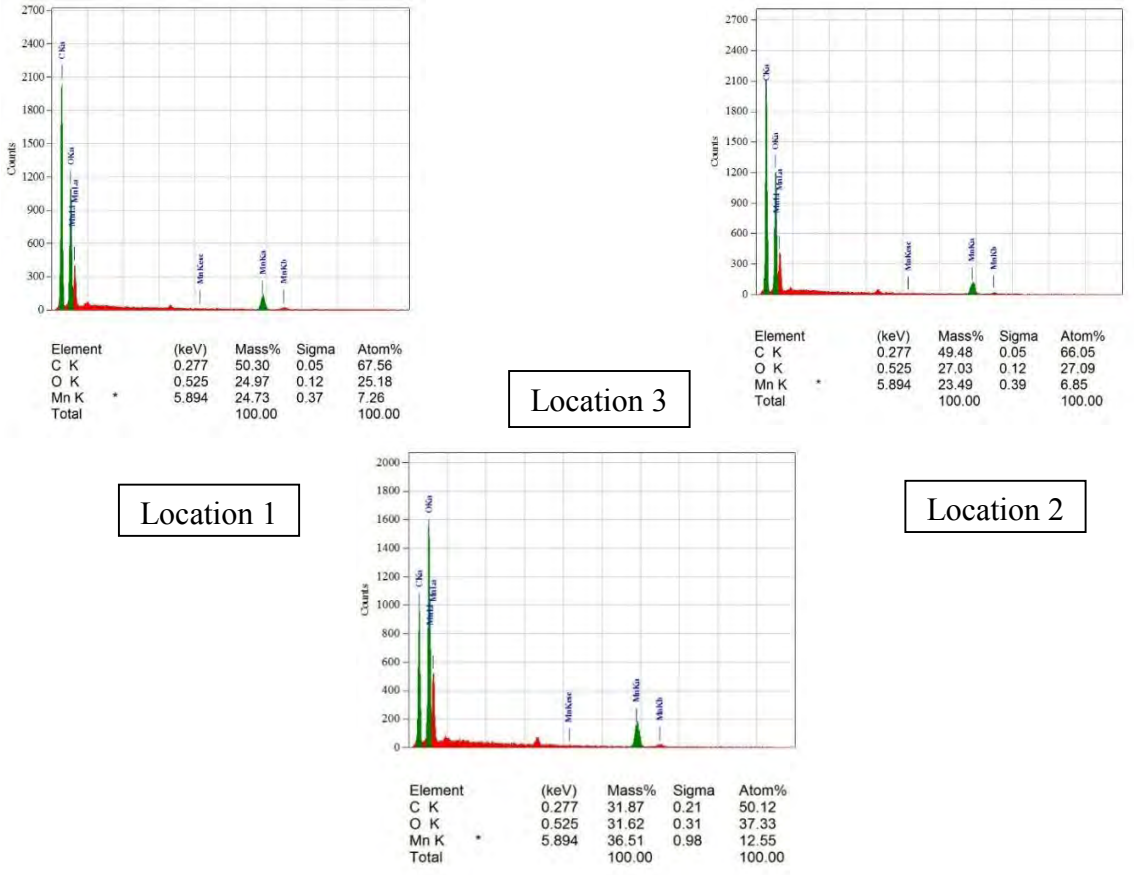

Fig. 5.15- EDX spectra of rGO/Mn-oxide

5.2.3.4 rGO/Sn-oxide Binary Nanocomposite

The EDX of rGO/Sn-oxide binary nanocomposite shows presence of a significant amount of tin atom supporting the formation tin oxide nanoparticle on rGO surface. Higher amount of oxygen atom compared to tin indicate the presence of higher extent of moisture in the composite structure.

Table 5.10- Elemental composition of rGO/Sn-oxide

Sample Location	C (atomic %)	O (atomic %)	Sn (atomic %)
1	56.87	35.59	7.54
2	57.74	34.94	7.32
3	61.92	30.96	7.12
Average	**58.84**	**33.83**	**7.33**

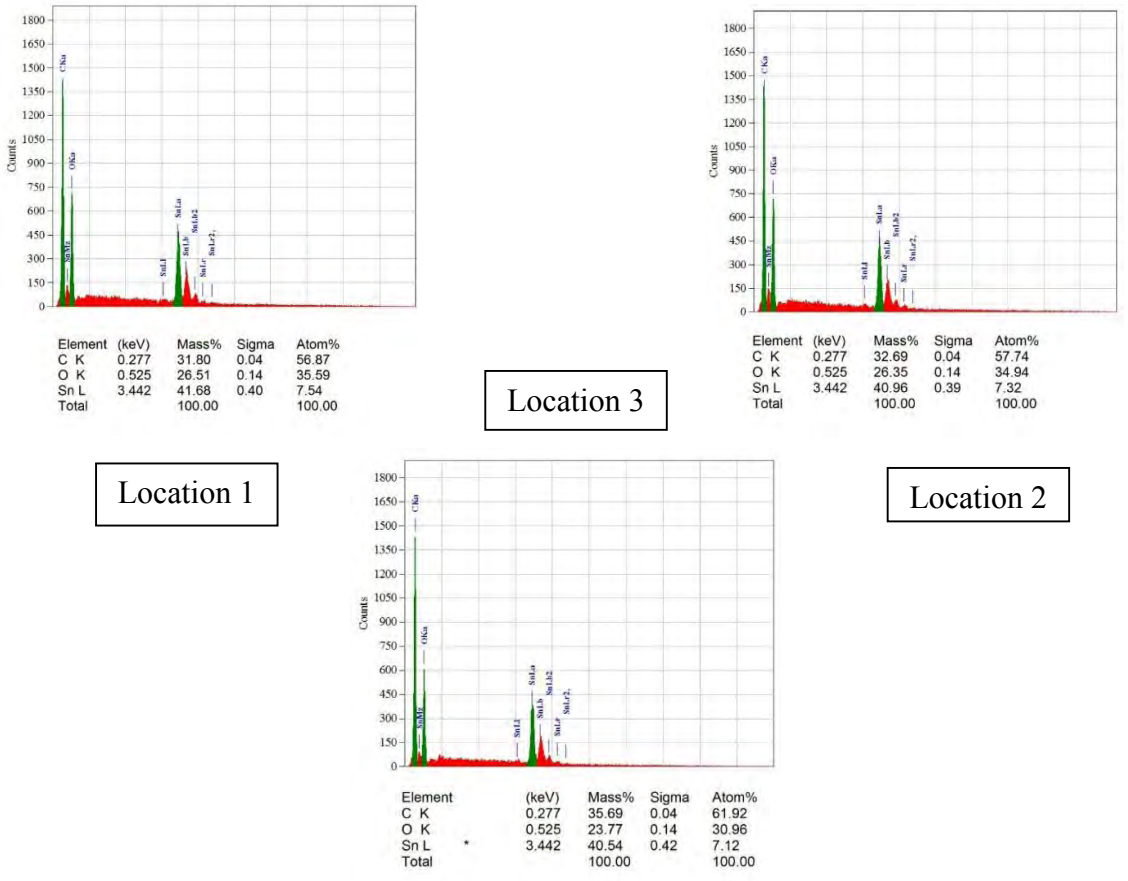

Fig. 5.16- EDX spectra of rGO/Sn-oxide

5.2.3.5 rGO/Mn-oxide/Sn-oxide Ternary Nanocomposite

The EDX of the rGO/Mn-oxide/Sn-oxide ternary nanocomposite heated under inert shows the presence of a balanced amount of manganese and tin which are present as their oxides suggesting a higher amount of loading of nanoparticles on rGO surface.

Table 5.11- Elemental composition of rGO/Mn-oxide/Sn-oxide

Sample Location	**C (atomic %)**	**O (atomic %)**	**Mn (atomic %)**	**Sn (atomic %)**
1	55.32	30.93	9.53	4.21
2	58.10	27.57	11.01	3.33
3	61.56	24.18	11.19	3.07
Average	**58.32**	**27.56**	**10.58**	**3.54**

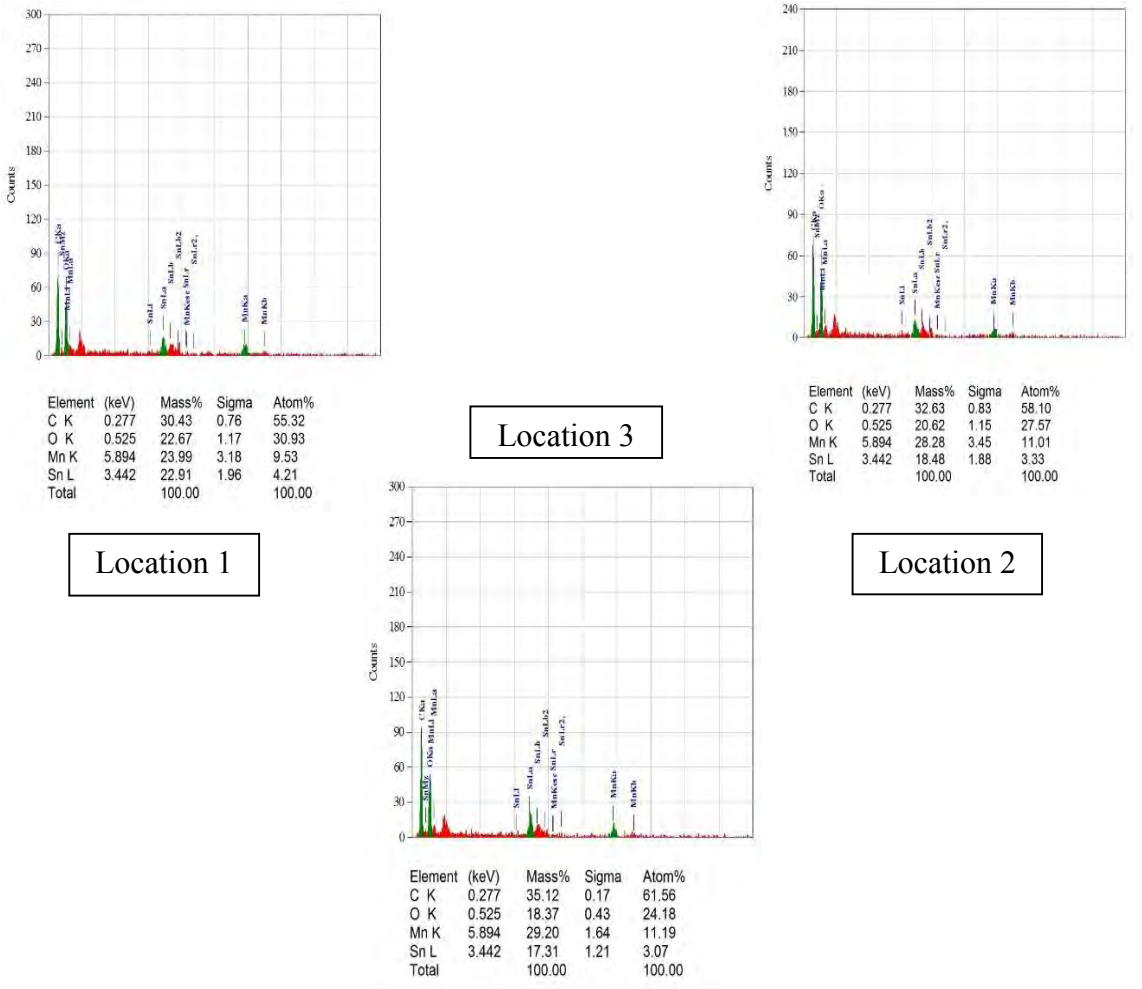

Fig. 5.17- EDX spectra of rGO/Mn-oxide/Sn-oxide

5.2.4 X-Ray Diffraction (XRD) Analysis

5.2.4.1 Graphene Oxide (GO)

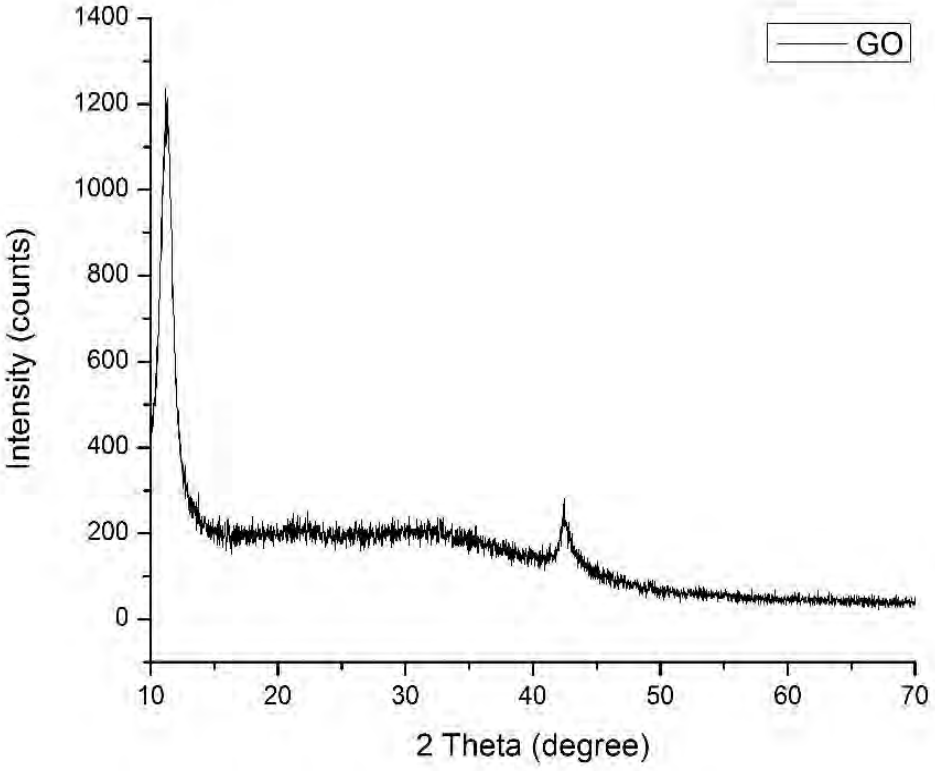

Fig. 5.18- XRD pattern of GO

The XRD pattern of the synthesized GO via Hummers method is shown in the figure. It shows a strong, sharp peak at 2θ = 11.26° belongs to the (001) reflection of GO indicating a successful conversion of graphite powder to graphene oxide [26]. Using the Scherrer formulae the interlayer spacing was found to be 7.85 Å, much higher than that of pristine graphite (3.4 Å), attributed to the presence of various oxygen containing functional groups at the basal plane of GO. The weak peak at 2θ = 42.35° belongs to the (101) plane of graphite, indicating the traces of the starting material (graphite flake) at a very low extent [27].

5.2.4.2 Reduced Graphene Oxide (rGO)

The XRD pattern of rGO obtained from GO through thermal annealing at 400°C shows characteristic peak at 2θ = 24.75° and 2θ = 43.5° belongs to the (002) and (100) plane of graphene layer respectively signaling almost complete reduction of GO (**JCPDS No. 75-**

1621) [28]. The interlayer spacing fall to 3.59 Å from 7.85 Å of GO, which is in agreement with the removal of oxygen containing functional groups from GO sheets due to thermal annealing.

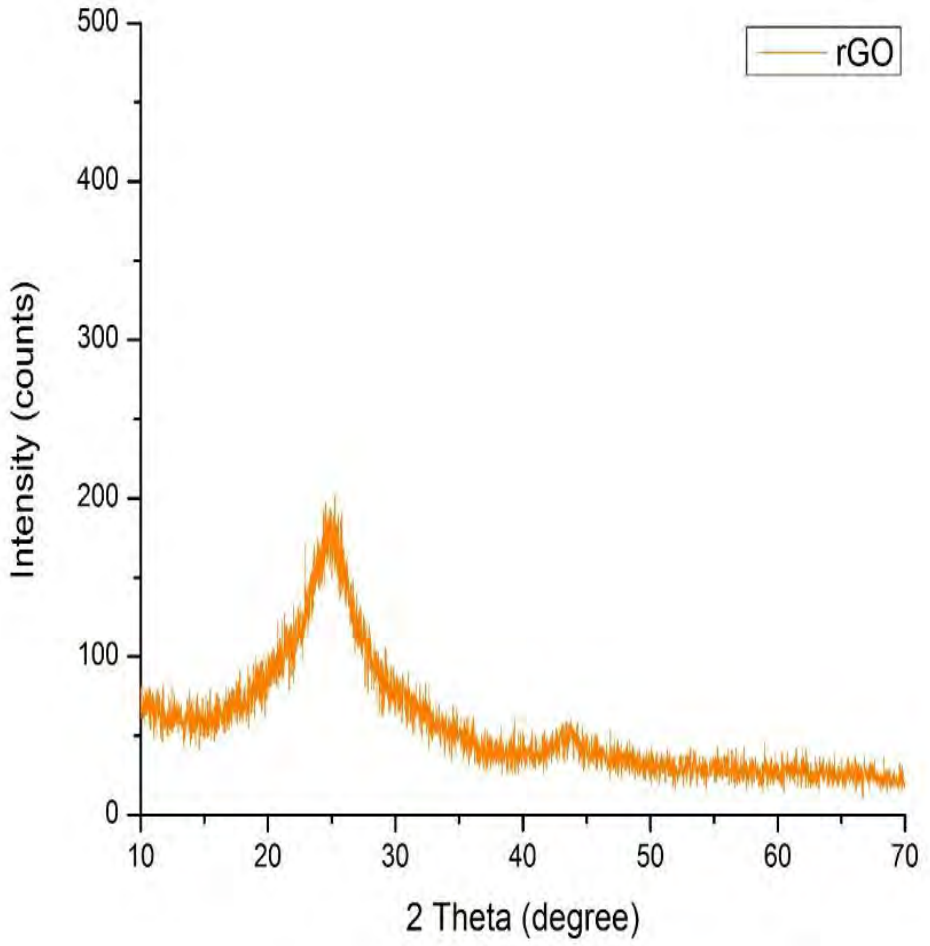

Fig. 5.19- XRD pattern of rGO

5.2.4.3 rGO/Mn-oxide Binary Nanocomposite

The XRD of the rGO/Mn-oxide nanocomposite shows the formation of Mn_3O_4 and MnO on the surface of rGO. The peaks at 2θ values 18°, 28.9°, 32.3°, 36°, 38°, 44.4°, 50.64°, 54.05°, 56.1°, 59.8°, 64.6° are attributed to (211), (112), (105), (211), (004), (220), (105), (015), (303), (224), (440) planes of Mn_3O_4 (**JCPDS card no. 24-0734**, Space group: $I4_1/amd$; Structure: Tetragonal (Spinel); a = 5.762 Å, b = 5.762 Å, c = 9.469 Å) and 2θ values 35°, 40.57°, 58.7° are attributed to (111), (200), (224) planes of MnO (**JCPDS**

card no. 75-1090, Space group: Fm3m; Lattice system: Cubic (Rocksalt); a = 4.430 Å, b = 4.430 Å, c = 4.430 Å) [29-31] .

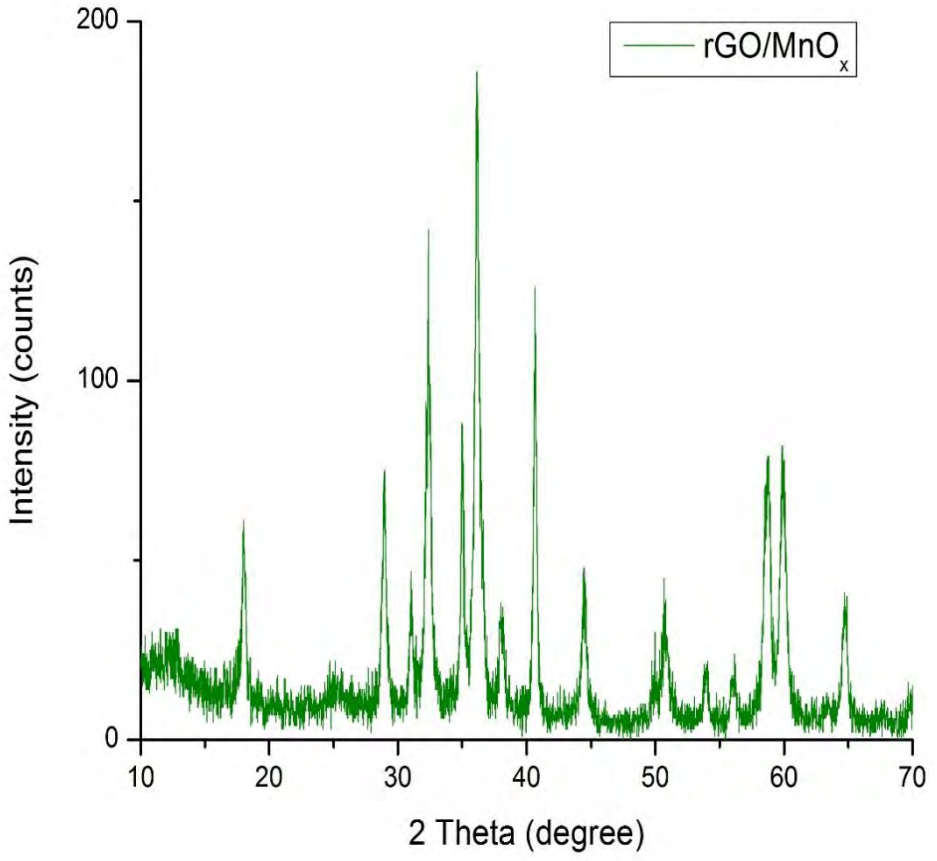

Fig. 5.20- XRD pattern of rGO/Mn-oxide

The crystallite size of Mn_3O_4 and MnO was calculated to be 20.3 nm (a = 5.19 Å, c = 11.41 Å) and 48.3 nm (a = 4.42 Å). It is notable that, the major peak from (211) plane of Mn_3O_4 is much stronger than that from (200) plane of MnO indicating the relative higher ratio of the former one than the later. The hazy peak at 2θ = ~ 25.1° can be attributed to (002) plane of rGO sheet [28].The absence of any sharp peak related to rGO indicate the surface was covered with high amount of manganese oxides.

5.2.4.4 rGO/Sn-oxide Binary Nanocomposite

The XRD of the rGO/Sn-oxide nanocomposite shows the formation of SnO_2 nanoparticles on the surface of rGO. The peaks at 2θ values 26.64°, 33.85°, 37.76°, 51.82°, 54.88°, 58.3°, 61.46°, 65.37° are associated with (110), (101), (200), (211), (220), (002), (310), (112) plane of SnO_2 (**JCPDS card no. 41-1445**, Space group: $P4_2/mnm$;

Lattice system: Tetragonal (Rutile); a = 4.74 Å, b = 4.74 Å, c = 3.19 Å) and the small peak at 2θ = 42.82° is related to the hexagonal structure of carbon from rGO sheet [32-33]. The crystallite size of SnO_2 was calculated to be 4.4 nm (a = 4.72, b = 3.13 Å).

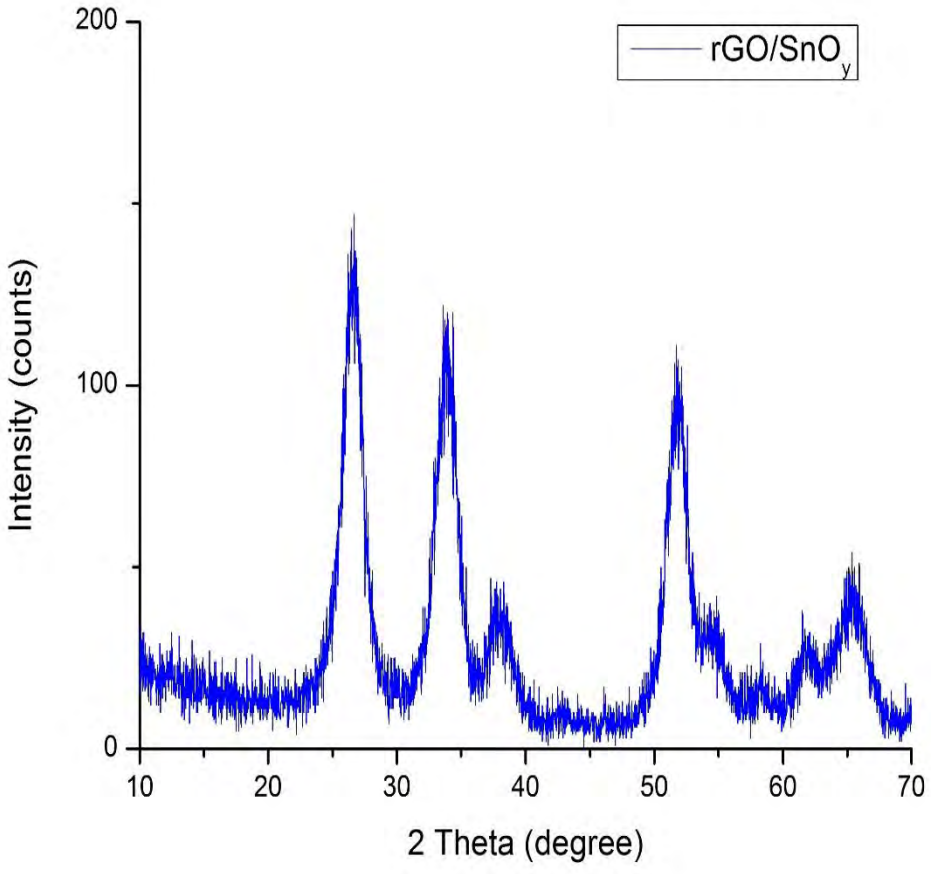

Fig. 5.21- XRD pattern of rGO/Sn-oxide

5.2.4.5 rGO/Mn-oxide/Sn-oxide Ternary Nanocomposite

The XRD of the rGO/Mn-oxide/Sn-oxide ternary nanocomposite annealed under inert atmosphere shows mostly broad peak compared to the binary nanocomposites indicating poor crystallinity and low crystallite size. The peaks at 17.86°, 28.9°,36°, 38° and 59.71° were traced to (211), (112), (211), (004) and (224) planes of Mn_3O_4. The peaks at 35° and 58.7° were traced to (111) and (224) plane of MnO. The peaks at 34.07° and 51.9° were traced to (101) and (211) planes of SnO_2 along with contribution from different planes of manganese oxides. No peak for rGO was obtained possibly due to the higher amount of nanoparticles anchored on its surface.

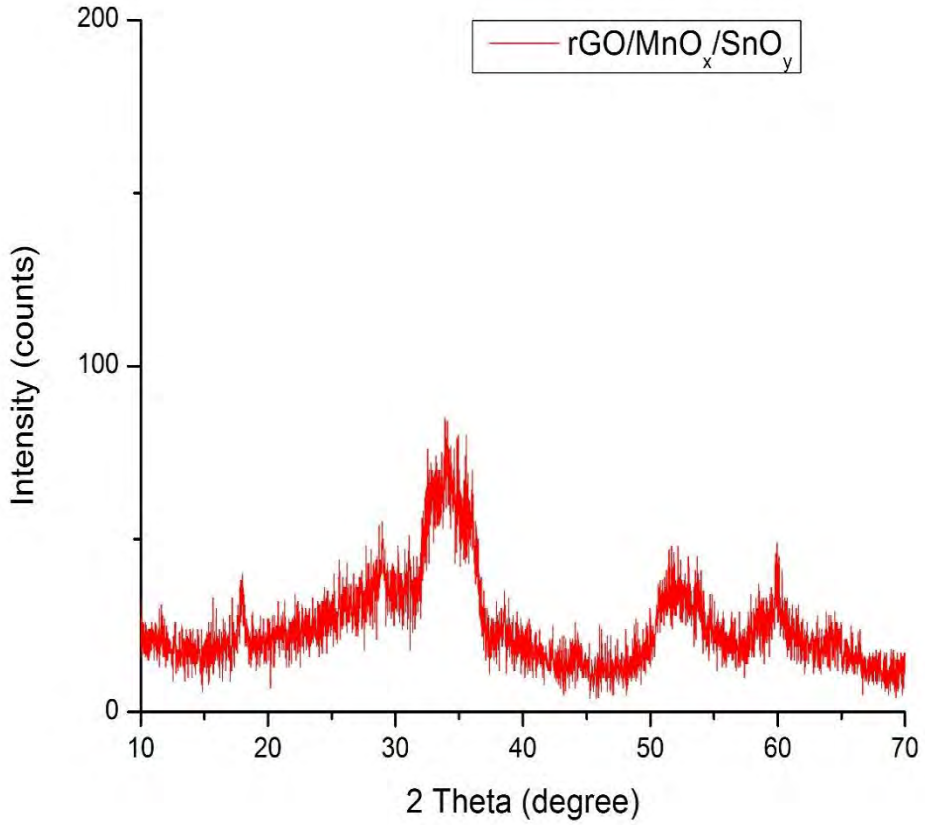

Fig. 5.22- XRD pattern of rGO/Mn-oxide/Sn-oxide

XRD analysis results from the synthesized materials altogether can be shown as follow-

Table 5.12- Crystallite size and lattice parameters of metal oxides in the nanocomposite

M-oxide	**Crystallite size (nm)**	**Crystal system**	**Lattice parameters (Å)**		
			a	**b**	**c**
Mn_3O_4	20.3	Tetragonal	5.19	5.19	11.41
MnO	48.3	Cubic	4.42	4.42	4.42
SnO_2	4.8	Tetragonal	4.72	4.72	3.13

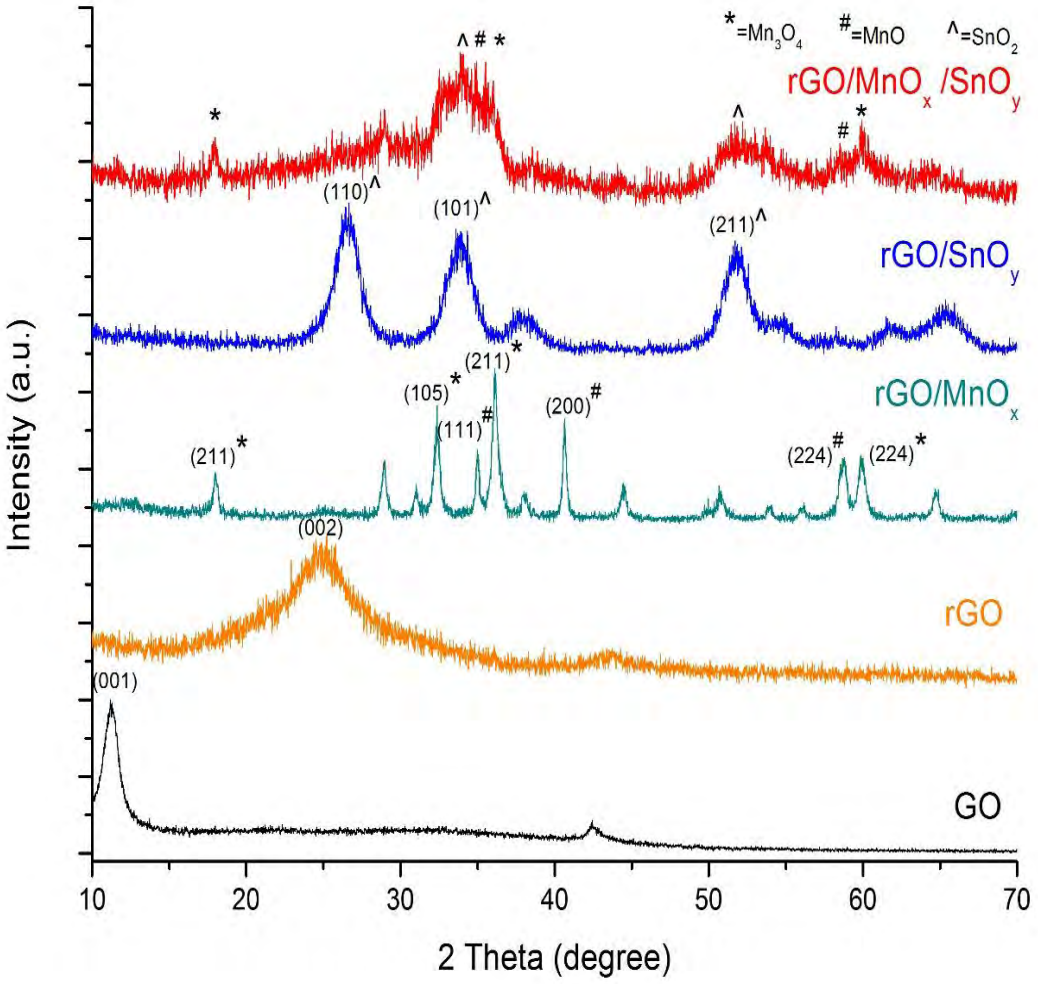

Fig. 5.23- XRD pattern of GO, rGO and the nanocomposites

5.2.5 Thermogravimetric Analysis (TGA)

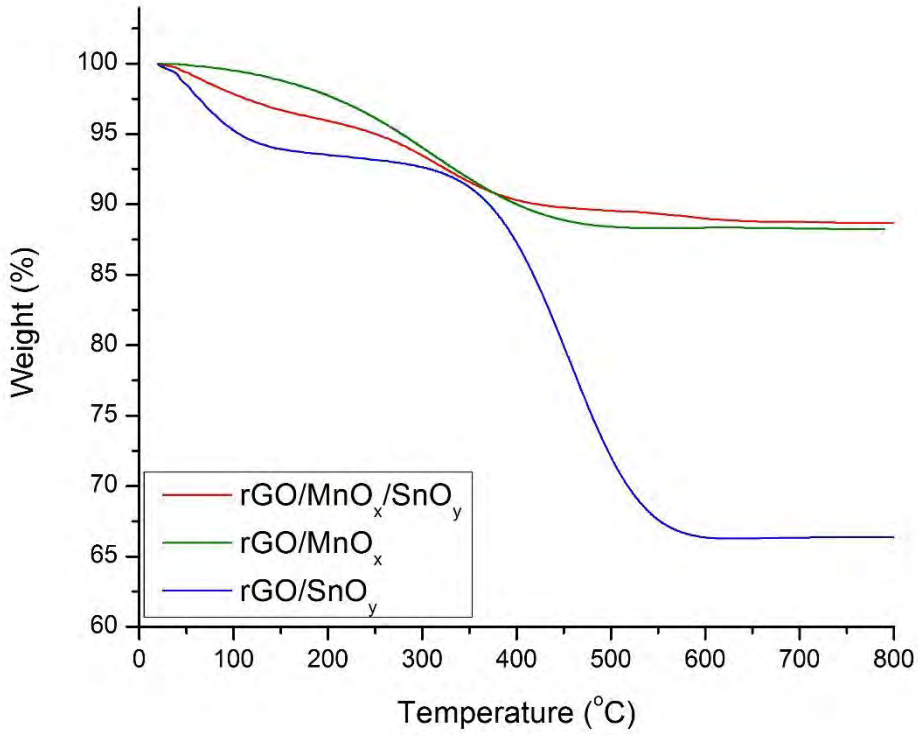

Fig. 5.24- TGA diagram of binary and ternary nanocomposites

The TGA graph of rGO/Mn-oxide shows, 2.90% weight loss within the temperature range of 23.79°- 205.74°C owing to the removal of surface absorbed water, 8.76% weight loss within 205.74° - 530.38°C mainly due to the loss of oxygen containing functional groups leading to evaporation of CO and CO_2 and finally retain 88.34% at 800°C. The TGA graph of rGO/Sn-oxide shows, 5.94% weight loss within 20.05°-139.42°C resulting from loss of moisture, 1.55% weight loss within 139.42° - 306.92°C due to the removal of oxygen containing functional groups as CO or CO_2, 26.17% weight loss within 306.92° - 600.78°C due to the oxidation of rGO sheet exposed and finally reaches 66.34% weight at 800°C.

The TGA graph of rGO/Mn-oxide/Sn-oxide shows, 5.41% weight loss within 20.71° - 266.92°C from loss of moisture and interlayer water mainly, 5.69% weight loss within 266.92° - 634.07°C from loss of oxygen containing functional groups and finally reaches 88.73% weight at 800°C.

All of the TGA graphs can be seen to follow a similar pattern possibly due to their synthesis from similar elements. Three segments are notable among the curves. The first segment lies within room temperature to ~ 250°C, due to loss of absorbed moisture mainly. The next segment lies within 250° - 650°C, mainly due to the removal of oxygen containing groups along with oxidation of rGO. But, the oxidation of rGO was prominent in case of rGO/Sn-oxide, within 300° - 600°C, most probably resulting from its higher exposed area of rGO.

All of the results from TGA has been summarized below-

Table 5.13- TGA data of the nanocomposites

Samples	**Range of temperature (°C)**				**Mass retained at 800° C (%)**
	Mass loss (%)				
rGO/Mn-oxide	23.7°-205.7°	205.7°-530.3°	530.3°-800°		**88.34%**
	2.90%	8.76%	0%		
rGO/Sn-oxide	20.1°-139.4°	139.4°-306.9°	306.9°-600.7°	600.7°-800°	**66.34%**
	5.94%	1.55%	26.17%	0%	
rGO/Mn-oxide/Sn-oxide	20.7°-266.9°	266.9°-634.1°	634.°-800°		**88.73%**
	5.41%	5.69%	0.17%		
Explanation	Evaporation of absorbed moisture and interlayer water	Loss of oxygen containing functional groups with evaporation as CO, CO_2	Oxidation of carbon from rGO		**Thermally stable at 800° C**

5.3 Investigation of the Behaviour in Dye Decolourization

5.3.1 Determination of Molar absorption coefficient

Molar absorption coefficient, λ was determined from the slope of the plot of absorbance against concentration of MB solutions at different concentration (viz. 1, 3, 5, 7 and 10 ppm) at ~ 30°C.

Table 5.14- Absorbance of MB at different concentrations, λ_{max} = 664 nm

Run no.	[MB] ppm	Absorbance
1	1	0.282
2	3	0.894
3	5	1.209
4	7	1.853
5	10	2.572

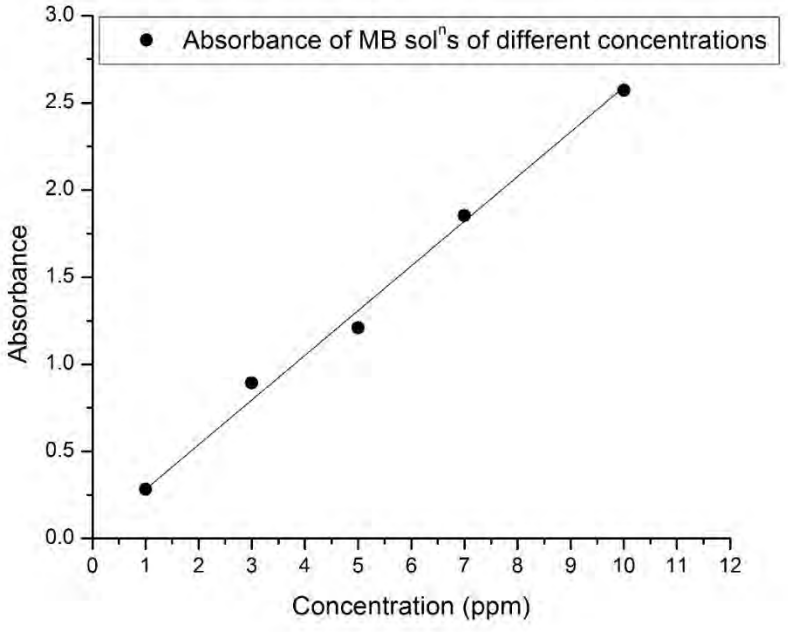

Fig. 5.25- Absorbance of MB solution at different concentrations

Following Beer-Lambert law (**A = εcl**), from the above graph, it was found that, molar absorption coefficient, $\varepsilon = 9.32 \times 10^4$ **L mol^{-1} cm^{-1}**.

5.3.2 Determination of Equilibrium Time of Interaction

Equilibrium time of interaction with MB solution for the ternary nanocomposite was determined to be 75 minutes, by observing absorbance and final equilibrium concentration of MB via Beer-Lambert law at different time intervals viz. 0, 15, 30, 45, 60, 75, 90 and 120 minutes at pH = 7.

Table 5.15- Determination of equilibrium time of interaction

Run no.	Time(min)	Inert treated	
		Absorbance	[MB]× 10^6 M
1	0	0.995	10.7
2	15	0.604	6.48
3	30	0.656	7.04
4	45	0.649	6.96
5	60	0.685	7.35
6	75	0.586	6.28
7	90	0.605	6.49
8	120	0.600	6.44

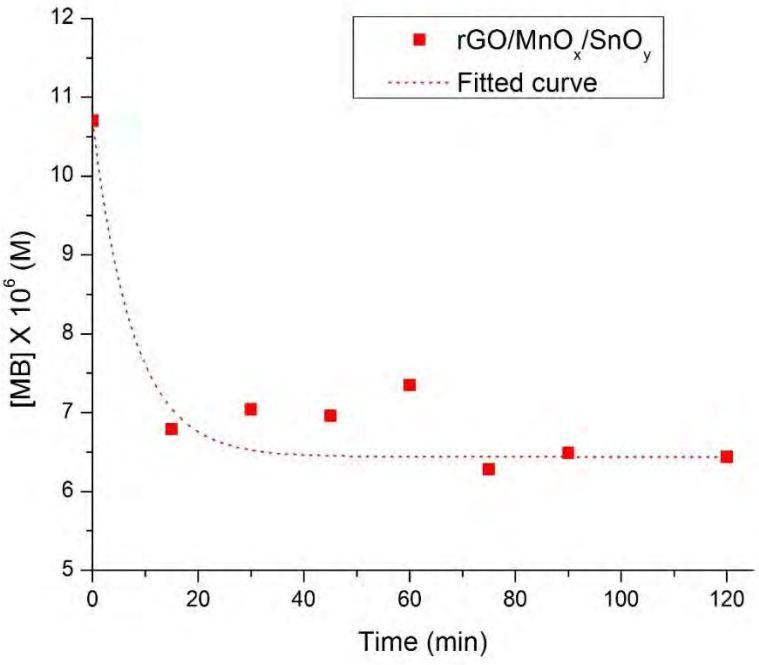

Fig. 5.26- Determination of equilibrium time of interaction

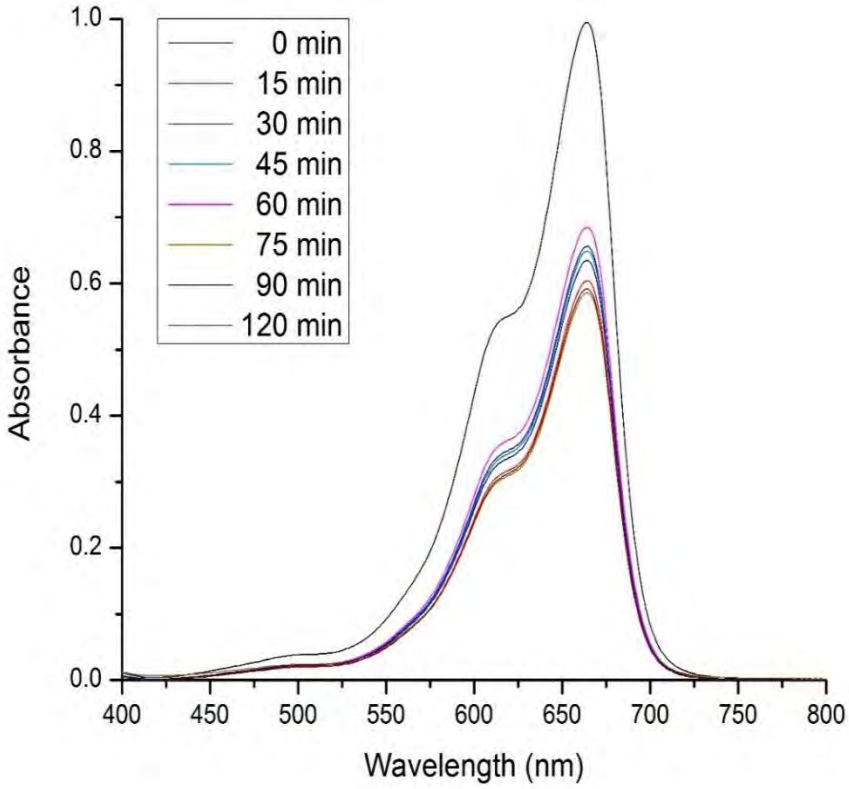

Fig. 5.27- UV spectra of the ternary nanocomposite at different time intervals

5.3.3 Effect of Contact Time

The effect of contact time on the removal of MB dye by the nanocomposites was observed by calculating specific amount adsorbed from the concentration of MB in the resulting supernatants after 0, 5, 10, 15, 20, 30, 45, 60 and 75 minutes of interaction, at pH=3, using the formulae,

$$\mathbf{q_t = \left(\frac{C_0 - C_t}{m}\right) V}$$

Where, C_0 and C_t are the initial and equilibrium concentrations of MB in solution (mg/L), V is the volume of solution (L), m is the mass of adsorbent (g).

It was found that, among the composites highest capacity, 17.7 mg/g was shown by the ternary nanocomposite which was almost same, but slightly higher to specific adsorption capacity 17.5 mg/g of rGO/Mn-oxide and 17.4 mg/g of rGO/Sn-oxide binary nanocomposite.

Table 5.16- Effect of contact time on MB dye removal by the nanocomposites

Run no.	Time (min)	rGO/Mn-oxide/Sn-oxide		rGO/Mn-oxide		rGO/Sn-oxide	
		Abs.	q_t (mg/g)	Abs.	q_t(mg/g)	Abs.	q_t(mg/g)
1	0	0.944	0	0.953	0	0.964	0
2	5	0.364	11.0	0.105	16.1	0.529	8.23
3	10	0.223	13.7	0.081	16.6	0.298	12.6
4	15	0.155	15.0	0.064	16.9	0.177	15
5	20	0.132	16.4	0.065	16.9	0.170	15.1
6	30	0.084	16.6	0.043	17.3	0.078	16.8
7	45	0.07	17.3	0.05	17.2	0.141	15.6
8	60	0.033	17.3	0.042	17.3	0.083	16.7
9	75	0.035	**17.7**	0.035	**17.5**	0.051	**17.4**

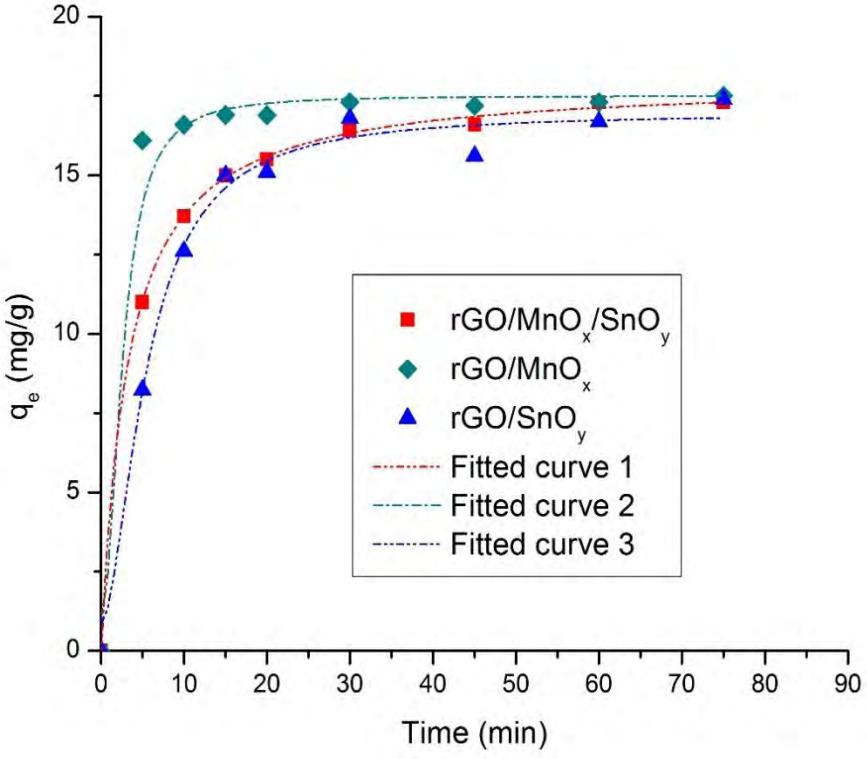

Fig. 5.28- Effect of contact time on MB dye removal by the nanocomposites

5.3.4 Effect of pH

The effect of pH on MB dye removal by the ternary nanocomposite was unraveled by conducting experiment at an acidic pH 3, a basic pH 10 and at the neutral pH 7 and calculating percentage of removal of MB at those pH values using the formulae,

$$\%E = \left(\frac{C_0 - C_e}{C_0}\right) \times 100$$

Where, C_0 and C_e are the initial and equilibrium concentrations of MB in solution (M).

It was found that the ternary nanocomposite shows maximum dye removal capacity at lower pH value and it falls around pH = 4 indicating the change of surface charge i.e. point of zero charge (PZC). After PZC, the surface of nanocomposite may have turned positive and repulsed MB, provided that methylene blue is a basic, cationic dye [34-35].

Table 5.17- Effect of pH on MB dye removal by the ternary nanocomposite

pH	rGO/Mn-oxide/Sn-oxide		
	Initial conc. C_0 ×10^6 M	**Equilibrium conc.C_e ×10^6 M**	**Removal (%)**
1	8.78	0.23	97.3
3	10.1	0.37	96.3
5	9.50	6.05	36.2
7	10.7	6.28	41.3
10	8.33	6.32	24.1

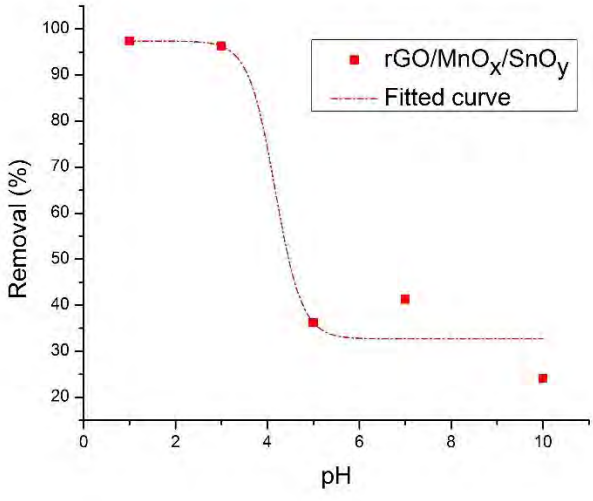

Fig. 5.29- Effect of pH on MB dye removal by the ternary nanocomposite

5.3.5 Effect of Dose

The effect of dose on dye removal by the ternary nanocomposite was analyzed by performing dye removal with two different amount 5 and 10 mg of the ternary nanocomposite treated under inert atmosphere with same volume of MB solution 25mL for equilibrium time 75 minutes at pH = 3. It was noted that, with increase in dose, specific adsorption capacity and removal rate both falls which may be attributed to possible aggregation of nanoparticles at higher dose [36].

Table 5.18- Effect of dose on MB dye removal by the ternary nanocomposite

Amount m (mg)	**Initial conc. $C_0 \times 10^6$ M**	**Equilibrium conc.C_e $\times 10^6$ M**	**Percentage of removal, % E $=\left(\frac{C_0-C_e}{C_0}\right)\times 100$**	**Specific amount adsorbed, q_e $=\left(\frac{C_0-C_e}{m}\right)V$**
2	10	0.38	96.1	42.8
5	10.1	0.37	96.3	18
10	10.4	1.22	88.3	8.7
20	10	0.51	94.8	4.2

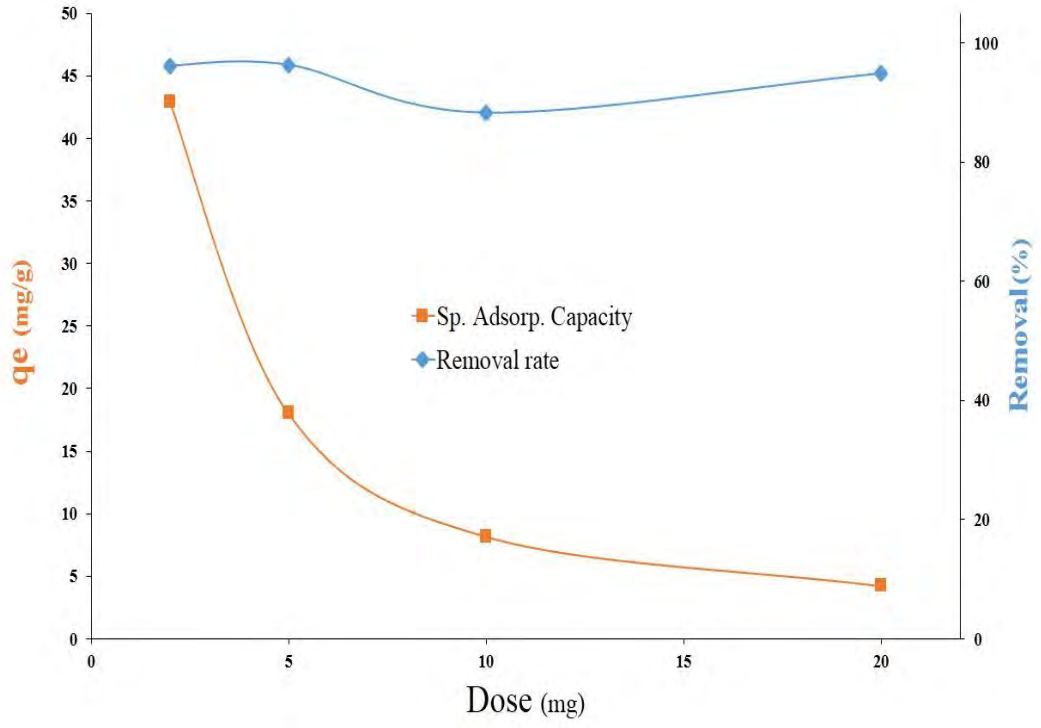

Fig. 5.30- Effect of dose on MB dye removal by the ternary nanocomposite

5.4 Investigation of Electrochemical Behaviour

5.4.1 Cyclic Voltammetry (CV)

Cyclic voltammetry (CV) of the samples was initially performed within -0.5 V to 1.0 V at 100 mV/s scan rate, to observe the nature of cyclic voltammogram of the nanocomposites. It showed almost symmetric shape within 0 - 0.6 V indicating a non-Faradic behaviour.

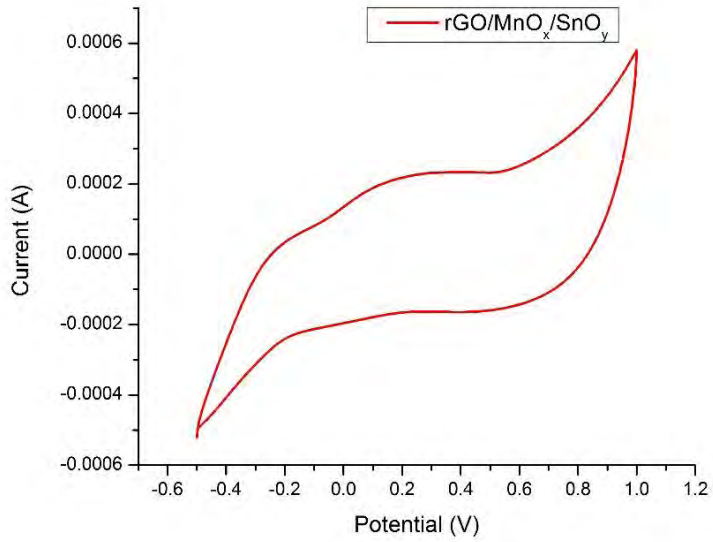

Fig. 5.31- Cyclic voltammogram of rGO/Mn-oxide/Sn-oxide ternary nanocomposite

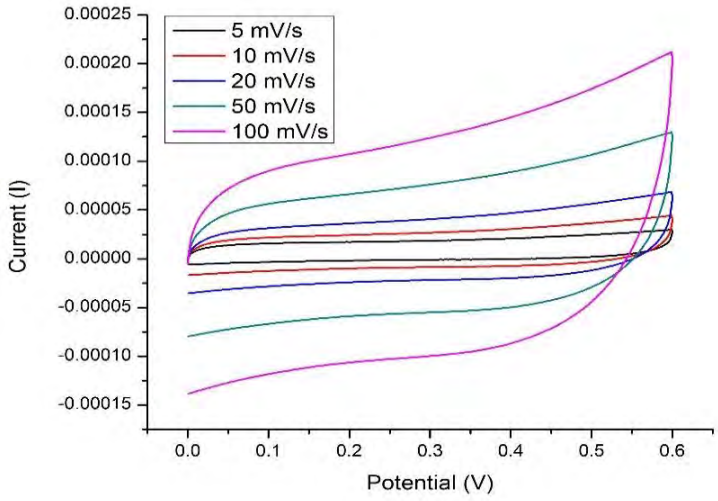

Fig. 5.32- Non-faradic behaviour of rGO/Mn-oxide/Sn-oxide ternary nanocomposite

The non-Faradic behaviour is attributed to electrochemical double layer charge storage mechanism, i.e. capacitance. CV of the ternary nanocomposite at different scan rate shows increase of current with the increase of scan rate, as per Randles–Sevcik equation (current proportional to the square root of scan rate), which is due to mass transfer ion adsorption-desorption, indicating porus nature of the composite, an important factor for charge storage by electrochemical double layer capacitor (EDLC) [37].

However, within an extended potential window 0 - 1.0 V, cyclic voltammogram appears with slightly distorted shape indicating presence of Faradic process and charge storage in the extended region by Faradic process is known as pseudocapacitance. The observation of increase of current with the increase of scan rate was present here too.

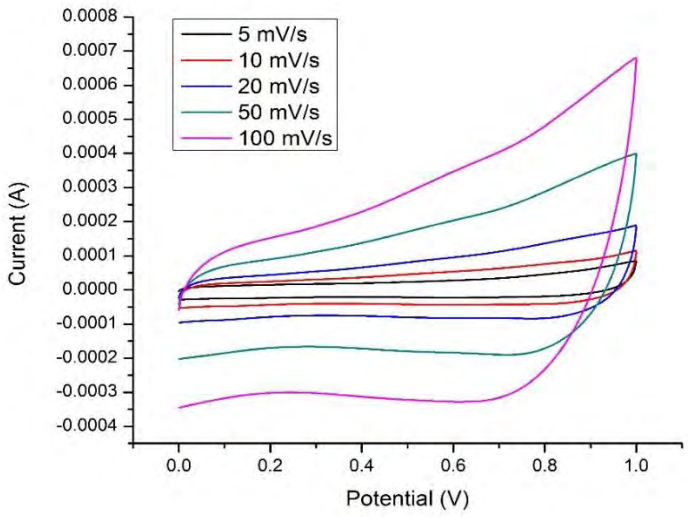

Fig. 5.33- Faradic behaviour of rGO/Mn-oxide/Sn-oxide ternary nanocomposite

5.4.2 Chronopotentiometry (CP)

Galvanostatic charging-discharging (GCD) was performed within the potential windows suggested from CV at different current density to have idea about the capacitive ability of the nanocomposites. The value of specific capacitance was obtained using the formulae,

$$C_s = \frac{it}{m\Delta V} = \frac{jt}{\Delta V}$$

Where, C_s is mass-specific capacitance in F/g, i is current in A, m is mass of active material in g, j is current density in A/g, t is time in s and ΔV is the potential window.

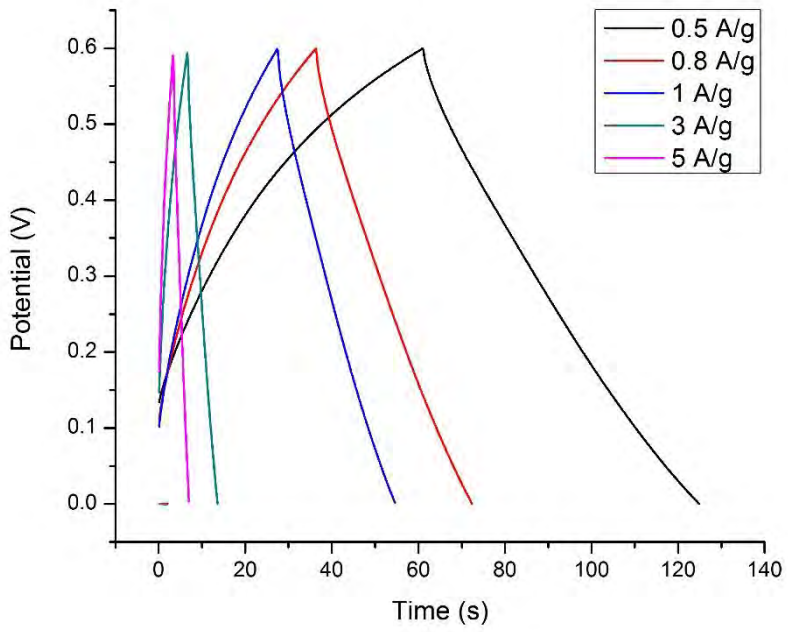

Fig. 5.34- GCD curve of the ternary nanocomposite within 0 - 0.6 V at 0.5, 0.8, 1, 3 and 5 A/g

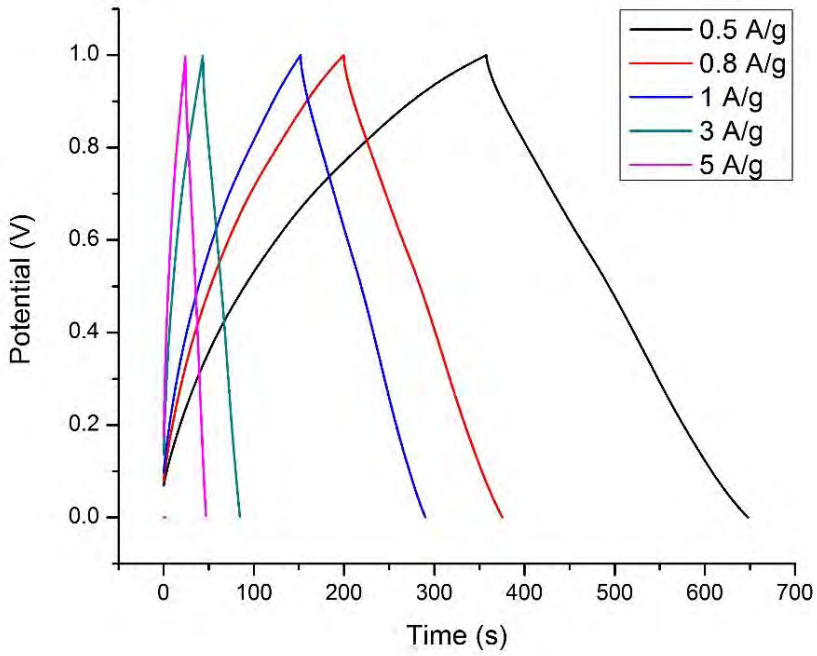

Fig. 5.35- GCD curve of the ternary nanocomposite within 0 - 1.0 V at 0.5, 0.8, 1, 3 and 5 A/g

GCD within 0 - 0.6 V at 0.5, 0.8, 1, 3 and 5 A/g shows specific capacitance 53.2, 48.2, 45.3, 35.6 and 29.5 F/g respectively. These values increase with the extension of potential window. GCD within 0 - 1.0 V at 0.5, 0.8, 1, 3 and 5 A/g shows specific capacitance 145.1, 141.3, 139.3, 121.29 and 114.5 A/g respectively. The decrease in capacitance at higher current density is attributed to the restriction arise from faster movement of electrolyte ions towards adsorption sites [38].

However, the ternary nanocomposite shows a lower specific capacitance in comparison to the binary nanocomposites. Within 0 - 1.0 V at 0.5 A/g current density, the rGO/Mn-oxide/Sn-oxide ternary nanocomposite, rGO/Mn-oxide and rGO/Sn-oxide binary nanocomposites shows specific capacitance 145.6, 463.8 and 178.3 F/g respectively. The low specific capacitance of the ternary nanocomposite in comparison to the binaries particularly rGO/Mn-oxide is possibly due to the higher ratio of MnO in compared to Mn_3O_4 in the ternary nanocomposite. The oxidation number of Mn in Mn_3O_4 and MnO is +2.66 and +2 respectively. During the oxidation of Sn^{2+} to Sn^{4+} in the preparation step, the Mn_3O_4 on rGO surface are favoured to reduction to MnO which is reported to possess less capacitive ability than Mn_3O_4.

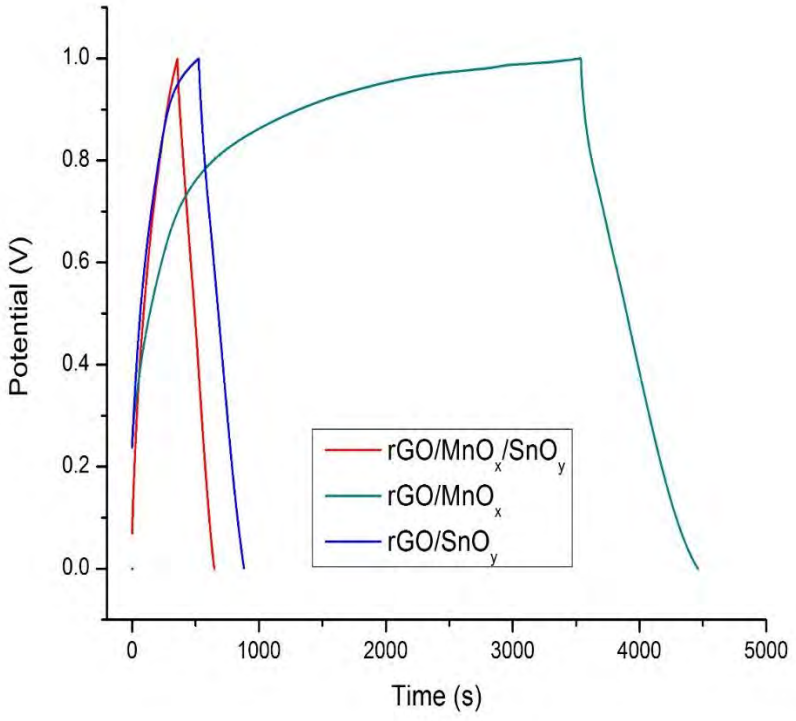

Fig. 5.36- GCD curve of the nanocomposites within 0 - 1.0 V at 0.5 A/g

Although the ternary nanocomposite shows relatively lower specific capacitance compared to the binaries, its ratio of discharging/charging time, 0.84 is higher than that of rGO/Mn-ox, 0.26 and rGO/Sn-ox, 0.69.

Table 5.19- Specific capacitance of the nanocomposites at 0.5 A/g current density

Sample	Specific Capacitance (F/g)	Discharge/charge time ratio
rGo/Mn-oxide	463.8	0.26
rGO/Sn-oxide	178.3	0.69
rGO/Mn-oxide/Sn-oxide	145.6	0.84

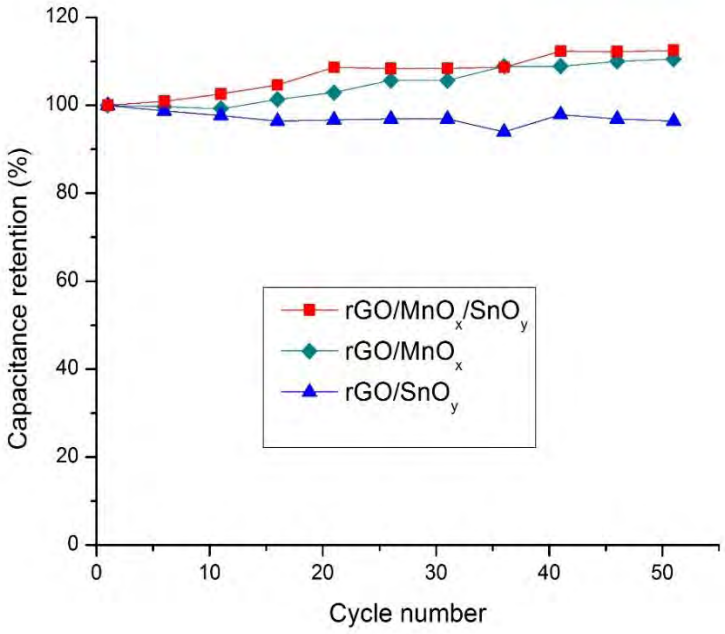

Fig. 5.37- Capacitance retention profile of the nanocomposites within 0 - 1 V at 5 A/g for first 50 cycles

Chronopotentiometry was also used to explore the cyclic stability of the nanocomposites. Chronopotentiometry was recorded at 5 A/g, initially, for first 50 cycles and they showed uniform structure. Specific capacitance was calculated with an interval of 5 cycles. It showed that the rGO/Mn-ox and rGO/Sn-ox binary nanocomposites and the rGO/Mn-ox/Sn-ox ternary nanocomposite retains 110.52%, 96.41% and 112.5% specific capacity

respectively after 50 cycles. Thus the ternary nanocomposite shows maximum retention capacity. The preliminary increase in the capacitance can be explained as a result of complete exposure of the active sites of the electrode to the electrolyte after repeated charging/discharging [39]. The specific and the interfacial capacitance values are decreased by a certain amount with increasing number of cycles due to the loss of active material caused by dissolution and/or detachment during the early charging and discharging cycles in the electrolyte [40].

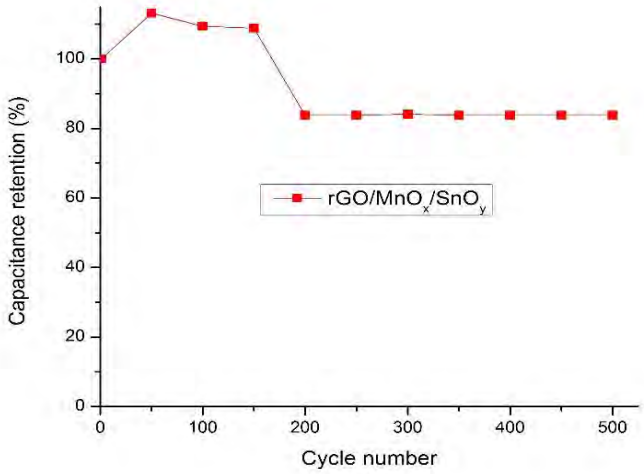

Fig. 5.38- Capacitance retention profile of the ternary nanocomposite within 0 - 1 V at 5 A/g for first 500 cycles

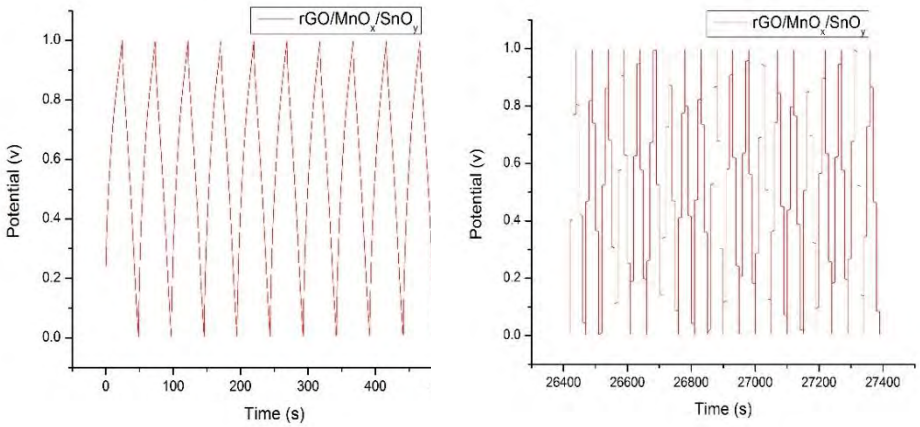

Fig. 5.39- Curve of first (left) and last (right) ten cycles of the GCD test of the ternary nanocomposite for 500 cycles

The ternary nanocomposite was further studied for longer cycles under same conditions and it was found to retain 84% of its capacitance after 500 cycle.

5.4.3 Electrochemical Impedance Spectroscopy (EIS)

Electrochemical impedance spectroscopy is a powerful tool to realize the capacitive behaviour of the system by providing information on possible electrochemical reactions taking place at the electrode surface, presence of possible types of resistances and describing dependency of impedance on frequency of current.

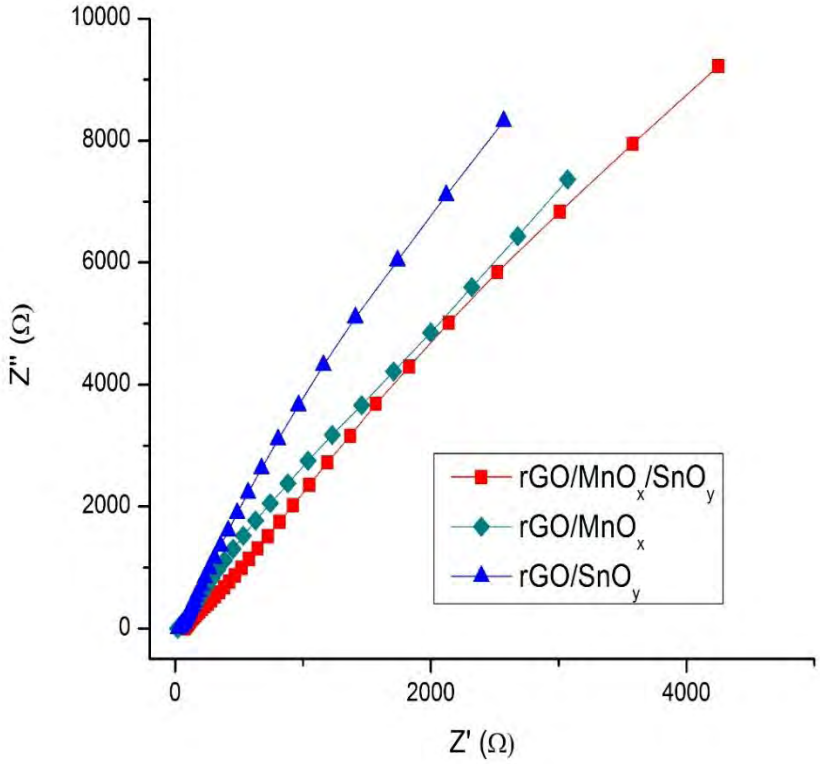

Fig. 5.40- Nyquist plot for the ternary and binary nanocomposites in 0.5M Na_2SO_4 aqueous solution recorded at ~ 30°C with open circuit voltage of 0 V and amplitude of 10 mV over a frequency range of 0.01 - 500 kHz.

The Nyquist plot from EIS measurement of the nanocomposites shows similar shape indicating similar structure of the nanocomposites. At high frequency region, both of the two binary nanocomposites shows a small semicircle appearance indicating presence of charge transfer resistance at some extent. But, the ternary nanocomposite shows almost linear shape indicating almost no charge transfer resistance. At, low frequency, the imaginary part of the impedance curves approaches a vertical line associated with Warburg impedance from diffusion, indicating good capacitive behavior [41-43]. It can be

seen that the slope of the straight line for the binaries are larger than that of the ternary nanocomposite, indicating a lower diffusive resistance of the electrolyte for the ternary nanocomposite.

As an equivalent circuit model, the following Randles circuit can be proposed-

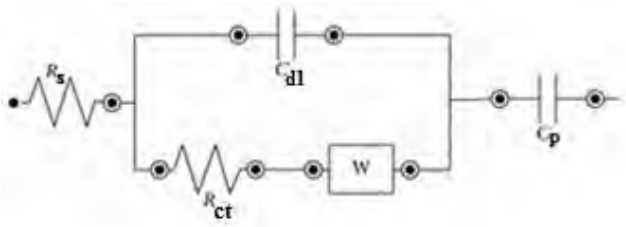

Fig. 5.41- Randles circuit representing the equivalent circuit for the nanocomposites under experiment

Where, R_s represents electrolyte resistance, C_{dl} stands for electrical double layer that is formed on the interface between electrode and its surrounding electrolyte as ions from the solution adsorb onto the electrode surface, C_p represents pseudocapacitance, R_{ct} represents the charge transfer resistance from kinetically controlled electrochemical reaction and W represents the Warburg impedance arise from diffusion [44-45].

References

1. Hummers, W. S., and Offeman, R. E., "Preparation of graphitic oxide", *J. Am. Chem. Soc*., vol. 80, pp. 1339-1339, 1958.
2. Dreyer, D. R., Park, S., Bielawski, C. W., and Ruoff, R. S., "The chemistry of graphene oxide", *Chem. Soc. Rev*., vol. 39, pp. 228-240, 2010.
3. Baojun, L., Huaqiang, C., Jin, S., Meizhen, Q., and Jamie, H. W., "Superparamagnetic Fe_3O_4 nanocrystals@graphene composites for energy storage devices", *J. mater. Chem*., vol. 21, pp. 5069-5075, 2011.
4. Ayrat, M. D., and James, M. T., "Mechanism of graphene oxide formation", *ACS Nano*, vol. 8(3), pp. 3060-3068, 2014.
5. Jong, H. K., Taehoon, K., Jaeyoo, C., Jisoo, P., Yern, S. K., Mi, S. C., Haesol, J., Kyang, T. P., Seung, J. Y., and Chong, R. P., "Hidden second oxidation step of Hummers method", *Chem. Mater*., vol. 28, pp. 756-764, 2016.
6. Songfeng, P., and Hui-Meng, C., "The reduction of graphene oxide", *Carbon*, vol. 50(9), pp. 3210-3228, 2012.
7. Seung, H. H. (2011) *Physics and Application of Graphene-Experiments*. InTech Ltd., Rijeka.
8. Lopez, M. P. L., Valverde, J. L., Sanchez-Silva, L., and Romero, A., "Solvent-based exfoliation via sonication of graphitic materials for graphene manufacture", *Ind. Eng. Chem. Res.*, vol. 55(4), pp. 845-855, 2016.
9. Chen, S., Zhu, J., Wn, X., Han, Q., and Wang, X., "Graphene oxide-MnO_2 nanocomposites for supercapacitors", *ACS Nano*, Vol. 4(5), pp. 2822-2830, (2010).
10. Zhong, L. S., Hu, J. S., Cui, Z. M., Wan, L. J., and Song, W. G., "In-situ loading of noble metal nanoparticles on hydroxyl-group-rich titania precursor and their catalytic applications", *Chem. Mater*., vol. 19, pp. 4557-4562, 2007.
11. Zhang, L. S., Jiang, L. Y., Yan, H. J., Wang, W., Song, W. G., Guo, Y. G., and Wan, L. J., "Mono dispersed SnO_2 nanoparticles on both sides of single layer graphene sheets as anode materials", *J. Mater. Chem*., vol. 20, pp. 5462-5467, 2010.
12. Xia, G., Li, N., Li, D., Liu, R., Wang, C, Li, Qing, Lu, X., Spendelow, J. S., Zhang, J., and Wu, G., "Graphene/Fe_2O_3/SnO_2 ternary nanocomposites as a high-performance anode for lithium ion batteries", *ACS Appl. Mater. Interfaces*, vol. 5, pp. 8607-8614, 2013.

13. Kiyoshi, T., and Masao, I., "Study on thermal decomposition of MnO_2 and Mn_2O_3 by thermal analysis", *T. Jpn. I. Met*, vol. 24(11), pp. 754-758, 1983.
14. Arno, H. R., "Manganese compounds", *UEIC*, (2000).
15. Sina, A., Hamed, A. and Hyoung, S. K., "Fast and fully scalable synthesis of reduced graphene oxide", *Sci. Rep*., vol. 5, pp. 10160-10166, 2015.
16. Daniela, C. M., Dmitry, V. K., Jacob, M. B., Alexander, S., Zhengzong, S., Alexander, S., Lawrence, B. A., Wei, L. and James, M. T., "Improved synthesis of graphene oxide, *ACS Nano*, vol. 4(8), pp. 4806-4814, 2010.
17. Yongchao, S., and Edward, T. S., "Synthesis of water soluble graphene", *Nano Lett.*, vol. 8(6), pp. 1679-1682, 2008.
18. Sourav, S., Tapas, K. G., Dipak, R., Indranil, R., Amartya, B., Gunjan, S., Mukut, C. and Dipankar, C., "Studies on synthesis of reduced graphene oxide (rGO) via green route and its electrical property", *Mater. Res. Bull*, vol. 63, pp. 80-87, 2015.
19. Ali, G., Leila, V. F., Nader, N. P. and Mina, R., "A new application of nano-graphene oxide (NGO) as a heterogenous catalyst in oxidation of alcohols types", *Chem. J.*, vol. 1(4), pp. 151-158, 2015.
20. Deepak, P. D., Dattatray, S. D., Rahul, R. S. and Chandrakant, D. L., "Conversion of chemically prepared interlocked cubelike Mn_3O_4 to birnessite MnO_2 using electrochemical cycling", *J. Electrochem. Soc.*, vol. 157(7), pp. A812-A817, 2010.
21. Dong, M. J., Yoon, M., Hyung, S. I.,Young, S. S., Yong, J. C., Chi, W. L., Jeunghee. P., Ah-Young, J. and Minyung, L., "Nanodiamonds as photocatalysts for reduction of water and graphene oxide", *Chem. Commun*., vol. 48, pp. 696-698, 2012.
22. Humaira, S., K Christian, K., Vimlesh, C. and Kwang, S. K., "Graphene-SnO_2 composites for highly efficient photocatalytic degradation of methylene blue under sunlight", *Nanotechnology*, vol. 23, pp. 355705-355711, 2012.
23. Nanjundan, A. K., Serge, G., Florence, D., Gerard, B. and Lionel, D., Synthesis of high quality reduced graphene oxide nanosheets free of paramagnetic metallic impuritiest", *J. Mater. Chem. A*, vol. 1, pp. 2789-2794, 2013.
24. Huanping, Y., Hailong, H., Yingying, W. and Ting, Y., "Rapid and non-destructive identification of grapheme oxide thickness using white light contrtast spectroscopy", *Carbon*, vol. 52, pp. 528-234, 2013.
25. Shikai, D. and Vikas, B., "Wrinkled, rippled and crumpled graphene: an overview of formation, mechanism, electronic properties and applications", *Mater. Today*, vol.

19, pp. 197-212, 2016.

26. Zhenyu, W., Yan, X., Xiaobiao, C., Pengfei, C., Biao, W., Yuan, G. and Xiaowei, L., "Humidity-sensing properties of urchinlike CuO nanostructures modifies by reduced graphene oxide", *ACS Appl. Mater. Interfaces*, vol. 6, pp. 3888-3895, 2014.
27. Norsaadatul, A. M. Z. and Nurul, H. I., "Enhanced capacitance of hybrid layered graphene/nickel nanocomposite for supercapacitors", *Sci. Rep*., vol. 6, pp. 32082-32088, 2016.
28. Shanmugam, M. and Jayavel, R., "Synthesize of graphene-tin oxide nanocomposites and its photocatalytic properties for the degradation of organic pollutants under visible light", *J. Nanosci. Nanotechnol*., vol. 15(9), pp. 7195-7201, 2015.
29. Dewei, W., Yuqi, L., Qihua, W. and Tingmei, W., "Facile synthesis of porous Mn_3O_4 nanocrystal-graphene nanocomposites for electrochemical supercapacitors", *Wur. J. Inorg. Chem*., vol. 4, pp. 628-635, 2012.
30. Prashanth, W. M., Arindram, I., Patrick, L., Michael, S., Caren, G., Reinhard, S. and Matthias, D., "Nanostructured manganese oxides as highly active water oxidation catalysts: a boost from manganese precursor chemistry", *ChemSusChem* vol. 7, pp. 2202-2211, 2014.
31. Pinto, R., Carmejim, M. J. and Montemor, M.F., "Electrodeposition and isothermal aging of Co and Mn layers on stainless steel for interconnectors: Initial stages of spinel phase formation", *J. Power Sources*, vol. 255, pp. 251-259, 2014.
32. Haizhem, L., Li, Z., Zebin, S., Yan, L., Bo, Y. and Shiqiang, Y., "One-step synthesis of magnetic 1,6-hexanediaminefunctionalized reduced graphene oxide-zinc ferrite for fast adsorption of Cr(VI)", *J. Name*., vol. 0, pp. 1-3, 2013.
33. Wei, C., Debraj, G. and Shaowei, C., "Large scale electrochemical synthesis of SnO_2 nanoparticles", *J. Mater. Sci*., vol. 43, pp. 5291-5299, 2008.
34. Garg, V. K., Moirangthem, A., Rakesh, K. and Renuka, G., "Basic dye (methylene blue) removal from simulated wastewater by adsorption using Indian rosewood sawdust: a timber industry waste", *Dyes and Pigments*, vol. 63, pp. 243-250, 2004.
35. Mohammad, M. A. and Ahmed, A. E., "Adsorption of cationic dye (methylene blue) from water using polyaniline nanotubes Base", *J. Phys. Chem. C*, vol. 114, pp. 14377-14383, 2010.
36. Alzaydien, A. S., "Adsorption behavior of methyl orange onto wheat bran: role of surface and pH", *Orient. J. Chem.*, vol. 31(2), pp. 643-651, 2015.

37. Gupta, R. K., Candler, J., Palchoudhury, S., Ramasamy, K., and Gupta, B. K., "Flexible and high performance supercapacitors based on $NiCo_2O_4$ for wide temperature range applications", *Sci. Rep*., vol 5, pp. 15265-15274, 2015.
38. Hu, Z., Zu, L., Jiang, Y., Lian, H., Liu, Y., Li, Z., Chen, F., Wang, X. and Cui, X., "High specific capacitance of polyaniline/mesoporous manganese dioxide composite using KI-H_2SO_4 electrolyte", *Polymers,* vol. 7, pp. 1939-1953, 2015.
39. Wimalasiri, Y., Fan, R., Zhao, X. S. and Zou, L., "Assembly of Ni-Al layered double hydroxide and graphene electrodes for supercapacitors", *Electrochim. Acta,* vol. 134, pp. 127-135, 2014.
40. Dubal, D. P., Dhawale, D. S., Salunkhe, R. R. and Lokhandez, C. D., "Conversion of chemically prepared interlocked cubelike Mn_3O_4 to birnessite MnO_2 using electrochemical cycling", *J. Electrochem. Soc.,* vol. 157(7), pp. 812-817, 2010.
41. Mshazi, P. N., Westbroek, P., Ozoemenac, K. I. and Nykong, T., "Surface chemistry and electrocatalytic behaviour of tetra-carboxy substituted iron, cobalt and manganese phthalocyanine monolayers on gold electrode", *Electrochim. Acta*, vol. 53, pp. 1858-1869, 2007.
42. Mai, Y. J., Wang, X. L., Xiang, J. Y., Qiao, Y. Q., Zhang, D., Gu, C. D., Tu, J. P., "CuO/graphene composite as anode materials for lithium-ion batteries", *Electrochim. Acta*, vol. 56, pp. 2306-2311, 2011.
43. Fenghua, L., Jiangfeng, S., Huafeng, Y., Shiyu, G., Quixian, Z., Dongxue, H., Ari, I. and Li, N., "One step synthesis of graphene/SnO_2 nanocomposites and its application in electrochemical supercapacitors", *Nanotechnology*, vol. 20, pp. 455602-455607, 2009.
44. Mohammad, R. H., Chin, W. L., Bee, A. H. and Wan, J. B., "Effect of Ce doping on rGO-TiO_2 nanocomposite for high photoelectrocatalytic behaviouur", *Int.J. Photoenergy*, vol. 2014, pp. 141368-141375, 2014.
45. Velmurugan, V., Srinibasarao, U., Ramchandran, R., Saranya, M., Santhos, C. and Grace, A. N., "Synthesis of tin oxide/graphene (SnO_2/G) nanocomposite and its electrochemical properties for supercapacitor applications", *Mater. Res. Bull.*, vol. 84, pp. 145-151, 2016.

Chapter 6

Conclusion

6. Conclusion

Graphene/Mn-oxide/Sn-oxide ternary nanocomposites can be successfully synthesized along with its binaries by following wet chemical route as it was confirmed with FTIR, EDX and XRD in the present study while the composition of the composite was studied with EDX and TGA and the structural characterization of the synthesized materials were performed using FESEM, XRD and TGA.

Structural characterization showed that, the Graphene/Mn-oxide binary nanocomposite is consist of tetragonal Mn_3O_4 and a few cubic MnO, while the Graphene/Sn-oxide binary nanocomposite is consist of tetragonal SnO_2. The Graphene/Mn-oxide/Sn-oxide ternary nanocomposite contains all the nanoparticles of binaries, but with a different extent.

Suitability of the ternary nanocomposite in dye removal was studied with MB as a model dye using UV-Vis absorption spectroscopy. Study of pH effect showed that, it shows maximum adsorption capacity at acidic pH. In the study of contact time, with 5 mg sample in 5 ppm MB solution of pH = 3 at ~ 30°C, the ternary nanocomposite showed a specific adsorption capacity of 17.7 mg/g, while that of graphene/Mn-oxide and graphene/Sn-oxide binary nanocomposites, under same conditions, was 17.5 mg/g and 17.4 mg/g respectively; suggesting that, the binary and the ternary nanocomposites have almost same amount of surface area. Study of dose effect revealed that, it is more effective at lower dose, possibly due to its aggregation at higher dose resulting to low surface area and hence low specific adsorption capacity.

The electrochemical capacitive behaviour of the ternary nanocomposite was explored using electrochemical working station with CV, CP and EIS. Three electrode system including surface modified graphite electrode as working electrode in 0.5 M Na_2SO_4 was employed. The range of 0 - 1.0 V was chosen as the working potential window from CV. GCD within that window at 0.5 A/g, showed a specific capacitance of 145.6 F/g, while under the same conditions, the graphene/Mn-oxide and the graphene/Sn-oxide binary nanocomposites showed 463.8 and 178.3 F/g specific capacitance respectively. The difference was attributed to the different ratio of the oxide forms of metals on graphene and their nature in nanocomposites. After, 500 cycles of GCD at 5 A/g, the ternary naocomposite retained 84% of its capacity. EIS study found that, the ternary nanocomposite possess lowest charge transfer resistance among the three synthesized nanocomposites, implying it as a good capacitive material.